



**HAL**  
open science

# Behaviour of a Colloid close to an Air-Water Interface : Interactions and Dynamics

Stefano Villa

► **To cite this version:**

Stefano Villa. Behaviour of a Colloid close to an Air-Water Interface: Interactions and Dynamics. Other [cond-mat.other]. Université Montpellier, 2018. English. NNT : 2018MONT074 . tel-02147635

**HAL Id: tel-02147635**

**<https://theses.hal.science/tel-02147635>**

Submitted on 4 Jun 2019

**HAL** is a multi-disciplinary open access archive for the deposit and dissemination of scientific research documents, whether they are published or not. The documents may come from teaching and research institutions in France or abroad, or from public or private research centers.

L'archive ouverte pluridisciplinaire **HAL**, est destinée au dépôt et à la diffusion de documents scientifiques de niveau recherche, publiés ou non, émanant des établissements d'enseignement et de recherche français ou étrangers, des laboratoires publics ou privés.

**THÈSE POUR OBTENIR LE GRADE DE DOCTEUR  
DE L'UNIVERSITÉ DE MONTPELLIER**

**En Physique ED I2S**

**École doctorale : Information, Structures, Systèmes**

**Unité de recherche L2C - UMR 5221**

**Behaviour of a Colloid close to an Air-Water  
Interface: Interactions and Dynamics**

**Présentée par STEFANO VILLA**

**Le 26/11/2018**

**Sous la direction de Maurizio Nobili**

**Devant le jury composé de**

**Martin IN, DR, CNRS Montpellier**

**Christophe YBERT, DR, Université de Lyon I**

**Cécile MONTEUX, CR, ESPCI Paris**

**Roberto CERBINO, Professeur, Université de Milan**

**Antonio STOCCO, CR, CNRS Strasbourg**

**Maurizio NOBILI, Professeur, Université de Montpellier**

**Président**

**Rapporteur**

**Rapporteur**

**Examineur**

**Examineur**

**Directeur de thèse**



**UNIVERSITÉ  
DE MONTPELLIER**

I stand at the seashore, alone, and start to think.

There are the rushing waves...  
mountains of molecules, each stupidly minding its own business...  
trillions apart...yet forming white surf in unison.

Ages on ages...before any eyes could see...  
year after year...thunderously pounding the shore as now.  
For whom, for what?

[...]

Stands at the sea...wonders at wondering...I...  
a universe of atoms...an atom in the universe.

- *R. Feynman*, *The Value of Science* (1955)

# Contents

<b>Introduction</b>	<b>5</b>
<b>1 State of the art and theoretical background</b>	<b>7</b>
1.1 Particle-interface colloidal interactions in ionic solutions . . . . .	8
1.1.1 The Gouy-Chapman theory of the diffusive double-layer . . . . .	8
1.1.2 Double-layers interaction between two objects in a medium . . .	10
1.1.3 Air-water surface potential . . . . .	13
1.1.4 Van der Waals interaction . . . . .	14
1.1.5 Measurements of the interaction with an air-water interface . .	15
1.2 Hydrodynamic viscous drag on a spherical particle diffusing in a bounded fluid . . . . .	16
1.2.1 Full-slip and no-slip interfaces . . . . .	17
1.2.2 Viscous and incompressible liquid interfaces . . . . .	20
1.2.3 Measurements of viscous drag close to a plane boundary: state of the art . . . . .	21
1.3 Brownian motion . . . . .	22
1.3.1 Dynamics in anisotropic media . . . . .	24
1.4 Electrokinetic effects . . . . .	24
1.4.1 Electroviscous drag . . . . .	25
1.4.2 Electrokinetic lift force . . . . .	26
1.5 Spherical particles at fluid interfaces: interface crossing dynamics . . .	27
<b>2 Experimental setup and 3D tracking procedure</b>	<b>31</b>
2.1 Optical system and interference origin . . . . .	31
2.1.1 Choice of the optical method for 3D particle tracking . . . . .	31
2.1.2 Overview of the experimental setup . . . . .	33
2.1.3 Fringe formation . . . . .	37
2.1.4 Optical alignment of the setup . . . . .	39
2.2 Algorithms for the analysis . . . . .	40
2.2.1 Algorithms for spherical particles . . . . .	41
2.2.2 Resolution in the gap distance measurement . . . . .	49
2.2.3 Experimental validation of the analysis . . . . .	51
2.2.4 Algorithms for ellipsoidal particles . . . . .	53
<b>3 Materials and methods</b>	<b>61</b>
3.1 Materials' choice . . . . .	61
3.1.1 Spherical particles . . . . .	61
3.1.2 Ellipsoidal particles production . . . . .	62
3.1.3 Solutions preparation . . . . .	62
3.2 The experimental cell . . . . .	64

3.2.1	Particle's drift . . . . .	65
3.2.2	Evaporation . . . . .	65
3.2.3	Drop's shape . . . . .	66
3.3	Complementary techniques . . . . .	69
3.3.1	Conductometry and pH-metry . . . . .	69
3.3.2	Zeta Potential measurements . . . . .	69
3.3.3	Tensiometry . . . . .	70
<b>4</b>	<b>Interaction between a spherical particle and an air-liquid interface</b>	<b>71</b>
4.1	Measurements of the predicted electrostatic equilibrium . . . . .	73
4.2	Measurements of the unexpected equilibrium . . . . .	77
4.3	Interface crossing: data and discussion . . . . .	81
4.4	Modelling and discussion of the interaction potential . . . . .	85
4.4.1	Total potential energy model . . . . .	88
4.4.2	Fit of the potential energy around the first equilibrium position . . . . .	90
4.4.3	Possible origins of the second equilibrium position . . . . .	91
4.5	Conclusions . . . . .	97
<b>5</b>	<b>Dynamics of a spherical particle near an air-liquid interface</b>	<b>99</b>
5.1	Analysis of the dynamics . . . . .	99
5.1.1	Measurement of the parallel drag . . . . .	100
5.1.2	Measurement of the perpendicular drag . . . . .	102
5.1.3	Effects of vertical fluctuations and neighbourhood particles . . . . .	106
5.2	Measured drag coefficients . . . . .	108
5.3	Discussion on drag values and comparison with theoretical models . . . . .	111
5.3.1	Surface incompressibility . . . . .	111
5.3.2	Possible electrokinetic effects on the drag . . . . .	114
5.4	Conclusions . . . . .	118
<b>6</b>	<b>Conclusion and outlook</b>	<b>119</b>
	<b>Notations</b>	<b>123</b>
<b>A</b>	<b>Basics of optics and microscopy</b>	<b>127</b>
A.1	Beam properties . . . . .	127
A.2	Interference calculations . . . . .	127
<b>B</b>	<b>Evolution of tracking algorithms</b>	<b>129</b>
B.1	Evolution of the algorithm for spheres' tracking . . . . .	129
<b>C</b>	<b>Contributions to the experimental error</b>	<b>131</b>
C.1	Error on the radial coordinate arising from the azimuthal average . . . . .	131
C.2	Frequency spectrum width's contribution . . . . .	132
	<b>Bibliography</b>	<b>135</b>
	<b>Acknowledgements</b>	<b>144</b>

# Introduction

Water is fundamental for life. Its unique properties settle the biological basics of life on Earth, model the planet and at the same times fascinate researchers. The study of water is a chance to overcome the everyday risk to take it for granted and to sense its beauty and complexity. It is by far the most studied liquid and as far as mankind interrogates on reality it also interrogates on water: one among many, Thales of Miletus, the first recognized philosopher and scientist of the western civilization, devotes to water a large part of his thought, identifying it as the originating principle of nature [1].

In spite of such a long history of investigation, the more water is studied more questions emerge [2]. In particular, a largely elusive and intriguing system is water interface with air, whose structure and properties are still widely debated. Such interface in association with nano- and micro-particles plays a central role in many technologies. For example, in flotation techniques, widely employed in mineral and food processing, air bubbles are driven in waste water to adsorb micro and nano pollutants at their interface. In this process the interaction and attachment of the particle contaminants to the air-water interface of the bubble are still largely unknown [3].

Despite such important applications and fundamental open questions, the dynamics of a particle close to an air-water interface and its interaction with such interface have been poorly investigated.

Direct measurements of the interaction with an air-water interface have been mainly achieved by Surface Force Apparatus [4, 5] and Atomic Force Microscopy [6, 7]. In these experiments the force between a solid wall and an air-water interface made dispersing an air-bubble in water is measured. The results successfully agree with models considering van der Waals and electrical double-layers interactions, and point out the importance of the choice of the electric boundary conditions at the air-water interface [5]. Very recently Total Internal Reflection Microscopy (TIRM) has been adapted to investigate the particle-interface interactions for a spherical particle freely diffusing close to a water-oil interface [8]. An enhancement of interface-breaching probability with the increasing of the ionic strength of the water solution is measured, pointing out the subtle balance between attractive van der Waals and repulsive double-layers interactions. Almost unexplored remains the particle interface breaching in the case of an air-water interface, the most important case for flotation techniques, where both van der Waals and double-layers interactions should be repulsive.

The dynamics of spherical microparticles close to a liquid interface has been recently studied using different optical techniques like imaging microscopy [9], dynamic light scattering [10] and 3D digital video microscopy [11]. All these techniques have a resolution of the order of particle radius and therefore are able to measure particle dynamics at relatively large distances from the interface. In such range the obtained results agree with purely hydrodynamics predictions. At the same time, however, very recent results at shorter distances by Maali *et al.* [12] revealed anoma-

lies in the particle drag in the direction perpendicular to an air-water interface. These anomalies were attributed to surface incompressibility caused by the presence of surface active species. Moreover, electro-osmotic experiments showed that close to charged liquid interfaces electrokinetic effects can significantly alter the flow field and contribute to energy dissipation [13]. All these recent results point out the peculiarity of the dynamical behaviour of a particle in extreme vicinity to an air-water interface, suggesting that such interface can act very differently than a simple full-slip boundary.

In the present work the diffusion of a spherical microparticle close to an air-water interface is studied. The experiments are made with an adapted Dual-Wave Reflection Interference Microscope (DW-RIM) without perturbing or altering the experimental system. This approach enables the simultaneous study of both the potential energy of the particle-interface system and the particle dynamics, necessary to address the possible coupling between electrical phenomena and hydrodynamics. In addition DW-RIM allows accurate measurements of the absolute particle-interface distance without requiring any calibration or assumption on the interface location. It grants a spatial resolution higher than the ones of the previous works thus making possible the investigation of very short particle-interface distances.

In chapter 1 the state on the art of the phenomena affecting the behaviour of a spherical particle close to an air-water interface is illustrated, with a particular focus on the ones relevant for this work.

In chapter 2 the DW-RIM setup and the tracking programs developed during the PhD are illustrated.

Other informations on the materials and methods are given in chapter 3. In particular the details on solutions and particles are discussed together with a description of the experimental cell. Technical issues addressed during the preliminary phase of the work and a brief description of other complementary experimental techniques are also treated.

The experimental results are given and discussed in chapters 4 and 5. In chapter 4 the potential energy of the particle-interface system is measured from the probability distribution of the particle's positions. The system shows two different potential energy landscapes resulting in two different equilibrium particle-interface distances. The one at larger distance can be fairly explained by van der Waals and double-layers interactions combined with gravity. The one closer to the interface presents an unexpected additional attractive interaction. The possible origins of such an interaction are discussed. Moreover, the conditions promoting the particle breaching of the interface are discussed and the particle dewetting dynamics is compared with previous results present in literature [14].

Chapter 5 is devoted to the dynamics. Using a specifically developed method of analysis of the particle mean square displacements in a generic potential, the particle drag coefficients are obtained as a function of the distance from the interface. Peculiarly, the air-water interface roughly acts as a slip boundary for the particle motion parallel to the interface and as a no-slip boundary for the particle motion perpendicular to the interface. Moreover, measured particle's drag coefficients are always larger than the hydrodynamic predictions and depend on the particle's electrical charge, pointing out a possible role of electrokinetic phenomena in the particle dynamics.

# Chapter 1

## State of the art and theoretical background

The dynamics of a colloid in water close to an air-water interface is affected by the ensemble of phenomena undergoing on an object diffusing near charged boundaries. Such phenomena are essentially declined in the particle-boundary electrostatic interactions and in the hydrodynamics in an inhomogeneous medium. For spherical particles and solid boundaries these phenomena are well known and successfully described. Conversely, exhaustive experimental data and rigorous descriptions are lacking for different particle morphologies (like ellipsoids) and boundary conditions (like liquid interfaces). Moreover, the coupling of both hydrodynamics and electrostatics gives rise to a number of more complex electrokinetic effects. They have been predicted in past decades and some of them (like electrophoresis) have robust experimental evidences. Some others still remain elusive and only in last years experimental observation are starting to be published.

Besides all this, the case of the air-water interface is unique because of the peculiar characteristics of water. It is still debated the issue of the value and the origin of the electric charge density of water surface [15], whose understanding is of a paramount importance for the comprehension of the breaching dynamics by a particle of an air-water interface.

Moreover, equilibrium contact angle of a particle trapped at the air-water interface and partial wetting dynamics are far from being trivial when dealing with micrometric or nanometric particles [14].

In the present work the dynamics and the interaction of a colloidal particle with an air-water interface is experimentally studied. In order to discuss the results, in this chapter a brief review of the necessary background and of the state of the art is given.

In section 1.1 are resumed the most important elements for the description of the electrostatic interaction between two charged objects in an electrolyte. There, the origin of the electrostatic charge at the air-water interface is discussed in section 1.1.3.

Subsequently, in section 1.2 the hydrodynamics close to plane boundary conditions is described and the main experimental achievements in that field are reported. Since in the present thesis the phenomenon allowing the study of the dynamics is particle's diffusion, the classic elements of the theory of Brownian motion are also given (section 1.3).

The coupling of electrostatics and hydrodynamics is then summarized in section

1.4. There, the electrokinetic effects whose contribution has been considered in the discussion of the obtained results are described.

Finally, in section 1.5 a particle trapped at a liquid-air interface is considered. The expression for the equilibrium contact angle is given and few insights on the partial-dewetting dynamics are illustrated.

## 1.1 Particle-interface colloidal interactions in ionic solutions

The subject of the interactions between colloidal particles is an extremely wide field of research [16, 17]. In this section we will limit to discuss the essential passages to obtain the expression of the double-layers interaction pertinent to the present study and to give some elements on the theory of van der Waals interaction. In section 1.1.1 the double-layer is defined and the classic Gouy-Chapman theory for the potential generated by a charged interface in an ionic solution is resumed. In section 1.1.2 the interaction between two double-layers is described and an expression for the electrostatic potential energy is given. A focus on the charge of the water surface is then made in section 1.1.3, while the van der Waals interaction is described in section 1.1.4. Finally, the state of the art on the measurements of the interaction of particles with an air-water interface is resumed in section 1.1.5.

### 1.1.1 The Gouy-Chapman theory of the diffusive double-layer

The separation of charge that occurs at the interface between two phases is called electrical *double-layer* because it consists, ideally, of two regions of opposite charge. The simplest model of this system is the one usually attributed to Helmholtz in which both layers of charge are fixed in parallel planes to form a molecular condenser. This model was first explicitly referred to by Perrin in 1904 [18]. Although it can be used to derive some of the important electrokinetic relationship, it has long been recognized as an inadequate representation of the situation. While the charge on a metal surface may be assumed to be located in a plane, and the same is valid for many insulating solids, it is unlikely to be so in a liquid phase where the electrical forces on the ions compete with the thermal diffusive forces. The theory of such diffusive double layer was developed independently by Gouy [19] and by Chapman [20].

According to the Gouy-Chapman model, one layer of charges is assumed to be uniformly spread over a plane surface immersed in an electrolyte solution. This surface will have an electrostatic potential, the *surface potential*  $\psi_0$ . Here we will not dwell of the precise definition of  $\psi_0$ , as it is a quite intricate concept and has a definition which is more general than the one here considered. For a more complete treatment, we refer to exhaustive references such as Hunter's *Foundations of Colloid Science* [17]. In the present work we consider  $\psi_0$  as the potential generated by the uniform charges on the surface in the electrolyte solution evaluated over the surface.

The compensating ions which organize in the liquid medium around the surface are regarded as point charges immersed in a continuous dielectric medium. Noting  $\rho_q$  the volume density of charge due to ions, the electric potential  $\psi$  is determined by the Poisson equation:

$$\nabla^2 \psi = -\frac{\rho_q}{\epsilon_0 \epsilon}, \quad (1.1)$$

where  $\epsilon$  is the relative permittivity of the liquid medium and  $\epsilon_0$  is vacuum permittivity.

At equilibrium the electrical and diffusive forces on the ions must balance out:

$$\nabla\mu_i = -j_i e \nabla\psi, \quad (1.2)$$

where  $\mu_i$  and  $j_i$  are respectively the chemical potential and the valency of the ion species  $i$ , while  $e$  is the modulus of the electron charge ( $e = 1.602 \cdot 10^{-19}$  C). For a flat double layer the electrostatic potential and the chemical potential are constant in planes parallel to the wall. Noting  $z$  the direction normal to the double layer, eq. 1.2 can thus be written as:

$$\frac{d\mu_i}{dz} = -j_i e \frac{d\psi}{dz} \quad (1.3)$$

Using the definition of chemical potential (per ion) in the form:

$$\mu_i = \mu_i^0 + k_B T \ln n_i, \quad (1.4)$$

where  $n_i$  is the number of ions  $i$  per unit volume,  $k_B$  is the Boltzmann constant and  $T$  is the temperature, we obtain:

$$\frac{1}{n_i} \frac{dn_i}{dz} = -\frac{j_i e}{k_B T} \frac{d\psi}{dz} \quad (1.5)$$

Integrating this equation from a point in the bulk solution (where  $\psi = 0$  and  $n_i = n_i^0$ ) leads to Boltzmann equation:

$$n_i = n_i^0 \exp\left(-\frac{j_i e \psi}{k_B T}\right) \quad (1.6)$$

Equation 1.6 gives the local concentration of each type of ion in the double-layer region. The volume charge density in the neighbourhood of the surface is then given by:

$$\rho_q = \sum_i n_i j_i e, \quad (1.7)$$

where the summation is over all species of ion present. Replacing equations 1.6 and 1.7 in equation 1.1 we obtain the Poisson-Boltzmann equation (PB):

$$\frac{d^2\psi}{dz^2} = -\frac{1}{\epsilon_0 \epsilon} \sum_i n_i^0 j_i e \exp\left(\frac{-j_i e \psi}{k_B T}\right) \quad (1.8)$$

If  $\psi$  is small everywhere in the double-layer ( $j_i e \psi \ll k_B T$ ), we can expand the exponential in equation 1.8 obtaining the linearized PB equation as:

$$\frac{d^2\psi}{dz^2} = -\frac{1}{\epsilon_0 \epsilon} \left[ \sum_i j_i e n_i^0 - \sum_i j_i^2 e^2 n_i^0 \frac{\psi}{k_B T} \right] \quad (1.9)$$

The first term in the parentheses in the right hand of this relation must be zero to preserve electroneutrality in the bulk electrolyte. Equation 1.9 thus becomes:

$$\frac{d^2\psi}{dz^2} = \frac{\psi}{\lambda_D^2} \quad (1.10)$$

where  $\lambda_D$  is called *Debye screening length* and is defined as:

$$\lambda_D = \sqrt{\frac{\epsilon_0 \epsilon k_B T}{e^2 \sum n_i^0 j_i^2}} \quad (1.11)$$

The simplification made considering a small  $\psi$  is referred to as the **Debye-Hückel approximation**. In the considered situation of a plane double-layer where the potential varies only with  $z$ , the linearized PB equation has solution  $\psi = \psi_0 \exp(-z/\lambda_D)$ . In general, the same procedure can be followed for different geometries if the Debye-Hückel approximation's condition is satisfied. In the case of spherical symmetry, for example, the Debye-Hückel potential around a sphere of radius  $a$  and surface potential  $\psi_0$  is function of the radial coordinate  $R$  and reads:

$$\psi = \psi_0 \frac{a \exp[(R-a)/\lambda_D]}{R} \quad (1.12)$$

### 1.1.2 Double-layers interaction between two objects in a medium

The electrostatic potential energy between two objects in a liquid is determined by the distribution of ions and electrical potential in the medium surrounding the objects and by the electric boundary conditions. On the surface of each object the boundary condition usually is either a constant surface potential or a constant surface charge distribution upon overlap of the double-layers. At large separation distances, when the two double-layers don't interact, the two boundary conditions are analogous. Conversely, once the double-layers overlap, the way the two objects interact depends on the physical variable (surface charge or potential) kept constant on the interface.

Here, the interaction between the surface of an object 1 at constant surface potential  $\psi_1$  and the surface of an object 2 at constant charge density  $\sigma_2$  is considered. A single, symmetrical electrolyte of valency  $j$  is assumed. Both the surface potential and the charge density are assumed to be sufficiently small that the Debye-Hückel approximation holds. An expression for the electrostatic potential energy for two semi-infinite, plane parallel double layers is first derived. Then, using Derjaguin's approximation (valid for inter-particles distances much smaller than the particles size), the interaction energy between the corresponding spherical double-layers is obtained.

In order to determine the electric potential  $\psi$  of the system of two plane double layers, the linearized one dimensional PB equation 1.10 is solved under the boundary conditions:

$$\psi(0) = \psi_1 \quad (1.13)$$

$$\left. \frac{d\psi}{dz} \right|_{z=H} = \frac{\sigma_2}{\epsilon_0 \epsilon}, \quad (1.14)$$

where the plane 1 and 2 are located at  $z = 0$  and at  $z = H$  respectively. The second boundary condition is found exploiting the Gauss law. Noting  $k$  the reciprocal of the Debye length, the solution of eq. 1.10, with the boundary conditions given by equations 1.13 and 1.14, is [21]:

$$\psi = \psi_1 \cosh kz + \left( \frac{\sigma_2}{k\epsilon_0\epsilon} - \psi_1 \sinh kH \right) \frac{\sinh kz}{\cosh kH} \quad (1.15)$$

As described by Verwey and Overbeek [22], the potential energy per unit area  $u^{\psi-\sigma}$  correspondent to the double-layers interaction can be evaluated as the difference in free energy per unit area between the system with the two double-layers at distance  $H$  and the one with an infinite separation distance. They also shown that, for a single plane double-layer within the Deby-Hückel approximation, the free energy per unit area  $G$  is  $G = -\sigma_1\psi_1/2$  for a constant surface potential and  $G = \sigma_2\psi_2/2$  for a constant surface charge. The total free energy per unit area of the overlapping dissimilar double-layer system is therefore:

$$G(H) = \frac{1}{2} (\sigma_2\psi_2 - \sigma_1\psi_1) \quad (1.16)$$

In relation 1.16  $\psi_1$  and  $\sigma_2$  are the constant boundary conditions while  $\psi_2$  and  $\sigma_1$  depend on the distance  $H$  and can be computed respectively from eq. 1.15 and from the Gaussian law. The potential energy of double-layers interaction per unit area  $u^{\psi-\sigma}$  in the end results in [22]:

$$\begin{aligned} u^{\psi-\sigma}(H) &= G(H) - G_\infty \\ &= \frac{1}{2} \left[ 2\sigma_2\psi_1 \operatorname{sech} kH + \left( \frac{\sigma_2^2}{k\epsilon_0\epsilon} - k\epsilon_0\epsilon\psi_1^2 \right) (\tanh kH - 1) \right] \end{aligned} \quad (1.17)$$

Once the potential energy per unit area is know for the system of two parallel planes, **Derjaguin approximation** allows the calculation of the potential energy of interaction between two spheres, provided that for both spheres the condition  $ka \ll 1$  is satisfied [17]. Under such condition the spheres can be approximated as a set of parallel planar half-spaces at different distances  $H$  and the total energy can be evaluated as an integral over the plane. Noting  $d$  the gap distance between two spheres of radii  $a_1$  and  $a_2$ , the correspondent potential energy  $U(d)$  is given by:

$$U(d) = \int_d^\infty 2\pi \left( \frac{a_1 a_2}{a_1 + a_2} \right) u(H) dH \quad (1.18)$$

The evaluation of the integral for the considered case is made introducing the relation 1.17. It leads to the expression for the potential energy between two spheres with dissimilar boundary conditions:

$$\begin{aligned} U^{\psi-\sigma}(d) &= \pi \frac{a_1 a_2}{a_1 + a_2} \left[ \frac{2\psi_1\sigma_2}{k} \left( \frac{\pi}{2} - \arctan \sinh(kd) \right) - \right. \\ &\quad \left. + \left( \frac{\sigma_2^2}{k^2\epsilon\epsilon_0} - \psi_1^2\epsilon\epsilon_0 \right) \ln \left( 1 + e^{-2kd} \right) \right] \end{aligned} \quad (1.19)$$

The same procedure, using different boundary conditions, allows the calculation of the analogous expressions for the potential energy between two spherical particles with both constant surface potential ( $U^{\psi-\psi}(d)$ ) [23] or with both constant surface charge ( $U^{\sigma-\sigma}(d)$ ) [24].

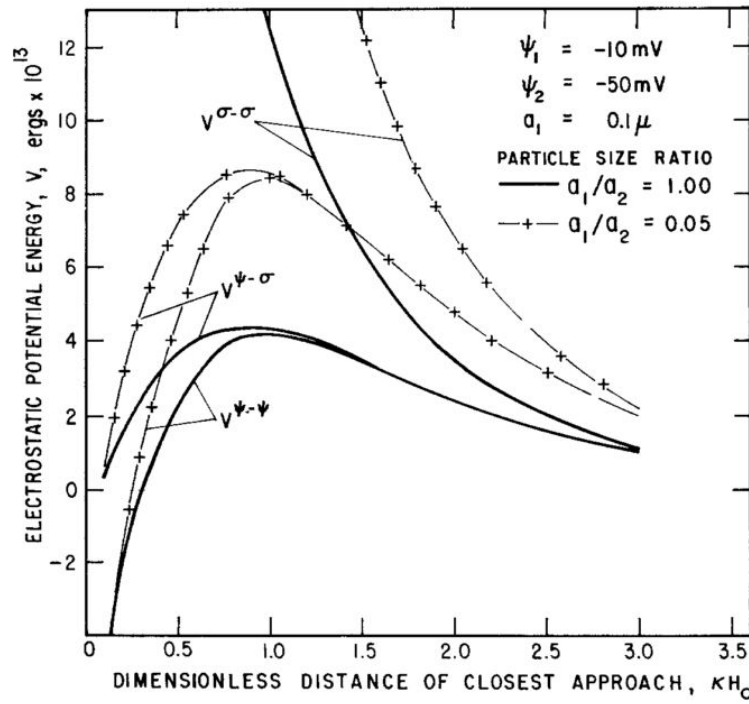


**Figure 1.1:** Plot from the paper of Kar *et al.* [21] of the electrostatic potential energy of two spherical particles immersed in an electrolyte (under Debye-Hückel and Derjaguin approximations) versus the gap distance. Differences in the nomenclature between our text and the paper are: the potential energies  $V$  (noted  $U$  in the text) and the gap distance  $H_0$  (noted  $d$  in the text). The plotted potential energies correspond to different boundary conditions: dissimilar spheres ( $V^{\psi-\sigma}$ ), both spheres with constant surface potential ( $V^{\psi-\psi}$ ) and both spheres with constant surface charge ( $V^{\sigma-\sigma}$ ). To facilitate the comparison, in the legend the surface charge density of a single particle at infinite separation is represented in terms of the corresponding surface potential.

In figure 1.1 is reported a comparison between these three possible set of boundary conditions. In all cases both spheres are negatively charged at infinite separation distance. For this reason, for constant surface charge systems the electrostatic potential energy is repulsive at all distances. Conversely, for constant surface potential and for mixed cases the potential energy is not monotonically repulsive: a potential barrier separates the long-range repulsion from a short-range attraction. This behaviour can be explained considering that, in order to keep a constant potential on one of the two surfaces while the other particle is approaching, there is a continuous readjustment of the surface charge. This effect can even induce a charge inversion over one of the particles for a sufficiently small separating distance, resulting in an attraction between the two surfaces.

### 1.1.3 Air-water surface potential

A multitude of experimental evidences exist of the accumulation of negative charges at the air-water interface and generally wherever water is in contact with an hydrophobic surface, either solid, liquid or gaseous. Qualitative evidence of this effect has been already found by Quincke in 1861 [25]. Since then, many measurements have been performed with different techniques and conditions, resulting in a wide range of surface potential values from  $-0.6$  mV down to  $-1100$  mV [4].

A widely diffused approach is the measure of the Zeta potential<sup>1</sup> of air-water surface by electrokinetic measurements [26, 27, 28] (*e.g.* detecting the mobility of air bubbles in water during electrophoresis). Recently, the Zeta potential has been measured also by optically detecting the shape distortion of an air-bubble induced by an external electric field [29]. On the other side, the measurement of the disjoining pressure of liquid films in air or between a solid wall and air allows to access to the double-layer potential of the air-water interface and the determination of the surface potential  $\psi_0$  of the interface. Disjoining pressure is studied through thin-film pressure balance (TFPB), [30, 31], atomic force microscopy (AFM) [32] and surface force apparatus (SFA) [4, 5]. Finally, interface charge density was also inferred by surface spectroscopic approaches [33, 34] which directly address the molecular composition of the air-water interface.

Concerning the origin of the electric charge of water surface, in 1996 Marinova *et al.* [35] found that the Zeta potential of an oil-water interface is independent from the nature of the oil. Moreover they also verified that the dependence of the Zeta potential from the concentration of dissolved NaCl is consistent with the typical dependence of the double-layer from  $\lambda_D$  and not with the adsorption of dissolved ions at the interface. This result excludes that the adsorption of  $\text{Cl}^-$  ions (or any other anion added to water) or any adventitious contaminations could be responsible for the water surface negative charge. These important results has been then confirmed and generalized to different hydrophobic interfaces [37, 38], including the air-water one, and for a wide range of electrolytes and surfactants [30] added to water. In particular, Beattie [36] reports the remarkably similar surface charge for the interfaces between water and air, oil and Teflon, obtained with the same Zeta potential measurement technique.

Water mainly differs from most other liquids in its high polarity and in its capability to create intermolecular hydrogen bondings. Many theoretical studies have been made to understand the way water molecules organizes at the air-water interface [39], but most have not considered the presence of the intrinsic negative charge.

It is generally agreed that the structure of water changes close to an interface and that there are some preferred orientations of the water electrical dipoles at the surface. In agreement with surface spectroscopy results [40], the most common model considers the hydrogen atoms of the water preferentially oriented to the low dielectric oil or air phase. A simple physical rationalization of this orientation is that it minimizes the image charge repulsion [41].

The listed experimental evidences are consistent with the idea that the interface of water has a typical double-layer, without adsorption of dispersed species at the interface. Moreover, the surface charge is independent from the properties of the dielectric medium forming the interface. These observations lead to the conclusion that extra charges are an intrinsic property of water surface. Dipole orientation cannot explain such effect as even if a potential difference is generated the net charge is zero. Another possible source of extra charges is the water autolysis: a possi-

---

<sup>1</sup>For the definition of Zeta potential, see section 1.4.

ble explanation is a specific adsorption of  $\text{OH}^-$  ions at the interface<sup>2</sup>. However, no definitive answers on the origins of surface water electric charge exists, as recent works also suggest other candidates like carbonate and bicarbonate ions in chemical equilibrium at the air-water interface [42].

### 1.1.4 Van der Waals interaction

Interaction between objects is possible even in the absence of a net surface charge. The presence of an attractive force between uncharged colloidal particles of the same material has long been observed but its detailed understanding took a long time to emerge [16]. This attraction is generally named van der Waals force. It arises from spontaneous electrical and magnetic polarizations, producing a fluctuating electromagnetic field within the media of the two objects and in the gap between them. There are two theoretical approaches to the evaluation of van der Waals interaction. In the classical (or microscopic) approach, due largely to Hamaker [43], the interaction between two macroscopic objects is obtained by the pairwise summation of all the relevant intermolecular interactions. All expressions obtained in this way can be split into a purely geometrical part and a constant  $A_H$ , the Hamaker constant, which is related only to the properties of the interacting macroscopic objects and the medium in which they are immersed. Typically,  $A_H$  ranges between  $10^{-21}$  J and  $10^{-19}$  J. However, the assumption of complete additivity underlying the model results in expressions always overestimating the interaction. In addition, this approach neglects retardation effects: as a matter of fact the finite propagation time of the dipole interaction causes a reduction of the correlation between oscillations in the interacting molecules and makes therefore the interaction weaker. Both non-additivity and retardation are taken into account through the use of an alternative approach proposed by Lifshitz in 1956 [44], in which the interaction is entirely derived from considerations of the macroscopic electromagnetic properties of the medium. In spite of its exactness, extensive application of the latter theory is limited by the difficulty of obtaining the necessary experimental information on the dielectric permittivity of materials and by the difficulty in its formulation for geometries different than the simplest ones.

In the Hamaker approach, the interaction between two particles is calculated through the sum of the interparticle molecular interactions. That is made by a double integration procedure leading to expressions which are simpler when the separation distance between the objects is small. For two spheres of radii  $a_1$  and  $a_2$ , separated by a gap distance  $d$ , the interaction energy at close approach ( $d \ll a_{1,2}$ ) is given by [16]:

$$U_{VdW} = A_H^{12} \frac{a_1 a_2}{6d(a_1 + a_2)}, \quad (1.20)$$

where  $A_H^{12}$  is the Hamaker constant for the media 1 and 2, of which the spheres are composed, assuming for the moment that they are in vacuum. Van der Waals interaction in vacuum is always attractive and therefore  $A_H^{12} < 0$ .

For interaction through a third medium, the same expressions can be used with a modified Hamaker constant. The Hamaker constant  $A_H^{132}$  associated to media 1 and 2 separated by medium 3 can be written as [16]:

$$A_H^{132} = A_H^{12} + A_H^{33} - A_H^{13} - A_H^{23} \quad (1.21)$$

<sup>2</sup>We refer to Beattie's dissertation [36] for more details on the reason why  $\text{OH}^-$  should be more favoured than  $\text{H}_3\text{O}^+$  to stay at the interface.

Depending on the relative magnitudes of the individual constants,  $A_H^{132}$  can be either negative or positive. In the latter case the interaction becomes repulsive. For its calculation, one has to integrate the dipolar interactions over all frequencies, and express them as an effective interaction between the two surfaces. A simple approximation [16, 45] is obtained by first considering the contribution due to dipolar interactions, given by the zero frequency dielectric constants of the materials, and then add the contribution of the entire frequency spectrum. The computation should in principle include contributions from all frequencies, but in most cases ultraviolet relaxations provide most of the interaction [46].

When compared to measurements, discrepancies of tens of percent of the Hamaker constant calculated for two materials immersed in a third one frequently arrives. That is not surprising as additional influences, like the particle coatings and the ionic strength of the solution, may alter the van der Waals interaction in a way which makes complex the precise calculation of  $A_H$ . For this reason, the Hamaker constant is often considered as an adjustable parameter, with a value chosen to fit experimental data [47, 48, 8].

In the case of the interaction between a sphere 1 of radius  $a$  and a semi-infinite plane 2 at a gap distance  $d$ , the exact expression of van der Waals potential obtained following the non-retarded derivation reads [16]:

$$U_{VdW} = \frac{A_H^{132}}{6} \left[ \frac{a}{d} + \frac{a}{d+2a} + \ln \left( \frac{d}{d+2a} \right) \right] \quad (1.22)$$

In this case the inclusion of the retardation effects does not alter relation 1.22 but just the value of the Hamaker constant [49].

### 1.1.5 Measurements of the interaction with an air-water interface

Interactions between an air-water interface and an air-bubble or a solid surface have been investigated using several methods, like TFPB [50, 51, 52], ellipsometry [53, 54], optical interferometry [55], AFM [6, 7] and SFA [4, 5].

TFPB [52] and AFM investigations [7] reveal the importance of double-layers and van der Waals interactions between air-bubbles and solid surfaces. In some situations, however, these interactions cannot alone account for the experimental results. For example, they cannot explain the way in which bubbles coalesce and the measured dynamics depend on the concentration and species of electrolyte [51]. Moreover, ellipsometric investigations of wetting films on silica surfaces reveal that additional hydration effects play a key role in that system [53].

Pushkarova and Horn [4] in 2008 and Del Castillo *et al.* [5] in 2016 studied the interaction between an air bubble and a negatively charged mica plate by SFA measurements. In their experiments, as the bubble approaches to the interface it experiences double-layer forces, until a final equilibrium wetting film between the bubble and mica surfaces is formed by van der Waals repulsion. Comparison with the theoretical models revealed that the double-layer forces become unexpectedly attractive at short range. Pushkarova and Horn tried to rationalize such behaviour by replacing the constant-charge electric boundary conditions with the ones of constant potential on both interfaces. Del Castillo *et al.* consider instead an intermediate condition of constant charge on the mica plate and constant surface potential on the air-bubble interface, providing a better agreement of the model with the experimental data.

In 2016 Helden *et al.* [8] measured by total internal reflection microscopy (TIRM) the energy potential experienced by a spherical particles close to a water-oil interface. They found a good agreement with theories taking into account van der Waals,

double-layers and gravity interactions and observed an enhancement of interface breaching probability by increasing the ionic strength of the water solution. That was expected as in that case the van der Waals interaction is attractive and dominates when double-layer interaction is screened. No systematic experimental study has been done to address the origin of interface breaching in the case of a particle freely diffusing close to an air-water interface, where the van der Waals interaction is typically repulsive.

## 1.2 Hydrodynamic viscous drag on a spherical particle diffusing in a bounded fluid

The dynamics of a particle immersed in a viscous fluid can be studied by solving the corresponding Navier-Stokes equation [56]. Considering the typical size  $a$  and velocity  $v$  of the particles measured in the present work, we can limit the discussion to the case of a Stokes (or creeping) flow, *i.e.* a flow at low *Reynolds number* ( $Re = \rho_1 va/\eta_1 \ll 1$ , where  $\rho_1$  and  $\eta_1$  are the density and the viscosity of the fluid). Noting  $p$  the pressure, the Navier-Stokes equation for incompressible fluids at low Reynolds number, the so-called Stokes equation, reads [56]:

$$\eta_1 \nabla^2 \vec{v} - \nabla p = 0 \quad (1.23)$$

It is well known that an object immersed in a fluid which translates at a velocity  $\vec{v}$  and/or rotates at an angular velocity  $\vec{\omega}$  is subjected to viscous drags (respectively  $\xi$  and  $\xi_\omega$ ). For a spherical particle in an unbounded liquid, translation and rotation are decoupled. The relation between  $\vec{v}$  (and  $\vec{\omega}$ ) and the resistive friction force  $\vec{F}_v$  (and torque  $\vec{\Omega}$ ) is obtained solving eq. 1.23 for the associated flow fields. They results in:

$$\vec{F}_v = -\xi \vec{v} \quad (1.24)$$

$$\vec{\Omega} = -\xi_\omega \vec{\omega} \quad (1.25)$$

The derivation of equations 1.24 and 1.25 can be found in the discussion of Landau and Lifshitz [56]. In the present work we are mainly interested in the translational motion and therefore we will give only explicit expressions for the translational drag coefficients. For a sphere of radius  $a$  in an homogeneous and unbounded liquid, with no-slip boundary conditions on its surface, the translational drag coefficient  $\xi_\infty$  is

$$\xi_\infty = 6\pi\eta_1 a \quad (1.26)$$

In most real situations, however the fluid is confined by rigid walls and/or fluid interfaces. In a bounded fluid, spatial homogeneity and isotropy are broken and drag coefficients are expected to depend on the position of the particle and on the direction of the motion with respect to the boundaries. Moreover, the spatial dependency of the drag induces a coupling of the particle's translational and rotational motions.

When the boundary is a plane interface, the particle's motion can be decomposed into its components in the directions parallel and perpendicular to the interface. For

a particle moving at a velocity  $\vec{v}$  the drag force it experiences is  $\vec{F}_v = \xi_{\parallel} v_{\parallel} \hat{e}_{\parallel} + \xi_{\perp} v_{\perp} \hat{e}_{\perp}$ , where  $\hat{e}$  are unit vectors and the subscripts  $\parallel$  and  $\perp$  identifies the direction respectively parallel and perpendicular to the boundary. Drag coefficients  $\xi_{\parallel}$  and  $\xi_{\perp}$  are function of the distance  $z_c$  between the particle center and the boundary (see the sketch in figure 1.2).

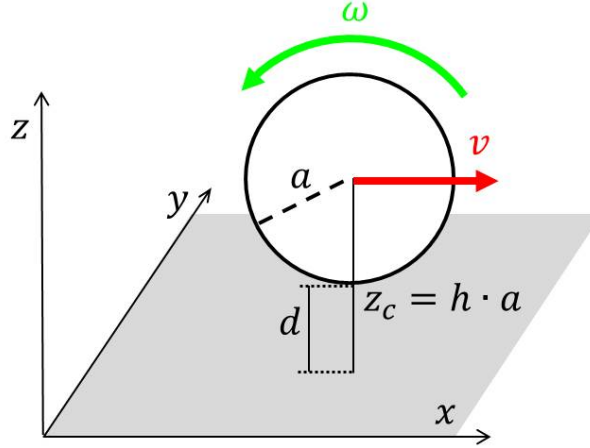


**Figure 1.2:** Sketch of the translational  $\vec{v}$  and angular  $\vec{\omega}$  velocities of a spherical particle of radius  $a$  during the motion in a bounded fluid. The fluid is bounded by a plane wall (either solid, liquid or gaseous) located in the  $xy$  plane. The  $z$ -axis is normal to the wall. The distance  $z_c$  is the one between the wall and the particle center,  $h$  is the scaled distance  $z_c/a$  and  $d$  is the gap distance between the two objects.

### 1.2.1 Full-slip and no-slip interfaces

For spherical particles analytical expressions have been calculated for drag parallel and perpendicular to a plane. The drag coefficient in the perpendicular direction was first obtained by Brenner [57]. He employed bipolar coordinates to determine the full series solution of the quasi-static Navier-Stokes equations for both full-slip and no-slip boundary conditions on the plane. These conditions reflect the two limit cases of a pure liquid-air interface (full-slip) and a solid wall (no-slip). Expressing the spatial dependency with the parameter  $h' = \cosh^{-1}(z_c/a)$ , Brenner's exact solutions for the sphere close to a plane with infinite lateral extension are:

$$\xi_{\perp}^{LA} = \xi_{\infty} f_{\perp}^{LA}, \quad (1.27)$$

with

$$f_{\perp}^{LA} = \frac{4}{3} \sinh h' \sum_{n=1}^{\infty} \frac{n(n+1)}{(2n-1)(2n+3)} \cdot \left[ \frac{4 \cosh^2(n + \frac{1}{2}) h' + (2n+1)^2 \sinh^2 h'}{2 \sinh(2n+1) h' - (2n+1) \sinh 2h'} - 1 \right] \quad (1.28)$$

for a liquid-air (LA) interface and

$$\xi_{\perp}^{LS} = \xi_{\infty} f_{\perp}^{LS}, \quad (1.29)$$

with

$$f_{\perp}^{LS} = \frac{4}{3} \sinh h' \sum_{n=1}^{\infty} \frac{n(n+1)}{(2n-1)(2n+3)} \cdot \left[ \frac{2 \sinh(2n+1)h' + (2n+1) \sinh 2h'}{4 \sinh^2(n+\frac{1}{2})h' - (2n+1)^2 \sinh^2 h} - 1 \right] \quad (1.30)$$

for a liquid-solid (LS) interface.

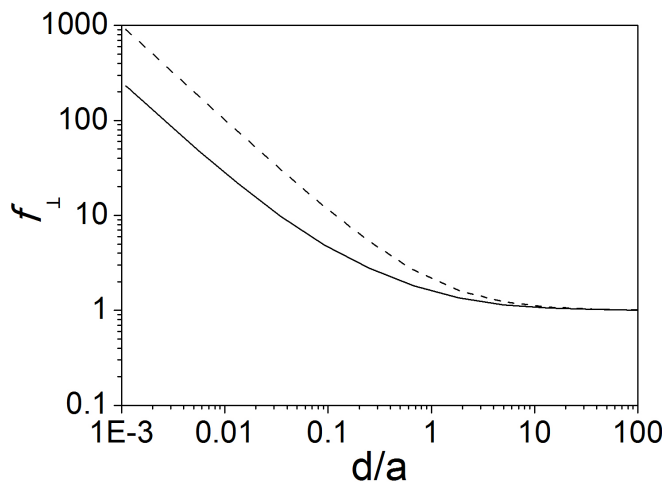


**Figure 1.3:** Adimensional perpendicular drag coefficient  $f_{\perp} = \xi_{\perp}/\xi_{\infty}$  versus  $d/a$  (the ratio between the gap distance and the radius) in the case of completely slip (continuous line, eq. 1.28) and no-slip (dashed line, eq. 1.30) boundary conditions.

In figure 1.3 the coefficients  $f_{\perp}^{LA}$  (continuous line) and  $f_{\perp}^{LS}$  (dashed line) are plotted versus  $d/a$ , where  $d = z_c - a$  is the particle-interface gap distance. For large  $d/a$  both  $f_{\perp}^{LA}$  and  $f_{\perp}^{LS}$  tend to 1 because far from the interface the drag coefficients are equal to the one of the unbounded liquid (eq. 1.26). As  $d/a$  decreases, both  $f_{\perp}$  increase ( $f_{\perp}^{LS}$  more rapidly than  $f_{\perp}^{LA}$ ).

The case of a sphere moving parallel to a plane is more complex because of the coupling between translational and rotational motion. The  $z_c$  dependency of the drag implies indeed that the viscous stress on particle's surface is different at different distances from the interface, thus implying a non-zero torque. Accordingly, the application of a translational force on the sphere generates also a rotation of the latter and similarly the application of a torque also generates a translation.

Goldman, Cox and Brenner (GCB) [58] found numerical solutions of Stokes equation for the translational and rotational drag coefficients of a sphere moving parallel to a solid wall under the influence of a simple shear flow. In the same paper two asymptotic solutions were also derived: a lubrication-theory-like approximation applicable when the particle-interface gap distance is much smaller than particle radius

( $d/a \rightarrow 0$ ) and an approximation by the method of reflections valid in the opposite limit ( $d/a \rightarrow \infty$ ).

Nguyen and Evans (NE) [59] found the corresponding exact numerical solutions for completely slip boundary conditions on the plane. They also developed approximate solutions of both their and GCB's numerical solutions for the whole range of separating distances. The relative errors of such approximations are less than 2% compared with the exact numerical results [59]. The approximated formula for  $f_{\parallel}^{LA}$  and  $f_{\parallel}^{LS}$  are:

$$f_{\parallel}^{LA} = \frac{1.106 + d/a}{1.501 + d/a} \quad (1.31)$$

and

$$f_{\parallel}^{LS} = \left\{ 1 + 0.498 \left\{ \ln \left[ 1.207 \left( \frac{a}{d} \right)^{0.986} + 1 \right] \right\}^{1.027} \right\}^{0.979} \quad (1.32)$$

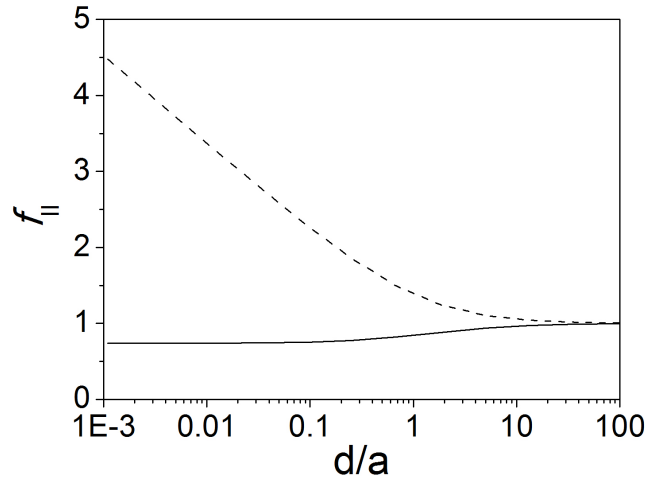


**Figure 1.4:** Adimensional parallel drag coefficient  $f_{\parallel} = \xi_{\parallel}/\xi_{\infty}$  versus  $d/a$  (the ratio between the gap distance and the particle radius) in the case of completely slip (continuous line, eq. 1.28) and no-slip (dashed line, eq. 1.30) boundary conditions.

Note that these translational adimensional drag coefficients also take into account the coupling with the rotation. In figure 1.4,  $f_{\parallel}^{LA}$  (solid line) and  $f_{\parallel}^{LS}$  (dashed line) are plotted versus  $d/a$ . In the case of the no-slip plane, the parallel drag increases when the particle approaches to the interface. The drag is however lower than the corresponding perpendicular one for same distance. Importantly, in the case of the full-slip boundary on the plane the parallel drag assumes a finite value lower than the one of the bulk as the particle approaches to the plane ( $f_{\parallel}^{LA} = 0.734$  for  $d/a = 0$ ). The decrease of the parallel drag at small distances is due to the negligible viscosity of air compared to the one of the liquid: air opposes less resistance than water to particle's motion.

The considered boundary conditions corresponding to particle's motion in a liquid near a solid wall and near a liquid-air interface are not the only possible ones. Intermediate cases are liquid-solid interfaces with partial slip boundary conditions [60] and interfaces between immiscible liquids. In the latter case the fundamental parameter is the viscosity ratio  $\eta_2/\eta_1$  between the two liquids (number 1 denotes the liquid where the particle is immersed and number 2 the other). The two cases described above (LA and LS) can be considered as two limiting cases for this situation as the viscosity ratio tends to zero and to infinite.

## 1.2.2 Viscous and incompressible liquid interfaces

Beyond the slip one treated in the previous section, fluid interfaces can also support other boundary conditions. They apply when other molecular species (surfactants, contaminants, ions,...) different from the ones of the two bulk fluids are present at the interface. Such species at the air-liquid interface affect particle dynamics in two ways. First, they produce Marangoni stresses that resist compressional interfacial flow, and second, they may result in non-zero interfacial viscosity. In the latter case, a large concentration of surface active species generates an interfacial shear viscosity which must be taken in consideration alongside the viscosities of the two medium. In 1913 Boussinesq [61] first introduced the concept of surface viscosity. Then, in 1960 Scriven [62] formulated the general constitutive relation for the viscous stresses on Newtonian interfaces of arbitrary shape. This was done by analogy with the three-dimensional case of bulk fluids, postulating the existence of independent dilatational ( $\eta_d$ ) and shear ( $\eta_{sh}$ ) interfacial viscosities. The effect of interfacial viscous stresses on particle motion has been first discussed by Davis and O'Neill in 1979 [63]. In 1998 Danov *et al.* [64] provided numerical results for the translational and rotational drag on a spherical particle of radius  $a$  as a function of particle-interface distance, surface viscosities and the viscosity ratio  $\eta_2/\eta_1$  between the bulk viscosities of the medium 2 and of the medium 1 containing the particle. The surface viscosities are expressed by the Boussinesq coefficients  $n_d = \eta_d / (a\eta_1)$  and  $n_{sh} = \eta_{sh} / (a\eta_1)$ . Danov *et al.* show that, at small distances from the interface, surface viscosity leads to an increase of particle drag. They also noted that relevant differences from the pure-interface predictions appear for  $n_d, n_{sh} \gtrsim 1$  and for values of the viscosity ratio greater than one.

The opposite limit of low concentration is governed by Marangoni stress, whose effect on the boundary conditions has been taken into consideration only recently [65]. This stress arises from the gradient of concentration of species at the interface produced by the motion of the fluid. The Marangoni stress thus opposes to the fluid motion at the interface, imposing an interfacial incompressibility to the flow. For a spherical particle oscillating in the direction perpendicular to the interface at frequency  $\nu$ , a model has been developed in 2017 by Maali *et al.* [12]. The model is made under the assumption of an ideal gas of surficial contaminants, with a surface pressure  $\Pi$  following the ideal gas law  $\Pi = c_s^i k_B T$ . Surface concentration of contaminants  $c_s^i$  follows an advection-diffusion equation [66, 67]:

$$\frac{dc_s^i}{dt} + \nabla \cdot (v_s c_s^i) = D_s \nabla^2 c_s^i, \quad (1.33)$$

where  $v_s$  is the flux velocity at the interface and  $D_s$  is the surface diffusion coefficient of the surface species. The velocity field in the water film between the air and the bead is treated in standard lubrication theory under the boundary conditions (expressed in cylindrical coordinates  $r, \varphi, z$ ):

$$v_z(z=0) = 0 \quad (1.34)$$

$$\left. \frac{\partial v_r}{\partial z} \right|_{z=0} = \frac{1}{\eta_1} \frac{\partial \Pi}{\partial r} \quad (1.35)$$

Using a finite-element method, Maali *et al.* numerically solved equation 1.33 to get the value of  $c_s^i$ , which was then used to find the surface pressure and the viscous drag force acting on the particle.

Accordingly to the model, if the typical times associated to the particle motion are large enough compared to the typical relaxation time of the gradient of  $c_s^i$  (*i.e.* if we are in the quasi-static limit) the fluid cannot flow any more on the interface because of surface incompressibility. The relative importance of the viscous force induced by the surface species is given by the ratio of the frequency  $\nu$  imposed to the particle and the frequency  $\nu_0$  given by:

$$\nu_0 = \frac{c_0^i k_B T}{8\eta_1 a} \quad (1.36)$$

If  $\nu \gg \nu_0$  the dynamics is the same as for a pure air-water interface, as expected since in the case of pure interface  $c_0^i \sim 0$  and thus  $\nu_0 \sim 0$ . Conversely, in the opposite limit  $\nu \ll \nu_0$  the dynamics is the one predicted for no-slip boundary conditions.

The treatment of the same effect in the case of the motion parallel to the interface is more complex because of the coupling with rotation and the lack of polar symmetry for the surface flow. Bławdziewicz *et al.* [65] numerically computed a solution in the case of a spherical particle translating parallel to the interface in the quasi-static limit. From their analysis it results that  $f_{\parallel}^{LA}$  is much less affected than  $f_{\perp}^{LA}$  by surface incompressibility: parallel drag is lower than in the bulk and about 14% higher than the one of the compressible case.

### 1.2.3 Measurements of viscous drag close to a plane boundary: state of the art

Measurements of particle viscous drags close to boundaries were first obtained for solid walls, because of the easier experimental conditions. Experimental evidences of enhanced drag coefficients were already found in the 1960s [68], but measurements of the  $d/a$ -dependencies have been a challenge for many years. Starting from the 2000s a number of experiments was made using different techniques like video microscopy [69], dynamic light scattering [70], total internal reflection microscopy [71] and oscillating optical tweezers [72]. These experiments validated Brenner and GCB theories for the drag close to a solid wall.

Experimental investigations of the liquid-air interface are more recent. The  $d/a$ -dependency of the parallel drag was first measured by Wang *et al.* in 2009 [9]. They studied a silica particle in water whose motion was confined by an optical trap [73]. The optical trap allowed the tuning of the distance from either an air-water or an oil-water interface. They tracked the motion of the particle parallel to the boundary by bright field microscopy and verified that the diffusivity was enhanced close to the air-water interface and reduced close to the oil-water one, accordingly to predictions. They sample the particle motion on a sequence of planes parallel to the interface spaced by 1  $\mu\text{m}$  (about 1/5 of the particle diameter) and calibrate the particle-interface distance identifying the zero distance with the position where the interfacial forces cause the particle to exit from the optical trap. This calibration has

therefore a precision limited to 100 nm, corresponding to the range where the interfacial forces become comparable to the strength of the optical trap. Consequently they were not able to measure particle drag at very short distances where it more dramatically deviates from the bulk value.

In 2014 Watari *et al.* [10] first measured the drag perpendicular to an air-water interface using a dynamic light scattering (DLS) technique based on a Michelson interferometer with a low-coherence light source. In low-coherence DLS, the depth of the scattering volume from the boundary can be controlled allowing the measurement of the diffusion coefficient as a function of the position [70]. Predictions were verified by measuring suspensions of monodisperse submicrometric particles with a spatial resolution of the order of the micrometer. As in the work of Wang *et al.*, the short range particle-interface distances were not explored.

The complete 3D trajectory of a colloidal spherical particle was measured only during the first years of this thesis by Benavides-Parra *et al.* [11]. They used 3D digital video microscopy (see sec. 2.1.1) to measure both parallel and perpendicular drag of a spherical particle of radius  $0.5 \mu\text{m}$  and for  $d/a \lesssim 10$ . Measurements were made with a  $d/a$  resolution of 0.5, in the same range as both Wang [9] and Watarai [10].

Experimental results for the motion perpendicular to the incompressible interface has been provided by Maali *et al.* [12]. The measurements were made using a spherical particle attached on an AFM tip and forced to oscillate at a given frequency. Their results have a good correspondence with the model they developed. Besides them, examples of surface incompressibility on air-water interfaces with different geometries were already reported [66, 67].

Two are the main technical difficulties which make difficult the study of the hydrodynamics at smaller distances. First, in order to probe distances  $d \ll a$  the spatial resolution in the measure either of the particle and of the interface position (the latter also affected by evaporation [10]) must be improved. Second, the repulsive long range particle-interface interactions hamper the study as they impede to reach the smallest particle-interface distances and make non-trivial the particles dynamics by confining them in not trivial potentials<sup>3</sup>.

The spatial resolutions of the reported works allow verifications of the theories of Brenner, GCB and NE but are not able to sense subtler effects recently predicted like the one of surface incompressibility on the parallel motion, for which no experimental observations are reported in literature.

### 1.3 Brownian motion

A colloidal particle immersed in a fluid shows an irregular and random walk, due to the collision of the molecules of the surrounding fluid. This effect was first observed for pollen grains immersed in water by Brown [74], from whom the effect took the name. Since then, the Brownian motion has been found in an extremely wide variety of systems, including many of the soft matter and biological fields [75]. The physical essence of Brownian motion is substantially thermal fluctuations: fluid molecules move by thermal energy and kick the particle causing a random force  $\vec{F}_r(t)$  acting on it. At the same time the particle is also subjected to a viscous dissipative force  $\vec{F}_v$  opposing the motion.

The equation of motion, known as *Langevin equation*, of a Brownian particle of mass  $m$  when it is not subjected to additional external forces reads:

<sup>3</sup>This problem will be widely discussed in chapter 5.

$$m \frac{d^2 \vec{x}}{dt^2} = \vec{F}_r - \xi \frac{d\vec{x}}{dt} \quad (1.37)$$

Since the random force has not an analytical expression, it is not possible to obtain an exact solution of eq. 1.37. A description of the motion can however be made as it follows. Considering the projection of the vectorial equation 1.37 along a generic direction  $x$ , let's multiply both sides of it by  $x$  and consider the ensemble average of all the terms:

$$m \left\langle x \frac{d^2 x}{dt^2} \right\rangle = \langle x F_r \rangle - \xi \left\langle x \frac{dx}{dt} \right\rangle \quad (1.38)$$

The first term in the right hand side is zero as  $F_r$  is a random force. The term averaged in the left hand side can instead be developed as:

$$x \frac{d^2 x}{dt^2} = \frac{d}{dt} \left( x \frac{dx}{dt} \right) - \left( \frac{dx}{dt} \right)^2 \quad (1.39)$$

Taking into account the equipartition theorem, *i.e.*  $k_B T \sim \langle m (dx/dt)^2 \rangle$ , equation 1.38 becomes:

$$m \frac{d}{dt} \left\langle x \frac{dx}{dt} \right\rangle = k_B T - \xi \left\langle x \frac{dx}{dt} \right\rangle \quad (1.40)$$

By solving eq. 1.40 with respect to the variable  $\langle x dx/dt \rangle$ , imposing the initial condition  $x = 0$  and then integrating over time we obtain:

$$\langle x^2 \rangle = \frac{2k_B T}{\xi} \left[ t - \tau_p \left( 1 - e^{-t/\tau_p} \right) \right], \quad (1.41)$$

where  $\tau_p = m/\xi$ .

At short times ( $t \ll \tau_p$ ), the exponential function is safely approached by its development in the Taylor series and equation 1.41 becomes:

$$\langle x^2 \rangle = \frac{k_B T}{m} t^2 \quad (1.42)$$

Thus, for short time scales with respect to  $\tau_p$ , the particle shows a ballistic motion at constant velocity  $v = \sqrt{k_B T/m}$ , as expected from equipartition theorem after a single molecular random kick. A direct verification of this prediction has been recently provided by a measurement of the instantaneous velocity of silica beads trapped in optical tweezers [76].

In the opposite case,  $t \gg \tau_p$ , the mean square displacements results in:

$$\langle x^2 \rangle = 2Dt \quad (1.43)$$

In this case the effect of several random molecular collisions translates in a diffusive regime, where  $\langle x^2 \rangle$  linearly increases in time. In equation 1.43,  $D$  is the *diffusion coefficient* defined as:

$$D = \frac{k_B T}{\xi} \quad (1.44)$$

### 1.3.1 Dynamics in anisotropic media

As seen in section 1.2, in inhomogeneous systems the viscous dissipation is anisotropic and therefore the particles diffuses in presence of drag gradients. This causes the insurgence of additional forces acting over the particles.

For a particle moving close to an infinite plane boundary lying on the  $xy$  plane, the only non-zero drag gradients are those along  $z$ , *i.e.*  $\partial\xi_{\parallel}/\partial z$  and  $\partial\xi_{\perp}/\partial z$  (henceforward denoted with  $\xi'_{\parallel}$  and  $\xi'_{\perp}$  for brevity). Under suitable conditions they both can generate a force: an hydrodynamic lift (caused by  $\xi'_{\parallel}$ ) and a drifting force related to the Brownian diffusion (caused by  $\xi'_{\perp}$ ).

The *hydrodynamic lift* originates from the perturbation of the flow field due to particle's motion. In the case of motion parallel to a solid wall, the situation where the perturbation operated by the interface is the highest, in 1977 Cox and Hsu [77] obtained analytical expressions for the lift velocity  $v_l$  away from the interface. Their results are valid for small gap distances and depend on the Reynolds numbers associated to particle's diameter ( $Re_a = \rho_1 2av_{\parallel}/\eta_1$ ) and to the distance between the center of the sphere and the interface ( $Re_z = \rho_1 z_c v_{\parallel}/\eta_1$ ). The expected  $v_l$  they found reads [77, 78]:

$$v_l = \frac{3}{64} Re_a v_{\parallel} \left[ 1 - \frac{11}{32} Re_z^2 + \dots \right] \quad (1.45)$$

Concerning the drift term in diffusion, it originates from the Brownian motion in the direction  $z$  normal to the interface. Following the derivation of Yang and Ripoll [79], viscous force acting on a diffusive particle in presence of a gradient of drag  $\xi'_{\perp}$  reads:

$$F_v(z) = -\frac{1}{\Delta t} \left( \xi_{\perp} \langle \Delta z \rangle + \frac{1}{2} \xi'_{\perp} \langle \Delta z^2 \rangle \right) \hat{z}, \quad (1.46)$$

where  $\Delta z$  is the displacement along  $z$  occurring in a time interval  $\Delta t$ . The first term is the one given in equation 1.24 for a homogeneous system and always opposes to  $v$ . The second term can be rewritten using equation 1.43 as

$$F_v^{II}(z) = -k_B T \frac{\xi'_{\perp}}{\xi_{\perp}} \hat{z} \quad (1.47)$$

It is dependent from  $\xi'_{\perp}$  and is always directed in the direction opposite to the gradient. In our specific case it is therefore a force which pushes the particle away from the interface. Intuitively, it can be seen as a spontaneous drift of the particle which, randomly diffusing, when it gets away from the interface moves faster than when it moves towards it due to the different  $\xi_{\perp}$ . The consequence is a net displacement towards regions at lower drag.

## 1.4 Electrokinetic effects

In the previous sections we separately analysed electrostatic and hydrodynamic phenomena. However, in real systems they are often interconnected. Consider now the double-layer originated by the presence of a charged phase (an object, either solid, liquid or gaseous) immersed in a liquid electrolytic phase. When one of the two phases moves relatively to the other phase, the double-layer is perturbed by the

flow. From the coupling of hydrodynamics and electric forces a number of phenomena arise which are grouped under the name of *electrokinetic effects*. There are four distinct effects depending on the way in which the motion is produced [81]:

- *electrophoresis*: the object is induced to move applying an external electric field,
- *electro-osmosis*: the object remains stationary and the ions moves in response to an external electric field,
- *streaming potential*: a flow is induced in the solution which accumulates downstream the charges causing an electric field (the opposite of electro-osmosis) and
- *sedimentation potential*: charged objects moves under gravity dragging the double-layer and generating a potential difference (the opposite of electrophoresis).

An important concept related to electrokinetic effects is the *Zeta potential*. Let's define the *surface of shear* as an imaginary surface, close to the object surface, enclosing a volume where the fluid is always stationary. Since the liquid within the surface of shear follows the motion of the object, an effective potential can be defined. It is directly related to the mobility of the particle [80, 81] and includes the effects of the surface potential and of the charges contained in the surface of shear. This potential is named Zeta potential ( $\zeta$ ) and has a central role in the electrokinetic properties of an object. As a matter of fact, it is the measured quantity in electrophoresis experiments.

Operatively, the evaluation of electrokinetic effects is made coupling the Poisson equation governing the electric potential and the ionic convective-diffusion equation determining the distribution of ionic charges in the liquid. The solution of this set of equations is a formidable task even in the simplest geometries and for this reason most of the works in literature deal with analytical approximations in the limit of low *Peclet number*, corresponding to convective dynamics small compared to the diffusive one. The Peclet number is defined as  $Pe = aU/D_i$ , where for our system  $a$  is the size of the object,  $U$  the typical velocity and  $D_i$  the diffusion coefficient of the electrolytes. The approach usually adopted is the evaluation of the total stress tensor acting on the particle which is the sum of the hydrodynamic and the electrostatic Maxwell stress tensors.

Here we report two effects which can be relevant in the case of a micrometric particle moving near a plane boundary [82]: the electroviscous drag and the electrokinetic lift.

### 1.4.1 Electroviscous drag

Electrokinetics is source of additional dissipations not included in purely hydrodynamic treatments of section 1.2. Dissipation essentially arises from the distortion of the double-layer due to the flux. This modification, in turn, alters the local hydrodynamic flow around the particle leading to an increment of energy dissipation. That remains valid even in the case of a stationary motion, as the ions of the double-layer are dragged away and a flux of new ions is attracted by the particle. This latter flux is the responsible of the additional dissipation.

In 1984 Oshima *et al.* [83] derived an expression for the electroviscous drag  $\xi_{ev}$  for a charged spherical particle translating in a bulk solution containing two ionic species with valency  $j_i$ , diffusivity  $D_i$  and bulk number density  $n_i^0$  (subscripts  $i = 1, 2$  refer to counter-ions and co-ions respectively). In the limit of  $Pe \ll 1$  and  $k \ll a$  they found for the electroviscous drag  $\xi_{ev}$  the following expression [84]:

$$\xi_{ev} = \frac{48\pi (\epsilon_0\epsilon)^2 (k_B T)^3}{e^4 (n_1^0 j_1^2 + n_2^0 j_2^2) a} \left( \frac{G_p^2}{j_1^2 D_1} + \frac{H_p^2}{j_2^2 D_2} \right), \quad (1.48)$$

where  $G_p$  and  $H_p$  are functions of the particle's Zeta potential, defined as:

$$G_p = \ln \left[ \frac{1 + \exp\left(\frac{j_1 e \zeta_p}{2k_B T}\right)}{2} \right] \quad (1.49)$$

$$H_p = \ln \left[ \frac{1 + \exp\left(\frac{j_2 e \zeta_p}{2k_B T}\right)}{2} \right] \quad (1.50)$$

In the same limits Tabatabaei *et al.* [85] in 2006 found an expression of the electroviscous force acting on a spherical particle moving parallel and close ( $d \ll a$ ) to a solid plane no-slip boundary having a Zeta potential  $\zeta_w$ . Considering a symmetric electrolyte ( $n_1^0 = n_2^0 = n^0$  and  $j_1 = j_2 = j$ ), the drag force  $F_{ev,\parallel}$  reads [85, 84]:

$$\begin{aligned} F_{ev,\parallel} = & \frac{8\pi (\epsilon_0\epsilon)^2 (k_B T)^3 a^2}{5j^4 e^4 n^0 a} \frac{a^2}{d^2} \cdot \\ & \cdot \left[ \frac{1}{5} \left( (7G_p + 2G_w) \frac{G_p + G_w}{D_1} + (7H_p + 2H_w) \frac{H_p + H_w}{D_2} \right) (v + a\omega) + \right. \\ & \left. - \left( (\alpha_1 G_p + \alpha_2 G_w) \frac{G_p - G_w}{D_1} + (\alpha_1 H_p + \alpha_2 H_w) \frac{H_p - H_w}{D_2} \right) (v - a\omega) \right], \end{aligned} \quad (1.51)$$

where  $\alpha_1 = 10.80625$ ,  $\alpha_2 = 4.94467$ , and  $v$  and  $\omega$  are the particle translational and angular velocities. The quantities  $G_w$  and  $H_w$  are defined for the wall in the same way as  $G_p$  and  $H_p$  are defined for the particle in equations 1.49 and 1.50.

The interesting point of relation 1.51 is that the parallel electroviscous drag increases as  $a^2/d^2$  approaching to the boundary. Accordingly, at very small distances the electroviscous drag increases much more rapidly than the hydrodynamic one (eq. 1.32).

## 1.4.2 Electrokinetic lift force

The motion of a charged spherical particle parallel to a charged surface leads to an electrokinetic lift force perpendicular to the surface, discovered in 1987 by Prieve and Bike [86]. An analytical expression for a cylindrical particle moving along a surface has been first derived by Wu *et al.* [87] by assuming that the Maxwell stress tensor due to the flux perturbation of the cloud of charges gives the dominant contribution to the force. They observed huge discrepancies between experiments and theory. In his general theory, Cox [88] reconciled these discrepancies showing that indeed the dominant contribution to the electrokinetic lift force comes from the hydrodynamic stress arising from the electroviscous flow along the surface of the particle.

The result for the lift force on a cylindrical particle has been used by Warszynski [89] to estimate the lift force on a different geometry. In the case of a solution with two ionic species, the resulting expression for the lift force  $F_{EL}$  exerted on a charged spherical particle moving parallel to the charged no-slip boundary has the form[89]:

$$F_{EL} = \frac{\epsilon\epsilon_0}{D_s^2 k^2} \left( \frac{k_B T}{je} \right)^2 \frac{G^2 a^2}{(h-1)^2} \frac{D_+ I_p^- + D_- I_p^+}{16(D_+ + D_-)^2} \left[ h - 1 + \frac{8}{3} (f_{\parallel}(h) + f_{\omega}(h)) \right] \cdot (g_1(h) + u_1(h) + w_1(h)), \quad (1.52)$$

where

$$g_1(h) = 8(h-1) \left[ D_- (I_p^+ + I_s^+) + D_+ (I_p^- + I_s^-) \right] \quad (1.53)$$

$$w_1(h) = f_{\omega}(h) \left[ D_- (9I_p^+ + I_s^+) + D_+ (9I_p^- + I_s^-) \right] \quad (1.54)$$

$$u_1(h) = f_{\parallel}(h) \left[ D_- (I_p^+ + 9I_s^+) + D_+ (I_p^- + 9I_s^-) \right], \quad (1.55)$$

and  $f_{\parallel}(h)$  and  $f_{\omega}(h)$  are the adimensional hydrodynamic drag coefficients for the tangential and rotational motion respectively close to the interface.

The other physical quantities introduced in 1.52 are: the flow rate  $G$ , the positive and negative ions bulk diffusion coefficients  $D_+$  and  $D_-$ , and  $D_s$ , which is defined as  $D_s = 2D_+D_-/(D_+ + D_-)$ .

Finally  $I_{p,s}^+$  and  $I_{p,s}^-$ , distinguished for the particle and the plane by the subscripts  $s$  and  $p$ , are defined as

$$I_{p,s}^{\pm} = \mp \bar{\zeta}_{p,s} + 4 \ln \left[ \cosh \left( \frac{\bar{\zeta}_{p,s}}{4} \right) \right], \quad (1.56)$$

with

$$\bar{\zeta}_{p,s} = \frac{je\zeta_{p,s}}{k_B T} \quad (1.57)$$

## 1.5 Spherical particles at fluid interfaces: interface crossing dynamics

In addition to the interactions reported in the previous sections, once the particle finds itself in contact with two different media a decisive role on its static and dynamic properties is played by surface tension. Surface tension  $\gamma_{lm}$  represents the free energy necessary to increase by one unit the area of contact between two different phases  $l$  and  $m$  [90]. The physical origin of this free energy relies in the molecular interactions: inside a phase  $l$ , the molecules attract each other, and they can better interact with neighbours of the same species  $l$  when located in the bulk medium than when located close to the interface with the other medium  $m$ .

When a solid particle  $P$  is at the interface between air  $A$  and water  $W$ , three interfaces ( $P$ - $W$ ,  $P$ - $A$ ,  $W$ - $A$ ) have to be considered. Each of them contributes to the total

surface free energy  $U_S$  by a term equal to the area of the surface times the respective surface tension ( $\gamma_{PW}$ ,  $\gamma_{PA}$  and  $\gamma_{WA}$ ). From simple geometrical arguments it is possible to recover  $U_S$  [91] as (see figure 1.5):

$$U_S = \frac{1}{\pi a^2 \gamma_{WA}} \left[ \frac{z_c^2}{a^2} + \frac{z_c}{a} \left( \frac{\gamma_{PA} - \gamma_{PW}}{\gamma_{WA}} \right) + \frac{2\gamma_{PW} + 2\gamma_{PA} - \gamma_{WA}}{\gamma_{WA}} \right] \quad (1.58)$$

The total surface free energy has therefore a parabolic profile as a function of  $z_c/a$ . The equilibrium position is obtained by imposing  $\partial U_S / \partial z_c = 0$ :

$$z_c = -a \frac{\gamma_{PA} - \gamma_{PW}}{\gamma_{WA}} \quad (1.59)$$

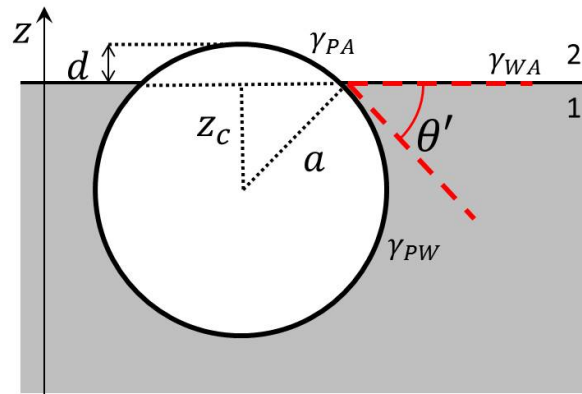


**Figure 1.5:** Scheme for a spherical particle of radius  $a$  at the fluid interface between two media 1 (water) and 2 (air). In the figure are indicated the distance  $z_c$  between the center of the particle and the interface, the distance  $d = a - z_c$  and the surface tensions between particle and water  $\gamma_{PW}$ , particle and air  $\gamma_{PA}$  and water and air  $\gamma_{WA}$ .

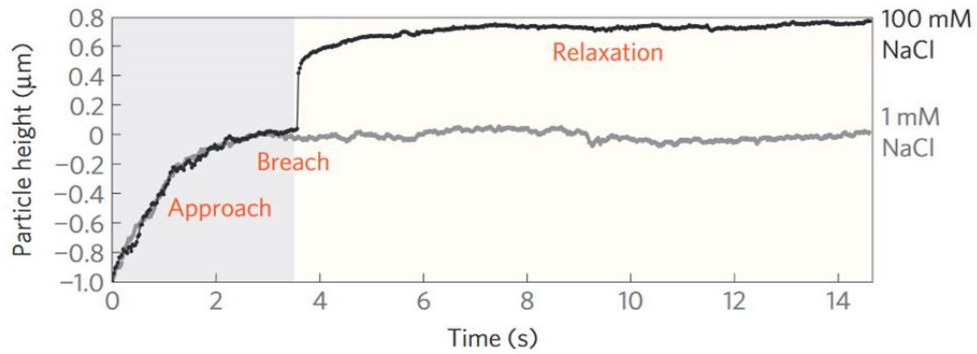
Defining the contact angle  $\theta'$  as the one between the wetted part of the particle and the air-water interface (figure 1.5), relation 1.59 can be re-written in the form of the Young law [92]:

$$\gamma_{WA} \cos \theta' = \gamma_{PA} - \gamma_{PW} \quad (1.60)$$

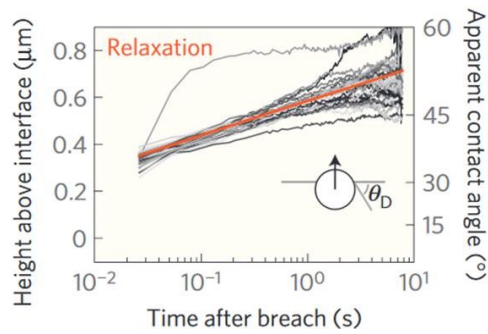
The contact angle depends therefore from the surface tensions between the three phases.

Young's law (eq. 1.60) provides the equilibrium position of a bead at the interface, but little is known about how such equilibrium is achieved. Recently Kaz *et al.*[14] observed the breaching dynamics of a spherical particle at a decane-water interface and the successive relaxation toward the equilibrium position (fig. 1.6(a)). This relaxation follows a logarithmic trend with characteristic times of months (fig. 1.6(b)).

Such a slow dynamics cannot be explained by viscous dissipation. Kaz *et al.* proposed a model based on thermally activated jumps of the contact line over surface heterogeneities and defects, considered as sites where the contact line is pinned.



(a)



(b)

**Figure 1.6:** Data reported in Kaz *et al.*[14]. (a) Typical time evolution of the distance between the interface and the top of a  $1.9\ \mu\text{m}$ -diameter polystyrene spherical particles breaching a decane-water interface. They associated the sharp transition in the 100 mM curve to the particle breaching of the interface. (b) A semi-log plot of the after-breaching trajectory versus time showing that the relaxation is approximately logarithmic. Each grey line is a trajectory for a different particle. The red line shows a logarithmic fit to the average of the data.

Close to equilibrium, the time evolution of the distance  $d$  between the interface and the top of the particle (figure 1.5, where now medium 2 is decane) follows the equation:

$$d = \frac{2ak_B T}{A\gamma} \ln \left( \frac{A\gamma_{12}}{2ak_B T} \tilde{\nu} a^* t \right), \quad (1.61)$$

where  $A$  is the mean defects area,  $a^*$  is the radius of the equilibrium wetted section of the particle and  $\tilde{\nu}$  is a frequency representing the reciprocal of the time scale for the contact line to hop over a defect. Kaz *et al.* used this model to fit the data taking  $A$  and  $\tilde{\nu}$  as fitting parameters. As explained in [93], at their experimental acquisition frequency it was not possible to access to the extremely short time scales of  $1/\tilde{\nu}$  and therefore from the fit they only recovered  $A$ . The values for  $A$  they found range from  $1 \text{ nm}^2$  to  $30 \text{ nm}^2$ , depending on the type of the particle but not on its size. Moreover, the defect area are of the same order of the area per charged group of the particle, even if the physical origin (charges, roughness,...) of the defects remains unclear.

Their results show that in many practical applications, a particle trapped at an interface is not at the equilibrium contact angle predicted by Young's law (eq. 1.60).

## Chapter 2

# Experimental setup and 3D tracking procedure

In order to investigate the motion dynamics of a colloidal particle close to an air-liquid interface and its interaction with the interface, we have developed dedicated techniques able to track all the degrees of freedom of the particle motion.

The experimental method is a dual wave reflection interference microscopy (DWRIM), based on the video recording of an interference pattern arising from the particle-interface system and in home-made algorithms able to reconstruct the particle's three dimensional trajectory and, for ellipsoids, orientation.

In section 2.1 the interferometric setup used to record the dynamics of the particles is described, then in section 2.2 the algorithms used to extract particles' position and orientation from the interference patterns are illustrated.

### 2.1 Optical system and interference origin

To obtain high resolution measurements, a lot of effort was put into the optimization of a custom setup initially designed by C. Blanc. All the degrees of freedom of the motion of the spheres and of the ellipsoids have to be tracked. For the spheres, the tracking involves the cartesian coordinates  $x$ ,  $y$  and  $z$ , where  $xy$  is a plane parallel to the interface (fig.2.1(a)) and  $z$  is its normal (fig. 2.1(b)). For the ellipsoids, the azimuthal angle  $\varphi_e$  in the plane  $xy$  and the tilt angle  $\theta_e$  with respect to the  $z$ -axis also have to be measured.

#### 2.1.1 Choice of the optical method for 3D particle tracking

Several optical techniques allow three dimensional (3D) particle tracking, but most of them are not easily adaptable to the air-liquid interface geometry.

One common technique which reaches a 10 nm spatial resolution is the **holographic microscopy**. It exploits the in-line holography, *i.e.* the interference between a laser beam transmitted from the sample and a coaxial reference beam incoming from the same source. The resulting interference pattern gives access to the whole particle scattered electric field (amplitude and phase), which in turns gives the 3D position and the size of the particle. This technique has rarely been employed for the study of non-spherical colloids because of the complex work on the scattering properties of the particles it requires [94, 95], resulting in a extremely time-consuming data analysis. Additionally, the use of this technique for the tracking of particles

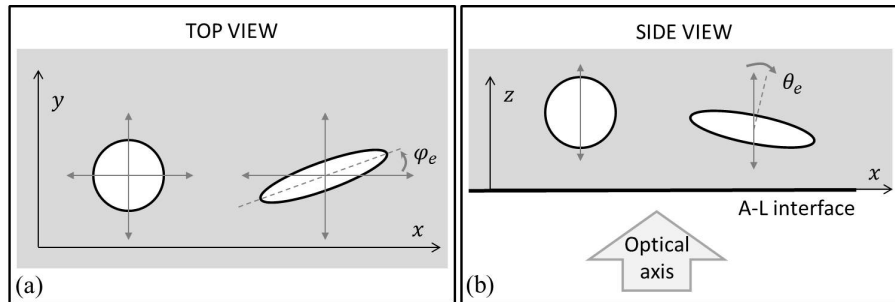


Figure 2.1: Definition of the degrees of freedom of the particles: (a) top view, in a plane  $(xy)$  parallel to the interface, (b) side view, in a plane containing the interface normal  $z$ .

close to an interface imposes a supplementary constraint of index matching between the two media of the interface in order to avoid optical artefacts. As a consequence holographic microscopy is employed for measurements of particles near water-oil interfaces [14] but cannot be easily employed in the case of an air-liquid interface. The request of index matching brings the further drawback of an optically undetectable interface. Hence, a direct determination of the particle position with respect to the interface is impossible. The relative displacements of the particle are measured but the real distance between the interface and the particle has to be inferred [14].

A second technique usually employed for the study of particles close to interfaces is the **total internal reflection microscopy (TIRM)**. It is an evanescent light-scattering method allowing the determination of the distance between a particle and a flat wall from the particle's scattering intensity. The wall is usually a solid one but recent works proved the capability to extend such technique to liquid interfaces [8, 96, 97]. The experimental procedure consists in illuminating the particle with an evanescent field created by total internal reflection of a laser beam at the interface. Since the scattering intensity at the interface is not known a priori, only the relative motion of the particle is detected and the absolute distance has to be found with a calibration. In order to allow total internal reflection, the medium containing the particle must have a refractive index lower than the one containing the incident beam. For this reason also this technique cannot be implemented for air-liquid interfaces.

A third method which has been recently employed is the **three-dimensional digital video microscopy (DVM-3D)**. This technique takes advantage of the diffraction pattern generated by a particle located below the focal plane of the microscope objective. The diffraction pattern consists of a series of concentric rings, the size of which is a monotonically increasing function of the distance between the colloid and the focal plane. Such property is used to quantify the separation distance with a resolution in  $z$  of the order of 100 nm [69, 98, 99]. DVM-3D has therefore a lower precision (10 times) than holographic microscopy, but has the advantage to have no restrictions on the refractive indexes of the two media, making possible its application to the study of an air-liquid interface [11]. As all the cited methods, however, it only detects the particle relative displacement, thus requiring a calibration to know the absolute distance.

The need of a calibration is therefore a disadvantage common to all the described methods. It is usually settled by comparing the measured particle's viscous friction with the distance-dependent one predicted by hydrodynamics [14, 8]. It is worth noting that this procedure prevents the experimental detection of possible deviations

from the predicted interactions and particle dynamics behaviour which was one of the objectives of this thesis.

The calibration drawback is avoided if **confocal microscopy** is used. Confocal microscopy reconstructs 3D trajectories from stacks of images taken at different focal planes [100]. The disadvantage here comes from the scanning limitation imposed by the piezo velocity impeding the use of such technique for fast dynamics [101]. Possible solutions can be to reduce the mobility of the particle increasing the viscosity of the medium [102] or to reduce the spatial resolution of the tracking to increase acquisition velocity [103]. Both solutions, however, prevent the study of the dynamics of a particle close to the air-water interface because to change the viscosity one has to change the liquid while the increasing of acquisition velocity prevents a spatial resolution sufficient to detect Brownian motion.

The technique that proved to satisfy the requested criteria is bright field microscopy coupled with interferometry. The interference arises from the superimposition of light beams reflected from the interface and from the particle surface (sec. 2.1.3). This technique allows obtaining the particle-interface distance since such information is encoded in the interference pattern (sec. 2.2.1). In this way there is no need of calibration. The only request on the two media forming the interface and on the particle is to have refractive indexes assuring a good contrast of the fringes (sec. 3.1). Moreover thanks to a simple optical geometry this method can be easily adapted to different shapes and different refractive index jumps only by simple geometrical calculations without needing heavy computational efforts to evaluate the scattered fields [104] (sec.2.2).

## 2.1.2 Overview of the experimental setup

In our experimental system, a cylindrical cell containing the liquid is putted upside down. The liquid is therefore the upper phase while air is the lower one. This configuration allows particles with densities larger than the one of the liquid to sediment towards the interface. The optical system is assembled similarly to an inverted microscope in order to work in reflection. A simple scheme of the interference mechanism is given in fig. 2.2: the source light beam hits the sample from below and is both back-reflected from the air-liquid interface and from the particle. The superposition of the two reflected beams gives rise to the measured interference.

A sketch of the microscope is illustrated in fig.2.3. In 2.3(a) the illumination part of the system is highlighted. Three light sources are employed. Two are monochromatic and are used for the interferometry. The third one is a white light used in transmission for the bright field imaging of the particle. It is used to adjust particle's position in the center of the field of view. White transmitted light is employed because a high-intensity illumination permits to detect a particle (even located far from the focal plane). The lamp housing used is a *Leitz Wetzlar Halogen 12V - 100W Lamphouse* with a tunable intensity and is located above the sample.

The two monochromatic sources, a red one (nominal wavelength  $\lambda_R = 625$  nm) and a blue one (nominal wavelength  $\lambda_B = 505$  nm), are based on light-emitting diodes (LED)<sup>1</sup>. Two wavelengths are needed to recover from the interference pattern the absolute distance of the particle from the interface (sec.2.2.1).

The choice of LEDs as monochromatic light sources is motivated by the order of magnitude of their coherence length<sup>2</sup>  $l_c$ . A simple estimation of  $l_c$  can be made in the case of a Gaussian spectrum as [105]:

<sup>1</sup>Thorlabs collimated LEDs M625L3-C2 and M505L3-C2.

<sup>2</sup>The coherence length is defined as the distance at which the visibility of the fringes is reduced by 50%

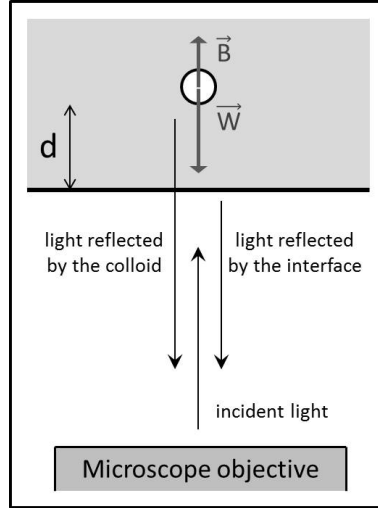


Figure 2.2: Reflection geometry for a colloidal particle immersed in a liquid close to the interface. In the sketch  $d$  is the particle-interface distance,  $\vec{B}$  is buoyancy force and  $\vec{W}$  is the particle weight. A colloid sediments towards the interface due to gravity. The incident light beam coming from below is reflected from both the interface and the particle. The reflected beams are both collected by the objective. Their superposition generates the interference pattern.

$$l_c = \sqrt{\frac{2 \ln 2}{\pi n} \frac{\lambda^2}{\Delta \lambda}}, \quad (2.1)$$

where  $n$  is the refractive index of the medium,  $\lambda$  the wavelength of the source and  $\Delta \lambda$  the full width at half maximum (FWHM) of its spectrum. For the LED used in the present work, formula 2.1 gives a coherence length of  $13 \mu\text{m}$  and  $5 \mu\text{m}$  for red and blue respectively. Coherence lengths of this order satisfy the two conditions for the formation of a low-noise fringe pattern. First, they allow fringes formation since they cover more than the double of the optical path between the colloid and the interface (see 2.1.3), which is typically of the order of a micrometer for the phenomena we study. Second, they are sufficiently short to prevent additional interference from reflections coming from other surfaces (internal reflection of the colloids, reflection of the lenses, of the dust on the lenses, of other particles far from the interface, of the upper side of the cell, ...) In figure 2.4(a) it is possible to see how a low-coherence laser ( $l_c < 300 \mu\text{m}$ ) illumination leads to additional fringes which are not observed using a red LED source (figure 2.4(b)).

Following the optical path in figure 2.3(a), the two LEDs (1, 2) are mounted on two different cage systems. In cages' connection a beam splitter (3) superimposes the two emitted beams. To correct the slight divergence of the beams, a lens<sup>3</sup> (4) is mounted after the beam splitter, at the entrance of the tube<sup>4</sup> (dashed line in figure 2.3) containing the imaging part of the setup. In order to align the beam axis with the one of the microscope the lens is mounted on a translator equipped with micrometric screws allowing the motion along the two axes perpendicular to the optical axis.

<sup>3</sup>Bi-Convex Lens,  $\varnothing 1''$ ,  $f = 30.0 \text{ mm}$ , ARC: 350-700 nm.

<sup>4</sup>*InfiniTube<sup>TM</sup> FM-200 System.*

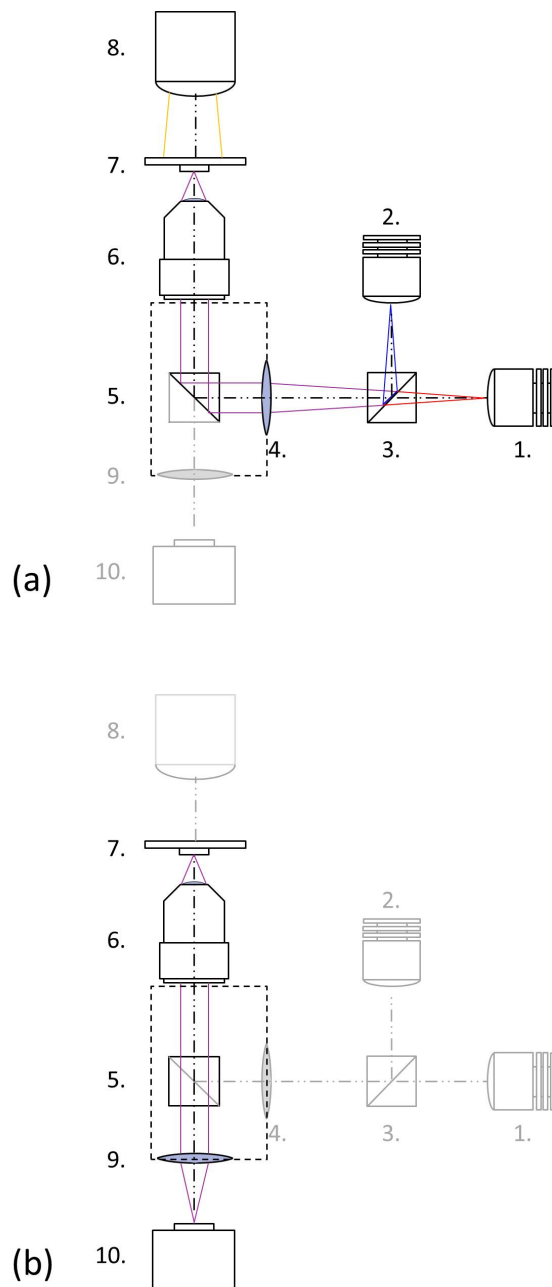


Figure 2.3: Scheme of the optical components of the setup. In (a) the illumination system and in (b) the imaging system are highlighted and the corresponding beams are sketched. Numbers correspond to the following elements: (1) red 625 nm LED, (2) blue 505 nm LED, (3, 5) beam splitters, (4, 9) lenses, (6) microscope objective, (7) sample holder, (8) white light illumination and (10) color camera. Dashed boxes represent the *InfiniTube<sup>TM</sup> FM-200 System*.

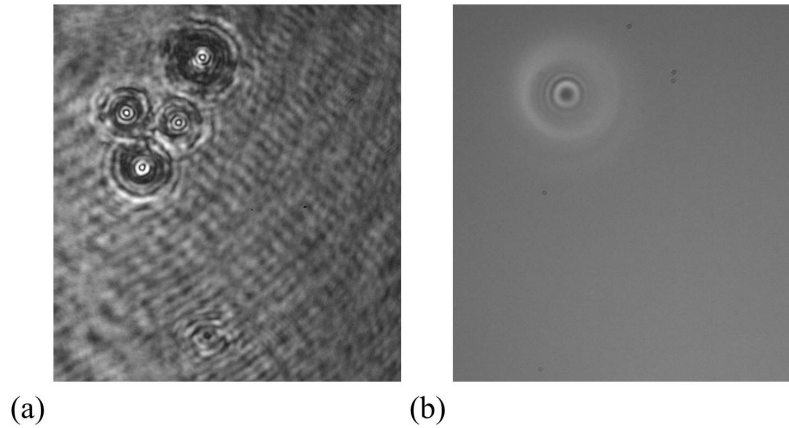


Figure 2.4: Comparison between an image taken using a low-coherent laser (*CrystalLaser*<sup>®</sup> Stabilized Compact Red laser,  $l_c < 300 \mu\text{m}$ ) (a) and a similar image using instead the red LED light (b).

Inside the imaging tube the bi-chromatic beam is reflected by a second beam splitter (5) towards the 100X objective<sup>5</sup> (6), which focuses the light on the sample (7). The objective has been chosen for its long working distance and high numerical aperture. The working distance is enough to penetrate at least  $100 \mu\text{m}$  in the liquid above the interface in order to have the possibility to follow particles also in the bulk. On the other hand an high numerical aperture allows instead the collection of a large solid angle of rays thus improving the quality and the number of the interference fringes.

In fig. 2.3(b) the imaging part of the setup is highlighted. The sample (7) is held on a stage equipped with a  $xy$  micrometric translator and a focusing knob ( $z$  direction). The focus can also be finely adjusted using a piezo objective scanner (*MCL*<sup>®</sup> Nano-F100) driven by a custom LabView controller program. The full displacement range of the piezoelectric actuator is  $100 \mu\text{m}$  with individual steps of  $0.2 \text{ nm}$ . The 100X objective and a second lens (9) at the end of the tube create a 2-lenses magnification system. After the lens, a color camera<sup>6</sup> (10) is mounted to collect the signal.

An RGB camera is used in order to simultaneously and separately record the two wavelengths' interference patterns. The spectral responses of the red and blue channels of the camera sensor (black lines in fig. 2.5) are sufficiently separated to avoid the superimposition of the power spectra of the two color sources (grey lines in fig.2.5), which allows the recording of the intensity of the blue diode on one channel and the red one on another.

In order to know the magnification of the system the effective pixel size is measured. The real size of the pixel is  $3.75 \mu\text{m} \times 3.75 \mu\text{m}$ , while its effective size is obtained measuring a graduated ruler (100 lines per mm) on the microscope. From the calibration an effective pixel size of  $0.0490 \pm 0.0004 \mu\text{m}$  is found, corresponding to an overall magnification of 76.5.

<sup>5</sup>100X *Mitutoyo* Plan Apo Infinity Corrected Long WD Objective,  $N_A = 0.7$ , Focal Length = 2.0 mm, Working Distance 6 mm, Depth of Focus =  $0.6 \mu\text{m}$ .

<sup>6</sup>*Basler dart camera daA1280-54uc* equipped with a CMOS sensor.

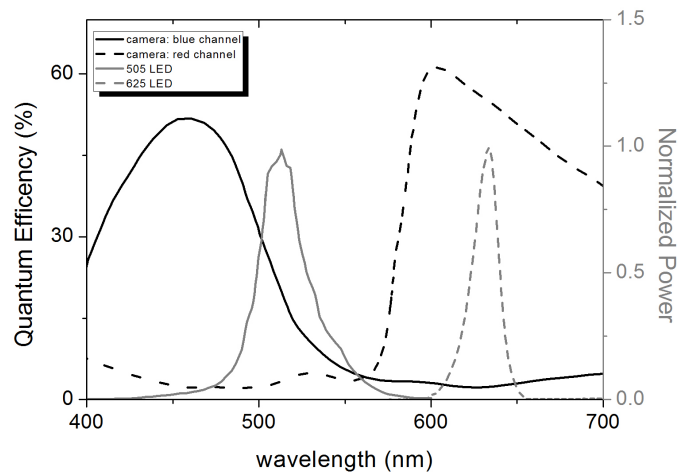


Figure 2.5: Spectral response of the blue and red channels of the color camera (black solid and dashed line respectively) and power spectra of the two blue and red monochromatic LED (grey solid and dashed line respectively). Data provided by camera's sensor and LEDs datasheets).

### 2.1.3 Fringe formation

The DW-RIM technique used in this thesis is a simplified version of the Reflection Interference Contrast Microscopy (RICM) technique, often used to image objects in contact with glass [104]. Such technique is usually employed with cell membranes or other biological objects<sup>7</sup>. The interference pattern formation is very similar when replacing the glass-water interface with the air-water one. The technique we used here shares therefore the properties and limitations of RICM.

The used DW-RIM technique works in an imaging configuration. The fringes, arising from the phase shift between the two reflected light beams, are formed only over the area of the colloid. We will assume as in RICM that they are localized on the water-air interface.

Figure 2.6 sketches the optics of the experiment. Let's define  $z_s(x, y)$  as the distance between one point  $P1$  on particle's surface and the interface as a function of the  $xy$  position with respect to the particle center (see the inset of fig. 2.6). The interference pattern is due to the phase shift between parallel rays reflecting at the water air interface and rays reflecting at the particle surface. This corresponds to an optical path difference of about  $2n_1z_s$ .

In figure 2.6 the sketch of the image formation is represented both for the colloid (in black) and for the air-liquid interface (in red). Since the Rayleigh length<sup>8</sup> is larger than the distance between the particle and the interface, both points  $P1$  and its projection  $P2$  on the interface are focused for the same position of the objective. This assumption is correct if we are imaging an object while it holds only as a first approximation in the case of interferometry. Strictly speaking, for interferometry the fact of considering the whole Rayleigh range as focused is not correct because of

<sup>7</sup>Since biological objects have a small index contrast with water, in RICM polarization effects are used to eliminate reflections in the objective and improve the contrast. In the present work this is unnecessary because the contrast is already good enough, as it will be detailed in section 3.1.

<sup>8</sup>For the definition of the Rayleigh length, see appendix A.

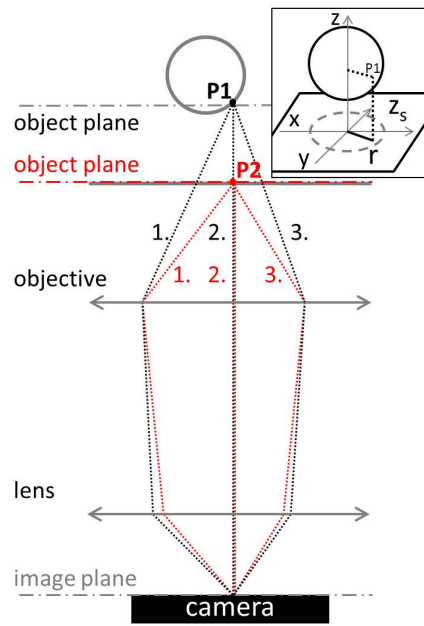


Figure 2.6: Sketch of image formation for the particle (black) and for the air-liquid interface (red). In the inset the coordinates of the point  $P1$  on the particle's surface are represented.

its sensitivity to the differences in optical path higher than the one of the imaging. Nevertheless, here the fringe formation is described supposing valid the aforesaid approximation and the errors this assumption introduces are discussed in section 2.2.2.

Note that colloid and air-water interface reflections both add a phase shift of  $\pi$  because the rays impinge on these interfaces from the medium having the lower refractive index:  $n_2 < n_1$  and  $n_1 < n_{coll}$ , marking with 1 and 2 the liquid and air respectively. Such contribution is therefore irrelevant. The same happens replacing water with all the water-based solutions used in the present work.

The fringes are assumed to be localized on a surface very close to the air-water interface and the focus is set on this plane. Image formation on the camera implies that all the rays propagating in all directions starting from a given point of the object (e.g. the paths 1., 2. and 3. in fig.2.6 for  $P1$  or  $P2$ ) will focus on a single point in the image plane of the camera after having travelled the same optical distance: the paths' lengths are different (2. is shorter than 1. and 3.) but the optical path is the same for all the rays coming from the same point.

For both  $P1$  and  $P2$  we can therefore consider only path 2. The optical path difference between the two beams is therefore  $2n_1 z_s(x, y)$ .

The bottom-right corner of figure 2.7 shows an example of the obtained interference pattern for a spherical particle, with its typical concentric rings. The coloured halo effect surrounding the colloid is not due to interference but to a combination of reflection and refraction inside the sphere. Dispersion relations for the refractive index implies that deflections are different for red and blue, generating spatial separation as in rainbows. This is confirmed by the order of the wavelengths in the halo, with blue inside and red outside.

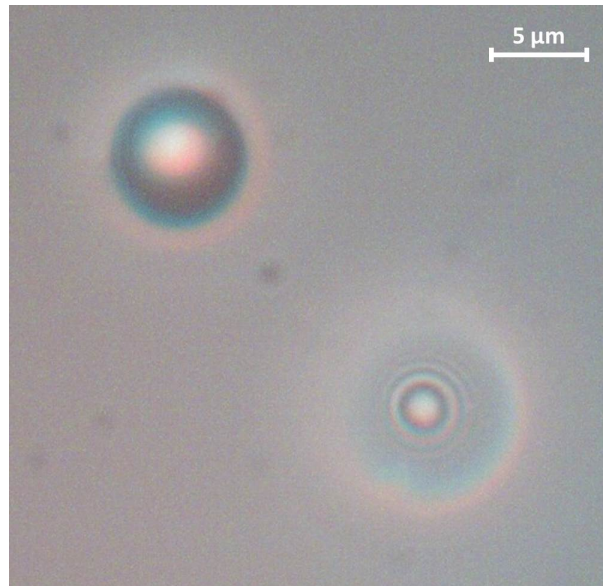


Figure 2.7: Typical interferometric image obtained from our experimental setup. In the top-left corner it is possible to see an image of a ( $8.9 \mu\text{m}$  diameter) spherical particle trapped at the interface with no associated interference pattern. The spherical particle in the bottom-right is close to the interface; interference fringes can be therefore observed.

Note that the described detection method allows an immediate discrimination between particles close and trapped at the interface: the particle in top-left of figure 2.7 do not show any interference pattern thus implying the absence of a liquid film between the particle and the objective, preventing double reflection. That particle is trapped at the interface.

#### 2.1.4 Optical alignment of the setup

A uniform illumination of the particle is required to efficiently track the interference pattern. Figure 2.8(a) shows how the interference pattern for a spherical particle appears if no attention is paid to the alignment between the illumination beam, the normal to the air-liquid interface and the axis of the objective screwed on the imaging tube. An azimuthal asymmetry of the interference intensity is visible. Misalignment affects illumination since if the reflected cone of light is tilted compared to the objective axis, more signal is collected from the particle's side towards which the incident cone of light is tilted.

The optical path between the objective and the camera has no degrees of freedom since all components are screwed on the imaging tube described in 2.1.2. The alignment between the objective and the sample's stage is made with a bullseye level by insuring that they are mounted perpendicularly. In the case of a flat interface the normal to the liquid surface is therefore parallel to the optical axis of the imaging part of the setup. Nevertheless, as explained in section 3.2.3 during experiments the surface is always convex. For this reason the asymmetry of figure 2.8(b) cannot be completely removed. For curvatures of the order of the ones used in the experiments (section 3.2.3) the light deflection coming from the tilt between the optical axis and

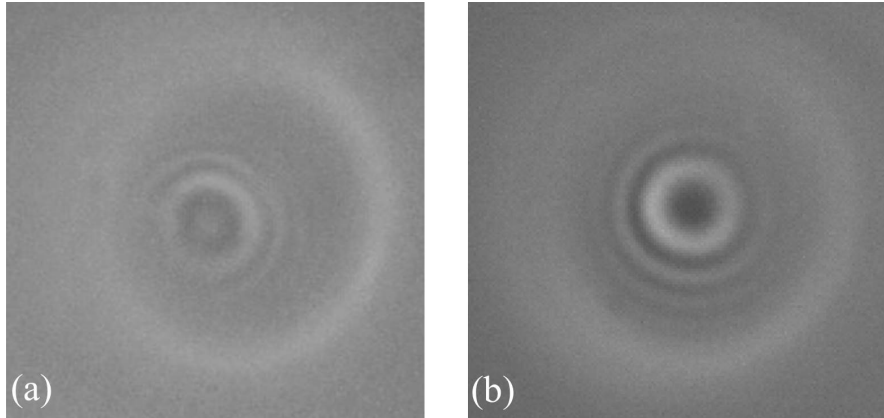


Figure 2.8: Two examples of interference patterns due to a spherical particle close to the interface. In the first image (a) it is possible to see the azimuthal asymmetry of fringes intensity due to the misalignment between the normal to the interface and the optical axis. In the second image (b) the system was aligned: it is still present a small asymmetry which is later removed by image treatment.

the normal to the interface negligibly affects the interference pattern for particles within a distance of 3 nm from the center of the curved interface.

Finally, the illumination beam has to be aligned with the imaging section of the setup. The focus is moved to image the light source on the camera. The illuminating beam's inclination can be removed centering the light source image in the camera field of view. This is possible moving the lateral lens (object 4 of fig.2.3(a)) equipped with micrometric translators.

Figure 2.8(b) shows a sphere's interference pattern after the setup alignment. A residual slight azimuthal asymmetry is still present and will be removed numerically as described in section 2.2.1.

## 2.2 Algorithms for the analysis

The two frame sequences of figure 2.9 illustrates the time evolution of the interference pattern for a sphere (a, b, c, d) and an ellipsoid (e, f, g, h). For each particle, four different frames are reported at different times. It can be noted that both the center (and for the ellipsoid also the orientation) and the phase of the interference pattern change due to the particle motion in the plane parallel to the interface and along the normal direction respectively. Such combined evolution of the fringes makes the particle tracking not trivial as will be detailed in section 2.2.1.

For the motion of a particle parallel to the interface a number of 2D tracking algorithms exist in order to extract the planar trajectory and the azimuthal angle. Usually the position of a particle in a frame is obtained looking for the light intensity's center of mass or by cross-correlation algorithms. In the first method the center of mass is found by a Gaussian fit of the image intensity. In the second, the image is spatially cross-correlated with a kernel having the same morphology of the object to track. The particle position is then extracted from the maximum of the correlation. The same methods also allow to recover the orientation of the particle in the plane.

In the present system none of the standard algorithms can be successfully em-

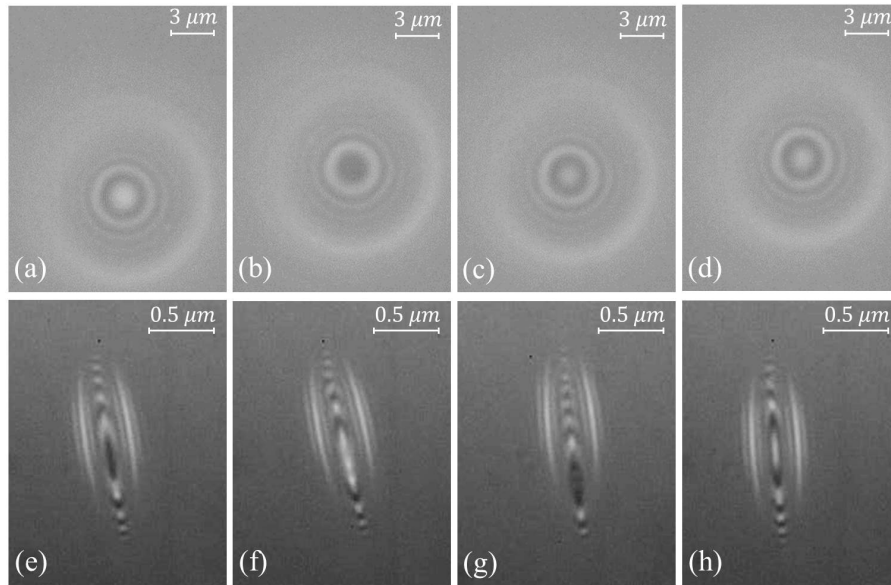


Figure 2.9: (a, b, c, d) Frame sequence of interference pattern of a  $4.5 \mu\text{m}$  spherical particle moving close to an air-water interface. (e, f, g, h) The same for an ellipsoidal particle with aspect ratio 10 and volume equivalent radius  $4.5 \mu\text{m}$ .

ployed because of two reasons. First, as shown in figure 2.9, the particle's interference pattern changes frame by frame, thus impeding the use of cross-correlation methods. Second the image is made of alternating fringes darker and brighter than the background. The center of mass methods therefore fail in determining the position of the object because on average the intensity is the same as the background. For these reasons dedicated tracking algorithms have been developed.

The analysis programs first track the center of the interference pattern in  $xy$  and extract the fringes' intensity profiles, radial for spheres and along the major axis for ellipsoids. The profiles are then analyzed to recover the distance from the interface and, for ellipsoids, the tilt angle.

Although the general lines of the tracking and reconstruction procedure are the same for both spheres and ellipsoids, adapted algorithms are necessary because of the differences between the two interference patterns. Dimensions of each single particle are obtained from bright field image in the case of spheres (sec. 2.2.1) and directly from the interference pattern for the ellipsoids (sec. 2.2.4).

### 2.2.1 Algorithms for spherical particles

#### Measurement of the sphere's radius

The spherical particles used in this work are made of Polystyrene and have a size dispersion of 2% for carboxylated and of 10% for sulfate functionalized particles (see section 3.1). This uncertainty is not sufficient for a significant comparison of single sphere's experimental results and models. A precise in-situ measurement was then required. On the other hand the sample polydispersity was an advantage since it allowed us to explore easily a possible size dependency of the dynamics. The radius can be measured from sphere's bright field image focusing on its equatorial plane.

Here, the procedure for this measurement is described together with the reached precision.

Prior to recording the particle interference patterns, we record its bright field image. In order to find the particle's equatorial plane, we approach the objective to the sample recording the particle image at each objective position. The  $z$ -scan can be done neglecting the contemporary particle's displacement in  $z$  as this last one is of the order of few tens of nanometers, remaining much lower than the scan step of 250 nm.

In figure 2.10(a, b, c, d, e) five snapshots obtained at different focal planes are reported<sup>9</sup>; while in fig.2.10(f), the azimuthal average of the light intensity versus the distance from the particle's center is given. The azimuthal average is obtained by selecting on the frame an annulus containing the bright perimeter. The annulus is chosen in order to keep its inner and outer perimeter tangential respectively to the inner and outer perimeter of the bright halo which defines the border of the sphere. Then, the algorithm does an azimuthal average over intensity profiles of the image taken along all straight lines passing from the center of the selected annulus.

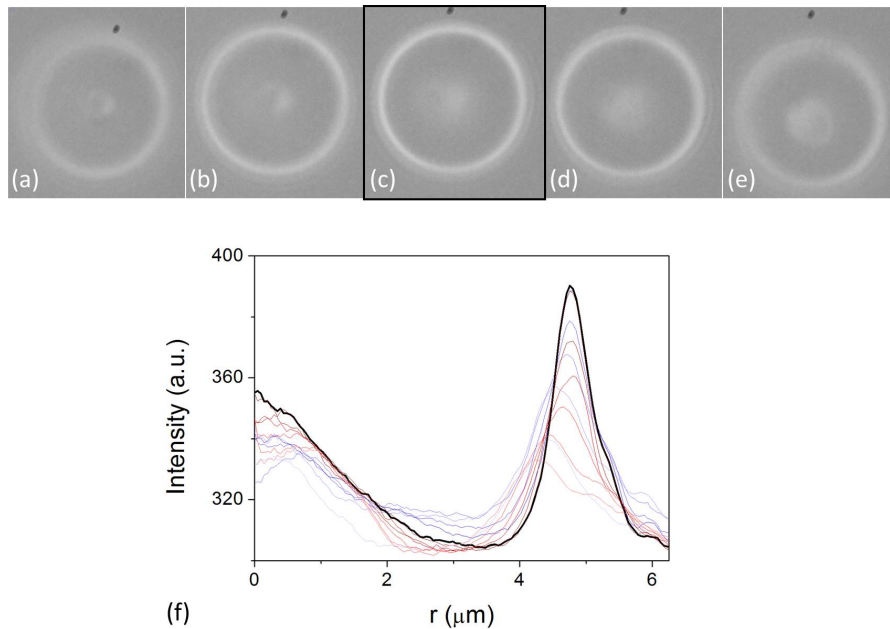


**Figure 2.10:** Five bright field image snapshots (a, b, c, d, e) of the same carboxylated spherical particle scanned by the piezo along  $z$ . In (f) the averaged intensity profile for different values of  $z$  are reported as a function of the distance  $r$  from the center. Black thickest line identifies the profile with the best resolved annulus perimeter. Blue and red lines identifies profiles for  $z$  lower and higher than the black one respectively. The step in  $z$  between each reported profile is of 500 nm, for a total scan covering 5  $\mu\text{m}$ . Black thicker profile in (f) corresponds to snapshot (c).

Among the different intensity profiles we choose the one with the more resolved annulus (black thicker profile in 2.10(f)). This is the profile for which we consider focused the particle's equatorial plane. The corresponding distance from the center

<sup>9</sup>On the figure, fringes are not present because interface is not any more within objective's Rayleigh length.

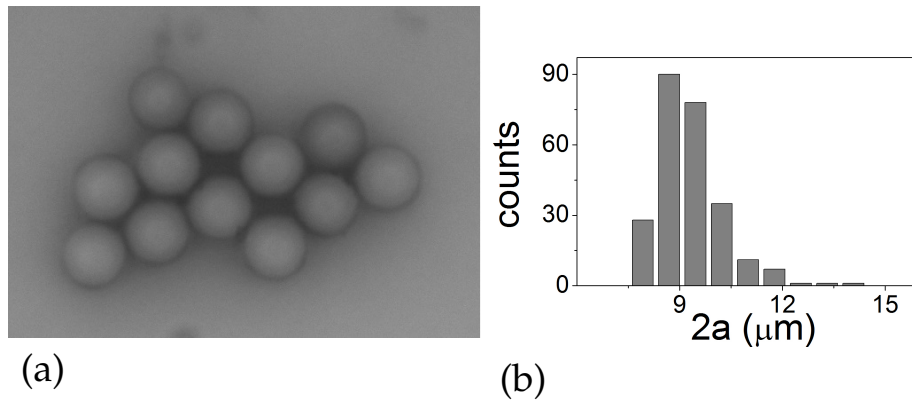


**Figure 2.11:** (a) Bright field image of a cluster of sulfate polystyrene spheres dried on a silicon wafer. (b) Size distribution of 250 measured sulfate polystyrene particles, with mean value  $9 \mu\text{m}$  with standard deviation  $1 \mu\text{m}$ .

of the intensity maximum is the measured radius  $a$  of the particle.

The error on the radius  $\sigma_a$  comes from the width of the annulus and from the different values found for red and blue channels. It depends from the observed particle and varies between  $20 \text{ nm}$  and  $70 \text{ nm}$ .

The radius of about 300 spheres among the two employed sets have been measured and the obtained distributions have been compared with the nominal ones. The result for carboxylated latex beads is a mean diameter of  $9.28 \mu\text{m}$  with a standard deviation of  $0.05 \mu\text{m}$ . This value is about  $0.4 \mu\text{m}$  larger than the manufacturer's nominal mean value:  $8.9 \pm 0.1 \mu\text{m}$ . The ratio between the nominal and the measured value is equal to  $f = 8.9/9.28 = 0.96$ .

To further investigate such difference and to calibrate the measurement, we have measured the center to center distances of clustered spheres in contact in dried samples made of the same particles<sup>10</sup> (fig.2.11(a)). The value found with this method is  $8.8 \pm 0.1 \mu\text{m}$ , in agreement with the nominal one.

A similar discrepancy between the nominal value and the diameters measured from the annulus has been found also for sulfate spheres having a nominal diameter of  $8.7 \pm 0.9 \mu\text{m}$  (see section 3.1). The diameter measured for 250 different particles (figure 2.11(b)) has an average value of  $9 \pm 1 \mu\text{m}$ .

The same  $f$  found for the carboxylated and sulfate spheres is also found for  $6.2 \pm 0.4 \mu\text{m}$  polystyrene beads<sup>11</sup>. Hence, the discrepancy between these values may be connected to the assumption that the maximum of light intensity in fig. 2.10(f) corresponds exactly with the particle border. It appears therefore that the radius found with this method is overestimated and a correction by the factor  $f = 0.96$  is thus applied to all the measured radii.

### Spherical particle center of mass tracking program

The tracking program finds the center of the interference pattern for each image and extracts the intensity profile of the fringes.

In order to treat each frame in an automatic way, the residual azimuthal asymmetry in intensity (see figure 2.12(a)) needs to be further reduced by the software. The program does a first-order correction finding the plane passing from the ridge of the

<sup>10</sup>During drying the strong attractive capillary force pushes particles in contact with each other.

<sup>11</sup>MolecularProbes™ carboxylated latex beads, 4% w/v,  $6 \mu\text{m}$ .

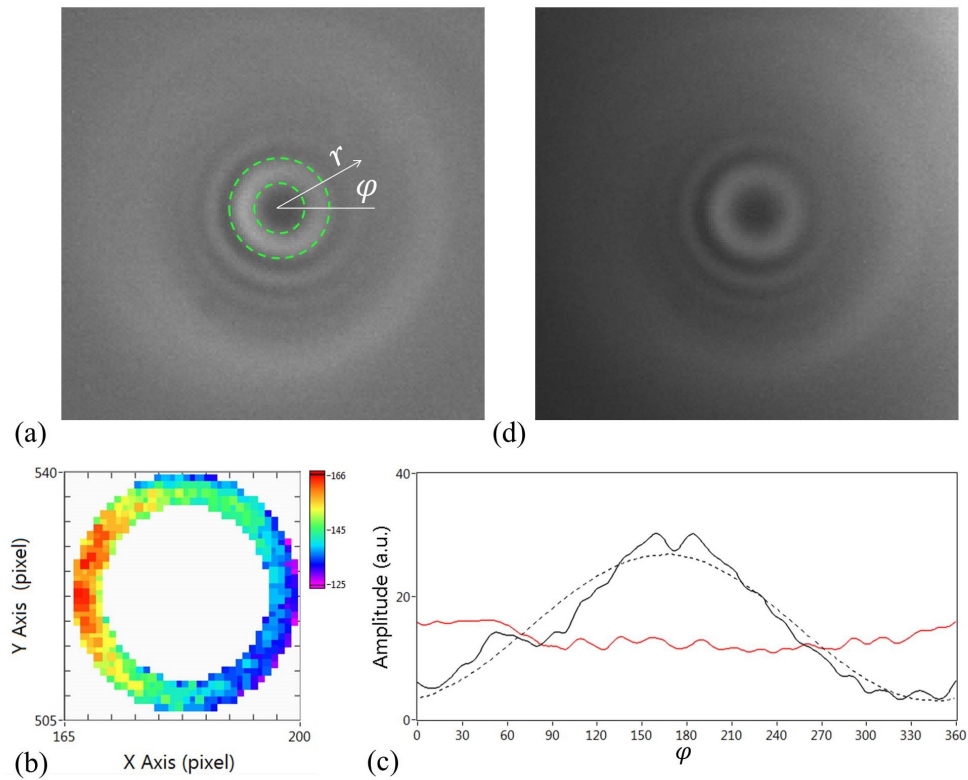


**Figure 2.12:** Example of the software correction of the asymmetry in the light intensity. (a) The procedure starts from the raw frame selecting an annulus containing the first fringe (dashed green annulus). In (b) the intensity inside the selected annulus is reported in false colours to stress the inequality of the ridge's height. In (c) the radial average of (b) (black continuous line) and its fit with a tilted plane (black dashed line) are plotted as a function of the azimuthal angle. Also represented in (c) is the corrected intensity (red continuous line) recovered from the resulting image (d) obtained by the ratio between (a) and the fitted plane.

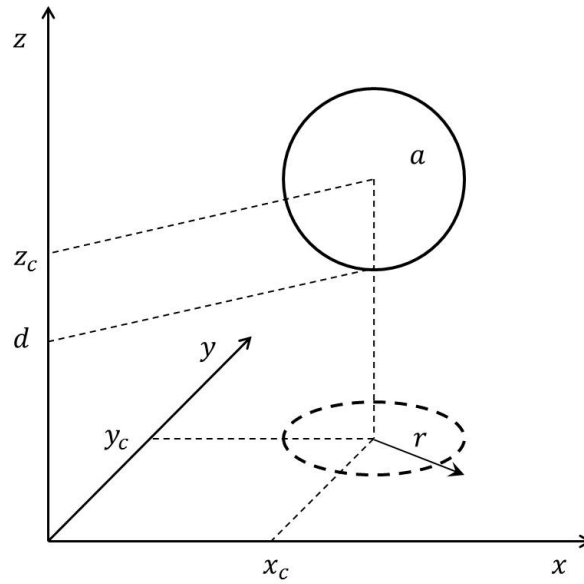


**Figure 2.13:** Sketch of the reference system for the sphere and the tracked degrees of freedom. The interface is at  $z = 0$ ,  $(x_c, y_c)$  are the particle center's coordinates in the plane of the interface and  $z_c$  is its coordinate along the normal to the plane. The distance  $d$  between the particle's surface and the interface is equal to  $d = z_c - a$ .

first fringe. Noting  $I_m(x, y)$  the measured intensity of the image as a function of the planar coordinates  $x$  and  $y$ , and  $I(x, y)$  the expected symmetric one, the relation between them is

$$I_m(x, y) = A_s(x, y) I(x, y), \quad (2.2)$$

where  $A_s$  is an illumination function which weighs the signal of each pixel. The illumination function can be written in a polynomial expansion as

$$A_s(x, y) = c_0 + c_{x,1}x + c_{y,1}y + \mathcal{O}(x^2, y^2, xy) \quad (2.3)$$

Here, only the linear terms are taken into account<sup>12</sup>.

The three coefficients  $c_0$ ,  $c_{x,1}$  and  $c_{y,1}$  are found by selecting on the first frame an annulus containing the first maximum of interference (2.12(a)). In 2.12(b) the selected region is reported in false colours to highlight the inequality of the ridge's height. Over this annulus a radial average of the intensity is made for each azimuthal angle  $\varphi$  to reduce the noise. In this way a function  $I_m(x, y)$  defined on a circumference with radius equal to the mean radius of the annulus is found.

The function  $I_m(x, y)$  is then fitted with the plane  $c_0 + c_{x,1}x + c_{y,1}y$ . In fig.2.12(c)  $I_m(x, y)$  (black continuous line) and the fitting plane (black dashed line) are shown versus the azimuthal angle  $\varphi$ . Once  $c_0$ ,  $c_{x,1}$  and  $c_{y,1}$  are found the corrected image (fig.2.12(d)) is found from the ratio between the original image 2.12(a) and the function  $c_0 + c_{x,1}x + c_{y,1}y$ . Such correction with the first frame fitting plane is then applied to all frames of the video.

<sup>12</sup>We chose to stop at the first order since we saw that this correction is enough to improve the efficiency of the tracking, making the algorithm working.

Once this correction is made the program starts the particle tracking. On the first frame the approximate position of the center of the fringes is chosen as initial condition for the tracking. A region of interest (ROI) containing the particle is also selected. For any new frame a new ROI is taken with same dimensions of the first one but centered on the previous frame's particle coordinates.

During the present work different methods to track the center of the interference pattern have been tested, weighing up their efficiency and velocity. Two main attempts have been made on frames binarized imposing a threshold higher than the average intensity in order to remove the background and the interference minima. The center of the fringe system was then recovered either as the center of mass of the binarized frame (first method) or identifying the circumferences corresponding to the fringe's maxima and taking the average of their centers as the particle's coordinates (second method). In Appendix B the main attempts are resumed. These attempts failed as binarization is a valid option only with objects wholly brighter or darker than the background, easily identified with a threshold, while here the object is an interference pattern with a lot of maxima and minima and all the shades of gray between them.

A third attempt was made working on the original frame finding all the intensity extrema (maxima and minima) and selecting the one closer to the previous' frame's center. In this way, the particle's coordinates are identified as the central zero-order intensity extremum of the interference pattern. This method has proved to be uneficent because of noise which prevents an easy identification of the extrema.

We finally implemented a method, which proved to be more efficient and robust, consisting in a direct fit of the image. The intensity of the frame  $I(x, y)$  inside the ROI is fitted with the 3D interference function coming from the superimposition of the two reflected beams.

The derivation of the formula for the interference pattern is given in Appendix A and the result is:

$$I(x, y) = 2I_0 \left[ 1 + \cos \frac{4\pi n_1}{\lambda} \left( d + a - a\sqrt{1 - \frac{r^2}{a^2}} \right) \right], \quad (2.4)$$

where  $r = \sqrt{(x - x_c)^2 + (y - y_c)^2}$ , being  $(x_c, y_c, z_c)$  the coordinates of the center of the particle (see figure 2.13),  $d$  is the particle-interface minimal distance (equal to  $z_c - a$ ) and  $\lambda$  is the wavelength of the red ( $\lambda_R$ ) or blue ( $\lambda_B$ ) LED.

The expression 2.4 predicts same amplitude for all the maxima. Conversely, in the measurements the intensity decreases increasing  $r$  (see fig. 2.12(a) and (d)). This is mainly due to the finite collecting angle of the objective, which alters the fringe system in a way described in detail in section 2.2.2.

We take into account this additional effect modulating the function 2.4 with a Gaussian function  $e^{-\frac{r^2}{2\sigma^2}}$ , which proved to be effective in making the fit converge recovering the correct  $x_c$  and  $y_c$ .

The used fitting function is therefore:

$$I(x, y) = Ae^{-\frac{r^2}{2\sigma^2}} \left[ 1 + \cos \frac{4\pi n_1}{\lambda} \left( z_c - a\sqrt{1 - \frac{r^2}{a^2}} \right) \right] + B \quad (2.5)$$

The fitting parameters are the multiplicative factor  $A$ , the offset  $B$  and the coordinates of the center of the sphere  $x_c$ ,  $y_c$  and  $z_c$ . After some tests on different recorded

trajectories we found that  $\sigma$  can be kept fixed at  $0.588 \mu\text{m}$  for all the particles, as expected since the object is always the same and the particle size only slightly changes.

In 2.14 an example of the result of the fitting procedure is reported: the minima and maxima of the fitting function (represented by blue and red circles) have been superposed to the original pattern, showing a good agreement.

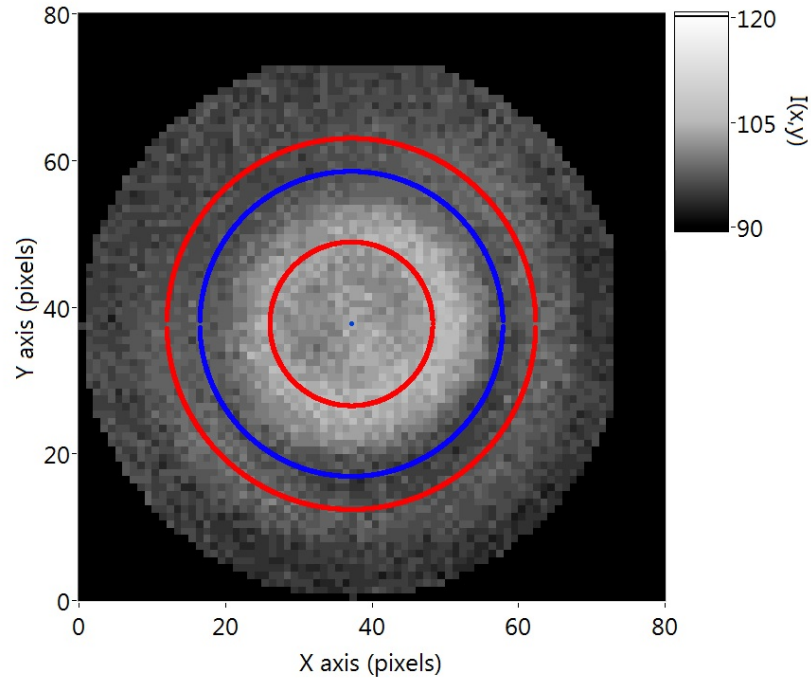


**Figure 2.14:** Example of the result of the fit method to find the center of the sphere. The non-zero points are the data considered for the fit. On the original data are superposed the circumferences corresponding to the minima (blue lines) and the maxima (red lines) of the fitting function evaluated for the best fitting parameters.

The error done in extrapolating  $x_c$  and  $y_c$  has been evaluated simulating a set of interference patterns of a same particle and different  $(x_c, y_c, z_c)$  and letting them be analyzed by the tracking program. From the comparison of the tracked centers with the correct ones a standard deviation  $\sigma_x = \sigma_y = 0.05 \mu\text{m}$  associated to  $x_c$  and  $y_c$  has been estimated.

The value of  $z_c$  given by the fit with equation 2.5 strongly depends on the radial position of the intensity extrema. This position is affected by the modulating arbitrary Gaussian function used to enable the fit to converge. For this reason the obtained  $z_c$  is not reliable and a further analysis of the radial intensity profile is required (sec.2.2.1). The determination of  $x_c$  and  $y_c$  is not affected by this problem since a radial function modulation doesn't affect its polar symmetry.

Once the analysis on the first frame is made, a loop over the entire video begins, where at each cycle the given input are the previous frame's parameters (the center coordinates  $x_c$  and  $y_c$ ). The new parameters are given in output in a *.txt* file together with the intensity profile of the fringe system. The profile is made by an azimuthal average of the intensities.

### Spherical particle fringe analysis: measurement of the gap distance $d$

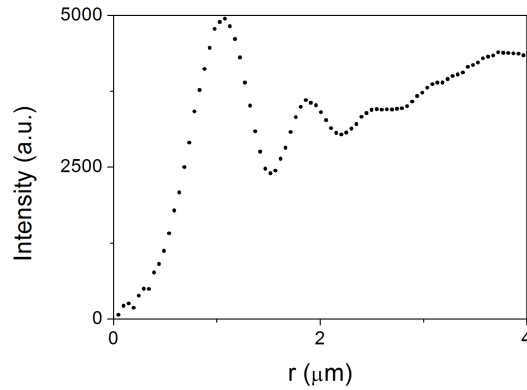


**Figure 2.15:** Typical example of an  $\varphi$ -averaged intensity profile versus  $r$  for a  $4.5 \mu\text{m}$  radius sphere.

In figure 2.15 a typical output of the sphere's tracking algorithm is reported. It is the plot of the  $\varphi$ -averaged intensity profile versus the radial coordinate  $r$ .

In order to obtain the particle-interface distance  $d$  the radial positions of the intensity maxima ( $r_M$ ) and minima ( $r_m$ ) are measured. To enhance the resolution the program takes the relative extrema of  $I(r)$  and for each one fits their neighbouring points with a parabola. The number of fitting points varies from 3 to 6 depending on the noise present on  $I(r)$ . The centers of the fitted parabolas are taken as the positions of the extrema. In this way the precision in the determination of  $r_M$  and  $r_m$  reaches a resolution  $\sigma_{par} \simeq 10 \text{ nm}$ .

The distance  $d$  is found following frame by frame the radial position  $r_e$  of an extremum. The distance  $d$  is directly found imposing in 2.4 the condition for the formation of an interference maximum or minimum. The resulting  $d$  are respectively:

$$d = a \left( 1 - \sqrt{1 - \left( \frac{r_M}{a} \right)^2} \right) + m \frac{\lambda}{2n_1} \quad (2.6)$$

and

$$d = a \left( 1 - \sqrt{1 - \left( \frac{r_m}{a} \right)^2} \right) + \left( m + \frac{1}{2} \right) \frac{\lambda}{2n_1}, \quad (2.7)$$

where  $m$  is a natural number representing the number of half-wavelengths contained in the distance between the particle and the interface. From the relations 2.6 and 2.7  $d$  can be known up to the additive factor  $m \frac{\lambda}{2n_1}$ .

The value of  $m$  is found cross-checking the information coming from the two wavelengths of the setup. For a given particle, the tracking is made both on the red and blue channel of the video recording. For each wavelength, the trajectory is reconstructed and plotted on the same graph as a function of the frame number and for different values of  $m_R$  (for the red) and  $m_B$  (for the blue) in order to find the couple for which there is the best agreement. In figure 2.16 an example of reconstructed

trajectories are plotted for the two channels and for three values of  $m_R$  and  $m_B$ : the best agreement is here obtained for  $m_R = m_B = 1$ .

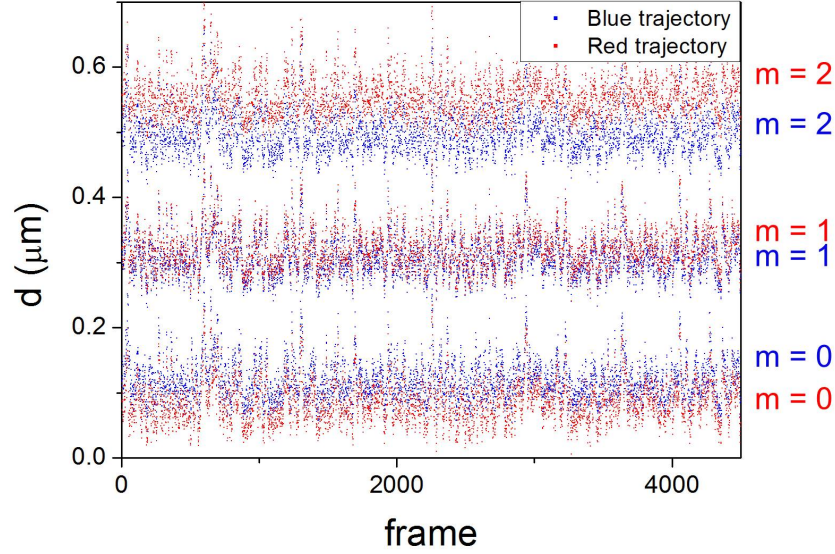


**Figure 2.16:** Comparison between the reconstructed time evolution of  $d$  coming from the red and the blue channels of the camera and for different  $m_R$  and  $m_B$ . The absolute averaged difference between red and blue channels for different combinations of  $m$  are: 32 nm ( $m_R = m_B = 0$ ), 13 nm ( $m_R = m_B = 1$ ), 57 nm ( $m_R = m_B = 2$ ) and higher values for  $m_R \neq m_B$ . In this example the best agreement is therefore for  $m_R = m_B = 1$ , giving an absolute average distance from the interface of  $\langle d \rangle = 0.311 \mu\text{m}$ .

Operatively the best couple of  $m_R$  and  $m_B$  is found minimizing the absolute averaged difference between the trajectories reconstructed from the two channels, *i.e.*  $|\langle d_R - d_B \rangle_t|$ . The possible values of  $m$  which are considered for the comparison range from 0 to 10. For higher orders the distance between the particle and the interface would indeed be larger than the coherence length.

### 2.2.2 Resolution in the gap distance measurement

Concerning the uncertainty  $\sigma_d$  on the measure of  $d$ , it derives from the propagation of the errors on the radius,  $\sigma_a$ , and on the position of the extremum,  $\sigma_{r_e}$ :

$$\sigma_d = \sqrt{\left(\frac{\partial d}{\partial r_e} \sigma_{r_e}\right)^2 + \left(\frac{\partial d}{\partial a} \sigma_a\right)^2} = \sqrt{\frac{r_e^2 \sigma_{r_e}^2}{a^2 - r_e^2} + \left(\frac{a}{\sqrt{a^2 - r_e^2}} - 1\right)^2 \sigma_a^2} \quad (2.8)$$

The error on the radius, given in section 2.2.1, depends on the particle and varies between 20 nm and 70 nm. The error on the position of the extremum  $\sigma_{r_e}$  is instead given by the sum of three sources:

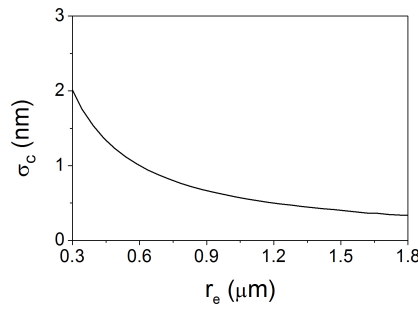


Figure 2.17: Error on  $r_e$  related to the precision in the measurement of the center of the interference pattern as a function of  $r_e$  given by the off-center azimuthal average.

$$\sigma_{r_e} = \sigma_{par} + \sigma_c + \sigma_{NI} \quad (2.9)$$

The first term is the incertitude coming from the precision in the determination of  $r_e$  with the parabolic fit described in 2.2.1 and results in  $\sigma_{par} = 10$  nm.

The second term  $\sigma_c$  is the error related to the precision in the measurement of the center of the interference pattern. When the radial intensity profile is recovered from the azimuthal average of the profiles passing from the center (section 2.2.1), an error in the center determination carries a distortion of the averaged intensity profile. The evaluation of  $\sigma_c$  has been made computing from eq. 2.4 the  $\varphi$ -averaged intensity profile centered on a new point located at a distance  $\delta_{xy}$  from the center of the fringe system. From this radial profile the coordinate  $\tilde{r}_e$  of an extremum is considered. Geometrical calculations (see appendix C) show that  $\tilde{r}_e$  is related to the extremum coordinate  $r_e$  corresponding to  $\delta_{xy} = 0$  by:

$$\tilde{r}_e = \frac{\delta_{xy}}{2\pi} \int_0^{2\pi} \sqrt{\frac{r_e^2}{\delta_{xy}^2} - \sin^2 \varphi} d\varphi \quad (2.10)$$

The value of  $\sigma_c = |r_e - \tilde{r}_e|$  evaluated for  $\delta_{xy} = \sigma_x = 0.049$   $\mu\text{m}$  is reported in 2.17(a) as a function of  $r_e$ . It can be seen that its contribution to the total error on  $r$  is negligible if compared to  $\sigma_{par}$ .

The third source of error  $\sigma_{NI}$  in equation 2.9 comes from the discrepancies between the experimental interference pattern and the model used to analyze the data, which consider only monochromatic beams at normal incidence. The calculation of the phase shift between the two reflected beams should consider the tilt of some rays relatively to the optical axis. The optical path difference, therefore, is not simply twice the normal distance between the surface of the particle and the interface [106]. The inclusion of the rays inclination affects the interference pattern. Since the illumination is focused on the sample, the incident rays form a cone of light whose angular amplitude depends on the numerical aperture  $N_A$  of the objective, but also on the way we have focused the light on the back focal plane of the objective (in our experiments we typically have an effective illumination numerical aperture of 0.45). In the computation of the interference pattern a first element that must be taken into account is therefore the incident cone of light and the additional optical paths travelled by rays not normally incident on the interface. Moreover, some rays impinging the sample can be back reflected with angles exceeding the cone of light collected by

the objective and their contribution to the interference pattern can be therefore lost. Finally, the particle surface is not planar and parallel to the interface and thus it also contributes to the deviation of the incident rays. A precise computation of all these phenomena is very difficult to make. It depends on the effective numerical aperture of the objective and on the precise optical properties of the involved interfaces, as the transmission and reflection coefficients are also function on the incident angle. For the particle, they depend on the precise optical properties and roughness of its surface. Because of such complexity, in the analysis we chose to consider only the normal incidence of a monochromatic light source. To evaluate the order of magnitude of the errors made under such assumption we made numerical calculations considering also the listed effect in order to compare them with the first-order model employed in the analysis. In figure 2.18 are reported numerical computations of the intensity of the interference pattern versus  $r$  for the red (a) and blue (b) sources. The patterns are calculated for a sphere of radius  $4.5 \mu\text{m}$  at a gap distance of  $300 \text{ nm}$  from the air-water interface. In each plot are represented: the interference pattern evaluated considering only normal incidence and the nominal wavelength of the source (black), the same evaluated considering the whole spectra of the source (blue), the interference pattern considering the oblique incidence and the whole spectra but considering the sphere made of a series of planes parallel to the air-water interface (red), and finally the same of the latter but also taking into account the curvature of the surface of the sphere (orange). It can be seen that the difference between the black and the blue simply results in a modulation in the height of the peaks, while the position of the maxima and minima does not change<sup>13</sup> (relative error on  $r_e$  lower than 1%). The red and the orange patterns are first characterized by a rapid decrease of the height of the peaks as a function of  $r$  which probably explains the observation of only a few experimental peaks. Moreover the positions of the peaks deviate in a more marked way from the black one, with relative errors over the three first extrema in the range between 2% and 10%. The deviation of  $r_e$  depends on the position of the extremum and on the gap distance  $d$ , is of the same order for both the wavelengths and can bring either a underestimation or an overestimation of the particle-interface distance.

Considering all the source of error on  $r_e$  and the one on the radius, the resulting error, evaluated with equation 2.8, on the particle-interface distance obtained from the analysis of one extremum is typically lower than  $20 \text{ nm}$ .

During the analysis we compare the experimental  $d$  time evolutions recovered for the same particle by analyzing 2-3 different extrema for each wavelength. The 4-6 obtained trajectories do not perfectly overlap because of the error  $\sigma_d$ . Their average  $d$  differ in a typical range of 2-15 nm, in agreement with the expected error. In the experimental results and for each particle, the experimental error is thus evaluated as the weighted standard deviation made over the 4-6 trajectories coming from the two channels.

### 2.2.3 Experimental validation of the analysis

An experimental test has been made in order to check the validity of the procedure to measure  $d$ . This test is made to secure that there are no neglected phase shifts, relevant aberration effects or an important superposition of the two wavelengths in the same channel of the camera. The test consists in the measurement of the size of two metallic spheres with a direct technique and from their interference patterns.

<sup>13</sup>A more exhaustive discussion on the negligibility of the contribution of the spectrum width of the light sources is discussed in appendix C.

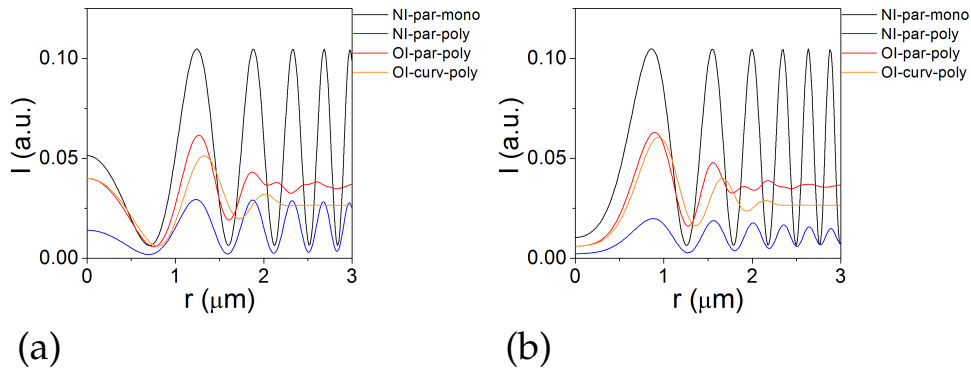


**Figure 2.18:** Numerical computed intensities of the interference pattern versus the radial coordinate  $r$  for a spherical particle of radius  $4.5 \mu\text{m}$  at a gap distance  $d$  from the air-water interface illuminated by the red (a) and by the blue (b) light source. Black line: interference pattern evaluated considering normal incidence on the interface, the nominal wavelength of the source and modelling the sphere surface as a series of steps parallel to the interface. Blue: interference pattern evaluated considering normal incidence on the interface, the whole spectra of the light source and modelling the sphere surface as a series of steps parallel to the interface. Red: interference pattern evaluated considering oblique incidence on the interface, the whole spectra of the light source and modelling the sphere surface as a series of steps parallel to the interface. Orange: interference pattern evaluated considering oblique incidence on the interface, the whole spectra of the light source and taking into account the curvature of the sphere surface.

The metal spheres are taken from the translator mechanism of a micrometric translator stage and have been chosen because of their exact dimensions. Their radii have been measured by a digital caliper and are respectively  $a_{M1} = 1189 \pm 1 \mu\text{m}$  and  $a_{M2} = 793 \pm 1 \mu\text{m}$ .

The metallic spheres have been placed on a microscope slide covered by a film of water, in order to keep at least the lower half of them in the liquid (figure 2.19). Interferometric images have been taken with both the LEDs. Figure 2.20 shows an image obtained using the red LED light. From the relative distance between each couple of adjacent intensity maximum-minimum the value of the radius has been extracted using relations recovered from the formulas reported in sec. 2.2.1. The obtained radii are  $a_{M1} = 1190 \pm 60 \mu\text{m}$  and  $a_{M2} = 800 \pm 30 \mu\text{m}$  in agreement with the values measured with the digital caliper<sup>14</sup>.

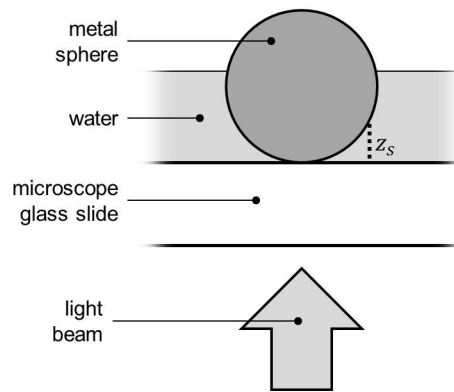


**Figure 2.19:** Experimental configuration used to measure the size of the metal spheres with the interference method.

## 2.2.4 Algorithms for ellipsoidal particles

The analysis of the ellipsoidal particles is divided in two steps: *i*) the particle tracking to find the major axis, its orientation  $\varphi_e$  and to extract the intensity profile along the major axis (see fig. 2.21(a) and (b)), and *ii*) the reconstruction program to recover from the intensity profile the center of mass coordinates, the tilt angle  $\theta_e$ , the moduli of the semiaxis and the gap distance  $d$  (see fig. 2.21(c)).

### Ellipsoidal particle tracking program

Figure 2.22(a) shows a typical interference pattern of an ellipsoidal particle. Dark and bright regions along the major axis of the pattern are the interference minima and maxima, while the two bright lateral wings are independent from  $d$  and are originated from internal reflection of incoherent light inside the ellipsoid.

During the present work, different methods to find ellipsoid's major axis from the interference pattern have been tested, weighing up their accuracy and efficiency.

<sup>14</sup>The errors here are larger than the ones on  $d$  for the  $9 \mu$  beads because the error on the radius is bigger than the one of  $d$  coming from the error propagation and because for this particular measure a different objective at lower magnification (50x) has been employed.

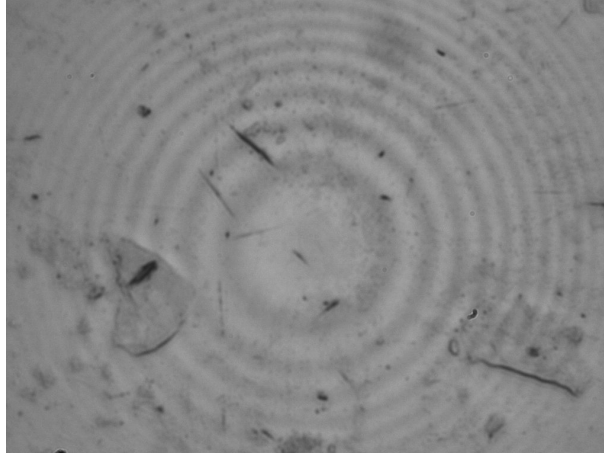


**Figure 2.20:** Fringe system originated by a metal sphere ( $a_{M1} = 1189 \pm 1 \mu\text{m}$ ) in the configuration of fig. 2.19. The employed wavelength is the red one.

The first attempt has been to look at the moments of the distribution of points in the binarized frame<sup>15</sup>. The first momentum returns the center of mass of the distribution, while the second one corresponds to the covariance matrix, whose eigenvectors and eigenvalues are the unit vectors and the moduli of the ellipsoid's semiaxes<sup>16</sup>. This method proved to be inefficient in recovering the major axis. The reason why it fails lies in the two lateral wings of the image of the ellipsoid. They are very bright compared to the interference fringes and thus a small difference in their brightness due to a small asymmetry in the illumination dramatically deviates the center of mass out of the real axes of the particle.

For this reason, the employed particle tracking program works on a different principle: it searches the two interference maxima that satisfies the following conditions: *i*) they are at a relative distance large compared to all the relative distances between all the interference maxima, and *ii*) they define a straight line passing as close as possible to the other maxima. The second condition has been included to avoid the risk of considering background dust grains or parts of the lateral wings as maxima (see figure 2.23).

Operatively, the ROI is binarized by applying a threshold equal to 1.5 times the average intensity inside the ROI. In the binarized image, more than 3 connected pixels are labelled as objects by the program. Then a selection is made of the couples of objects ( $N = 10$ ) with the largest relative distance. In order to satisfy condition *ii*) the program finally chooses among the selected  $N$  objects the couple  $(\alpha, \beta)$  which minimizes the sum  $D^{\alpha, \beta}$  of distances from the straight line defined by the couple (see fig. 2.23). In formulas  $D^{\alpha, \beta}$  is given by:

$$D^{\alpha, \beta} = \sum_{i=1}^N d_i^{\alpha, \beta} = \sum_{i=1}^N \left| \frac{y_i - px_i - q}{\sqrt{p^2 + 1}} \right|, \quad (2.11)$$

with  $p$  and  $q$  given by:

<sup>15</sup>Binarization is made imposing a threshold higher than the average intensity in order to remove the background and the fringes' minima, obtaining an image like the one in figure 2.22(b).

<sup>16</sup>If the tilt angle is zero.

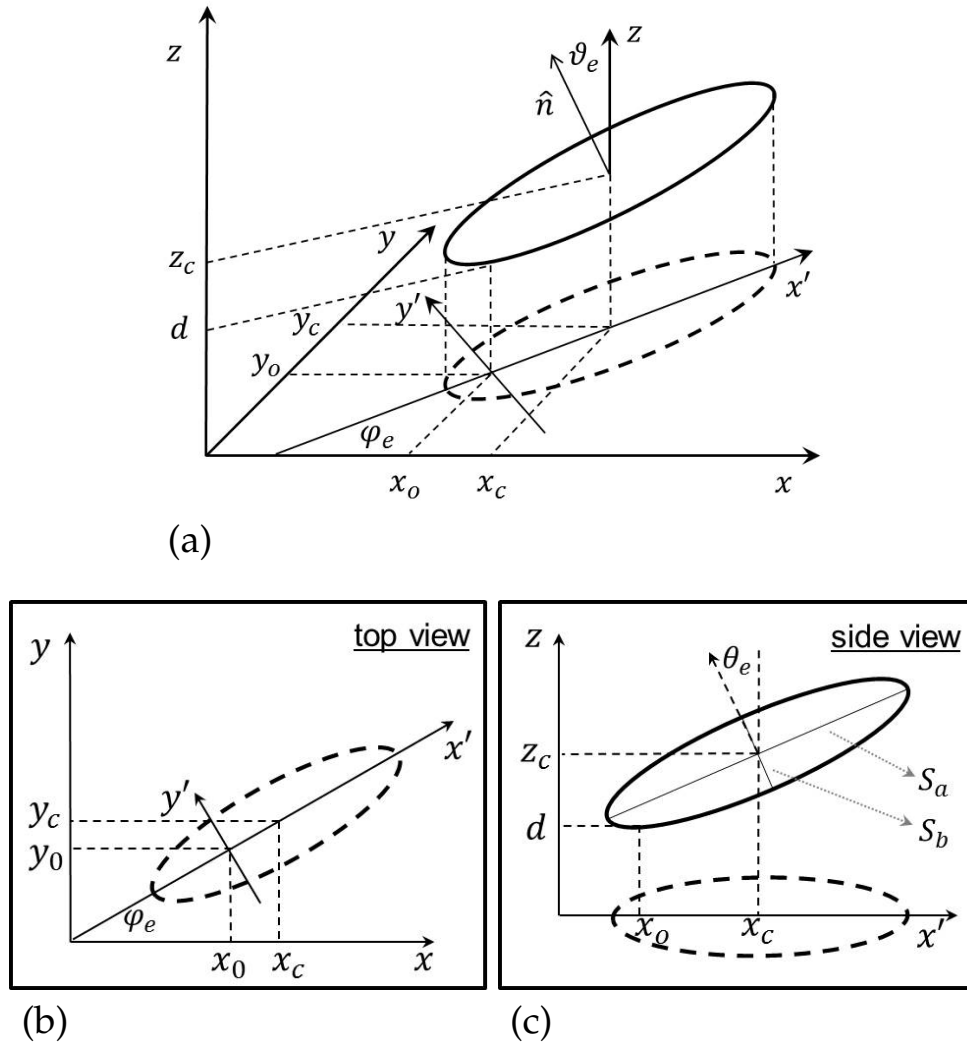


**Figure 2.21:** (a) Ellipsoid's reference systems and degrees of freedom. In (b) and (c) the top and the side view are also reported. The degrees of freedom found by the program are: the center coordinates  $(x_c, y_c, z_c)$ , the coordinates of the point of particle's surface closer to the interface  $(x_0, y_0, d)$ , the azimuthal angle  $\varphi_e$ , the tilt angle  $\theta_e$  and the moduli  $S_a$  and  $S_b$  of the major and minor semiaxis respectively. A local reference system is also defined. It is centered in  $(x_0, y_0, 0)$  and has the  $x'$  axis parallel to the major axis of the ellipsoid.

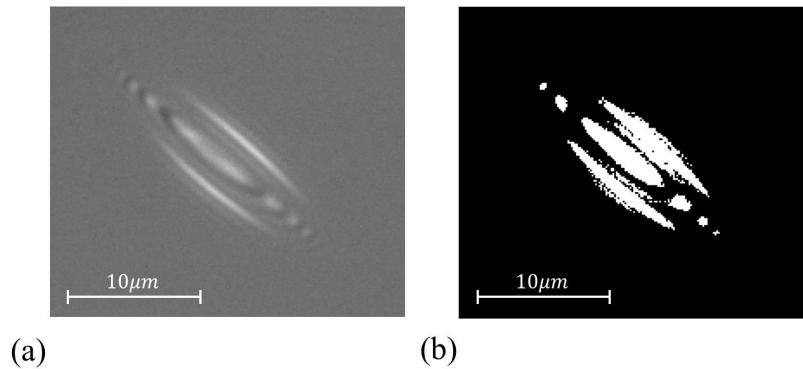


**Figure 2.22:** Typical interference pattern of an ellipsoidal particle of aspect ratio 6 (a) and its binarized version (b). In (b) the lateral wings are enhanced: they covers a surface comparable to the central maximum.

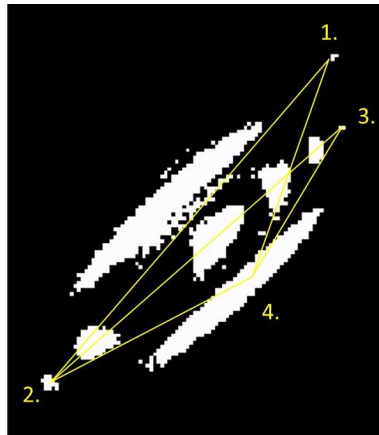


**Figure 2.23:** Binarized image of an ellipsoid close to a dust grain (object 1). Due to its vicinity to the ellipsoid the dust grain becomes one of the candidates to define the ellipsoid's major axis. Among the considered objects (here  $N=4$  instead of 10 for simplicity) the couple 1-2 is the one having the maximum relative distance. The additional criterium of passing as close as possible to the other maxima allows the automatic selection of the correct couple (2-3).

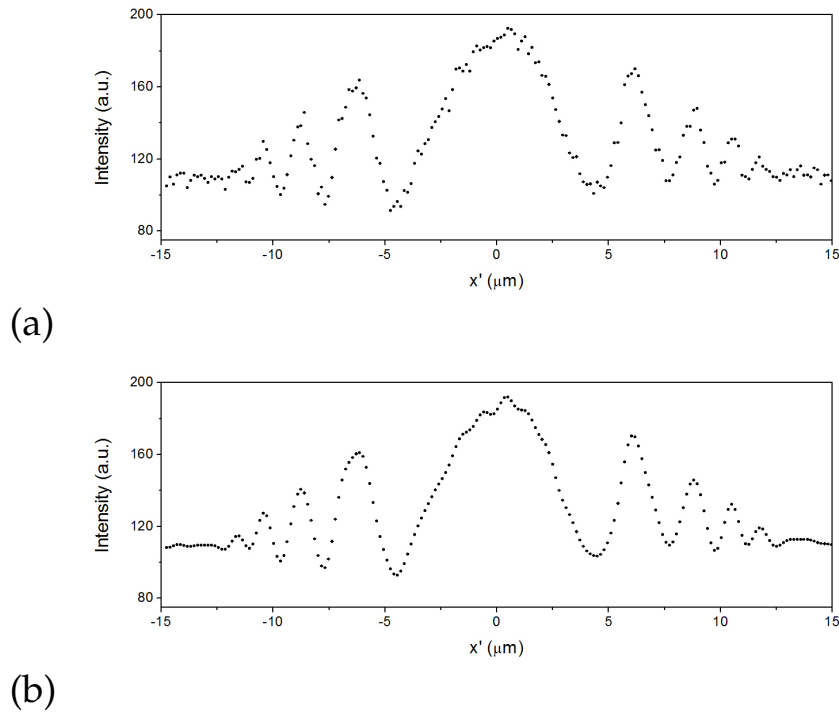


**Figure 2.24:** Typical measured intensity profile  $I(x')$  for an ellipsoid with an aspect ratio 6. (a) Raw data. (b) Data after the application of the low-pass filter.

$$p = \frac{y_\alpha - y_\beta}{x_\alpha - x_\beta} \quad (2.12)$$

$$q = y_\beta - mx_\beta \quad (2.13)$$

Here  $(x_\alpha, y_\alpha)$ ,  $(x_\beta, y_\beta)$  and  $(x_i, y_i)$  are respectively the coordinates of the center of mass of the two chosen objects ( $\alpha$  and  $\beta$ ) and of a generic one ( $i$ ).

The straight line connecting the couple  $\alpha$  and  $\beta$  which minimizes 2.11 is the major axis of the ellipsoid, along which the intensity profile of the fringe pattern is extracted. A local 2D cartesian coordinates system  $x'y'$  is also defined (fig. 2.21). The two axes  $x'$  and  $y'$  are parallel to the major and minor axes of the ellipsoid respectively, and the origin corresponds to the point  $(x_0, y_0)$  of minimal ellipsoid-interface distance. Operatively,  $(x_0, y_0)$  cannot be identified as the position of the central extremum of intensity, since the superimposition of the fringe system with the lateral bright wings around the center makes it unclear (see figure 2.24). The point  $(x_0, y_0)$  is therefore found along  $x'$  as the medium point between the first couple of intensity extrema on both side of the center of the intensity profile. Note that  $(x_0, y_0)$  is superimposed to  $(x_c, y_c)$  only for  $\theta_e = 0$  (see the side view of fig. 2.21).

### Ellipsoidal particle fringe analysis: reconstruction program

Figure 2.24(a) shows a typical intensity profile  $I(x')$  returned by the tracking program.

The first step of the algorithm is the removal of high spatial frequencies noise using a low-pass filter via the Fast Fourier Transform (FFT) of  $I(x')$ . Since the spa-

cial frequency spectrum of the fringes is a low frequency one ( $f_x$  lower than  $250 \mu\text{m}^{-1}$ ) while the noise occupies a region at high spatial frequencies (more than  $500 \mu\text{m}^{-1}$ ), this operation doesn't remove significantly information from the signal. This noise reduction is necessary for ellipsoids because differently from the spheres the azimuthal average can not be performed. Figure 2.24(b) shows the same profile of 2.24(a) after the noise reduction.

The advantage with ellipsoids, if compared with spheres, is the presence of several maxima and minima because of the high radius of curvature of the particle along the major axis. The possibility to have up to 10 reliable extrema allows the measure of the moduli of the semiaxis  $S_a$  and  $S_b$  (fig. 2.21(c)) directly from the intensity profile of the interference system.

The starting point for the measure of the semiaxes is the reconstruction of the particle-interface distance  $z_s(x'_e)$  for each extremum located at different  $x'_e$  along  $x'$ . The superimposition of two beams having a difference of  $2n_1z_s/\lambda$  in the optical path gives an interference signal whose intensity is proportional to  $1 + \cos(4\pi n_1z_s/\lambda)$ . The difference in  $z_s$  between two adjacent extrema (either a couple maximum-minimum or minimum-maximum) is therefore equal to  $\lambda/4n_1$ . Knowing that the center of the interference pattern corresponds to the closest point to the interface, the reconstruction can be made (figure 2.25(b)).

In principle, the points obtained in figure 2.25(b) allow to recover from a proper elliptic fit  $S_a, S_b, x'_c, z_c$  and  $\theta_e$ . In practice, the number of points in fig.2.25(b) is too small with respect to the number of free parameters to obtain a sufficient precision in the fit parameters. For this reason the ellipsoid's parameters are found in two steps. We first measure  $S_a$  and  $S_b$  by averaging all the reconstructed  $z$ -profiles of the same ellipsoid: the  $z_s(x'_e)$  recovered from all the frames are superimposed on the same plot (fig.2.25(c)). A given extremum represents a fixed relative distance from the interface. Fluctuations both in  $z$  and in the tilt angle generates a dispersion in the position  $x'_e$ . In figure 2.25(c) the red points represent the average position for each considered extremum.

If the number of considered frames is enough<sup>17</sup>,  $x'_c$  and  $\theta_e$  are zero on average. The average profile is therefore fitted with the expression describing an ellipse parallel to  $x'$ :

$$\langle z_s(x') \rangle = \langle z_c \rangle - S_b \sqrt{1 - \frac{x'^2}{S_a^2}} \quad (2.14)$$

From the best fit, we obtain  $S_a$  and  $S_b$  with typical errors of 1-2  $\mu\text{m}$ .

Once the values of the semiaxes are known, the center coordinates and  $\theta_e$  can be found as a function of time: for each frame the profile of figure 2.25(b) is fitted keeping fixed  $S_a$  and  $S_b$  and leaving  $x'_c, z_c$  and  $\theta_e$  as free parameters. The fitting function is obtained rotating by an angle  $\theta_e$  the ellipse equation used eq. 2.14:

$$z_s(x') = z_c - \frac{(x' - x'_c) \mathcal{B}(\theta_e)}{2\mathcal{A}(\theta_e)} + \frac{\sqrt{(x' - x'_c)^2 \mathcal{B}^2(\theta_e) - 4\mathcal{A}(\theta_e) \left( (x' - x'_c)^2 \mathcal{C}(\theta_e) - 1 \right)}}{2\mathcal{A}(\theta_e)} \quad (2.15)$$

<sup>17</sup>Considering the measured range of tilt angles, it has been verified that the frames must be at least 2000.

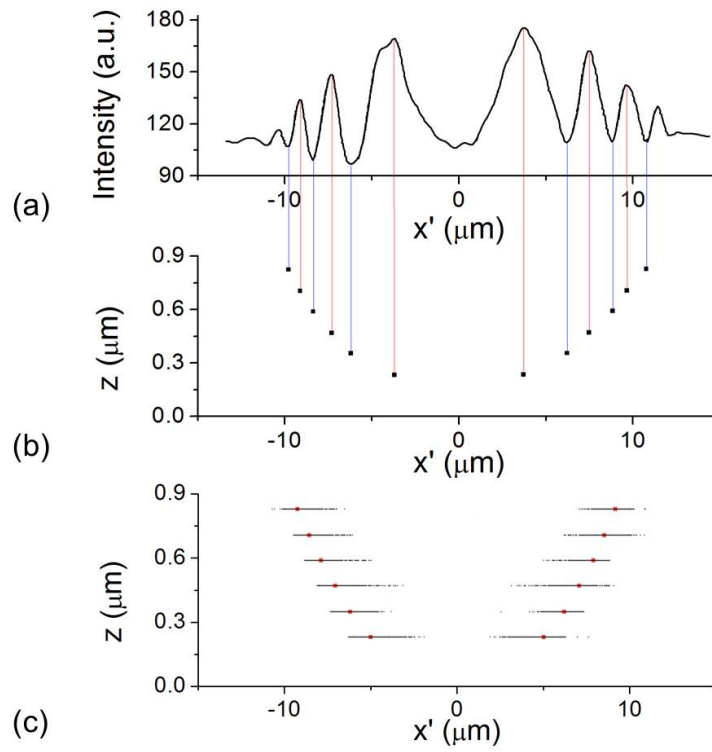


**Figure 2.25:** Reconstruction method to measure the semiaxes of an ellipsoid. (a) The position  $x'_e$  of the extrema along the ellipsoid's long axis is found. (b) Knowing the difference in  $z_s$  between two adjacent extrema is  $\lambda/4n_1$ , the  $z_s(x'_e)$  profile on the ellipsoid is reconstructed. (c) The latter operation is made for all frames on the same particle and the  $x'_e$  positions corresponding to the intensity extrema are plotted on the same graph (black points). For each extremum the average position on the frames is evaluated (red points). These are the points fitted to recover the moduli of the semiaxes of the ellipsoid.

Where  $\mathcal{A}(\theta_e)$ ,  $\mathcal{B}(\theta_e)$  and  $\mathcal{C}(\theta_e)$  are defined as:

$$\mathcal{A}(\theta_e) = \left(\frac{\sin \theta_e}{S_a}\right)^2 + \left(\frac{\cos \theta_e}{S_b}\right)^2 \quad (2.16)$$

$$\mathcal{B}(\theta_e) = 2 \cos \theta_e \sin \theta_e \left(\frac{1}{S_b^2} - \frac{1}{S_a^2}\right) \quad (2.17)$$

$$\mathcal{C}(\theta_e) = \left(\frac{\cos \theta_e}{S_a}\right)^2 + \left(\frac{\sin \theta_e}{S_b}\right)^2 \quad (2.18)$$

The coordinates of the center of the particle in the plane of the lab frame are finally found from  $x'_c$  and the angle  $\varphi_e$  as  $x_c = x_0 + x'_c \cos \varphi_e$  and  $y_c = y_0 + x'_c \sin \varphi_e$ .

As for spheres, with this method  $z_c$  is known up to an additive factor  $m\lambda/2n_1$ . The value of  $m$  is then found following the same procedure described in section 2.2.1: from each wavelength the trajectory is obtained and the correct  $m_R$ - $m_B$  couple is identified as the one minimizing  $|\langle z_c^R - z_c^B \rangle_t|$ . The error on  $z_c$  is obtained from the covariance matrix of the fit.

# Chapter 3

## Materials and methods

In the present chapter some details are given on the choice of the particles and on the preparation of the samples (section 3.1), followed by the description of the experimental cell (section 3.2). A brief list of the complementary techniques used during the work is also given in section 3.3.

### 3.1 Materials' choice

We used spherical and ellipsoidal particles dispersed at very low concentrations ( $10^{-3} - 10^{-2}$  g/L, corresponding to a particle density number close to the interface of  $10^1 - 10^2$  nm<sup>-1</sup>). Particles were dispersed in water solutions prepared with deionized water. Deionized water is produced by a Millipore Milli-Q filtration system, with a nominal resistivity of 18 MΩcm and a density  $\rho_w = 0.997$  g/cm<sup>3</sup> at 25°C. Conductivity measurements (see sec.3.3) show that its effective resistivity measured few minutes after deionization is 2 MΩcm. Experiments are made with solutions of different molarity, pH and density.

#### 3.1.1 Spherical particles

The spherical particles employed in the present thesis are polystyrene latex beads with a diameter of about 9 μm. Their low density  $\rho_{col} = 1.055$  g/cm<sup>3</sup> assures a strong enough buoyancy to avoid the trapping at the air-pure water interface<sup>1</sup>.

Two different sets of polystyrene beads have been used. Most of the measurements are made with sulfate beads<sup>2</sup> with a diameter  $2a = 8.7 \pm 0.9$  μm. The relatively large polydispersity is an advantage in our case as it allows to explore the possible size dependency of the measured effects. In order to have a tunable surface charge we also used pH-sensitive carboxylated beads<sup>3</sup> with  $2a = 8.9 \pm 0.1$  μm.

The choice of diameter is driven by the need to have a sufficient number of fringes for the  $z$  reconstruction, as described in section 2.2.2, and at the same time to keep the size small enough to observe Brownian motion.

Polystyrene particles have also been chosen because of the refractive index of 1.59 which maximizes the fringe visibility of the interference pattern given that the refractive jump between polystyrene and water ( $\Delta n_{p-1} = 1.59 - 1.33 \sim 0.3$ ) is almost

---

<sup>1</sup>Tests made with particles at higher density (silica beads) result in a direct trapping of the particles at the interface.

<sup>2</sup>*MolecularProbes™* sulfate latex beads, 4% w/v, 9 μm.

<sup>3</sup>*Micro Particles GmbH* PS-particles, carboxylated, 8.91 μm, SD=0.1 μm, 10% w/v aqueous suspension.

the same of the one between water and air ( $\Delta n_{1-2} = 1.33 - 1.0 \sim 0.3$ ). See appendix A for further details.

### 3.1.2 Ellipsoidal particles production

The ellipsoidal particles have been produced in the laboratory starting from the sulfate latex beads which are stretched by a homemade apparatus [107]. A Poly(vinyl alcohol) (PVA)<sup>4</sup> solution in deionized water (10%-90%) is prepared by mixing the components by several cycles of shaking at 300 rpm and heating at 90-100°C (30-60 min for each operation), until a homogeneous phase is obtained. The solution is then filtrated with a hydrophobic filter PTFE (pores dimension: 5  $\mu\text{m}$ ) to remove macroscopic dust before adding the beads. A volume of about one milliliter of the spherical particle sample is dispersed in 40 ml of the PVA-water solution. The resulting solution is then slowly poured in a Petri dish (diameter 100 mm) which, before use, was carefully cleaned with distilled water. Great attention is paid to avoid the formation of air bubbles, whose presence may affect the stretching procedure. The solution is then left to evaporate in a hood for 1-2 days on a flat surface. Finally, a thin film of PVA (thickness  $\sim 0.2$  mm) containing the spherical particles is obtained. Strips are cut from the dried film, with special regard to the central region, that must be extremely regular; otherwise, a non-homogeneous stretching can distort the final shape of the colloids. The strips are clamped into a metal frame, heated in an oven above the temperature of glass transition of polystyrene ( $T_g \sim 100^\circ\text{C}$ ) and then stretched. The stretching of both the strip and the particles embedded inside is achieved by displacing the upper part of the metal frame by a tension-controlled screw, with a displacing rate of 12 mm/min. In this way, the spherical particles undergo an affine transformation and a spheroidal shape is achieved (fig. 3.1(a)). The strips are finally soaked in deionized water and PVA is removed by at least 10 cycles of centrifugation (4000 rpm for 10-15 min), replacing the supernatant with Millipore water at the end of each cycle. At the end, the ellipsoids are re-dispersed in deionized water with the aid of an ultrasonic bath. A SEM picture of typical particles obtained after such a procedure is shown in fig. 3.1(b).

We can denote with  $\Lambda$  the elongation imposed at both the strip and the particles. It is defined as the ratio between the final and the initial length of the strip (fig. 3.1(a)):  $\Lambda = l/l_0$ . It follows that, along the stretching direction, a major semi-axis is obtained:  $S_a = \Lambda a$ . Since the total volume of the particle remains constant, i.e.  $S_a S_b^2 = a^3$ , the two minor semi-axes, in the perpendicular plane, are  $S_b = a/\sqrt{\Lambda}$ . We can quantify the degree of anisotropy of each particle using the aspect ratio  $Ar = S_a/S_b$ . Sets of particle with the same initial size, and so the same volume, but different elongation are prepared and used in the present work. The range for  $Ar$  can vary from 1 (unstretched spheres) to about 10, that is the upper limit imposed by the stretching method.

### 3.1.3 Solutions preparation

In order to change the ions molarity in water we use sodium chloride<sup>5</sup>. Different molarities in a range spacing from the one of deionized water (0.004 mM) up to 10 mM have been prepared. Since anhydrous NaCl is hygroscopic, before its weighting for the dilution in water it is dried in an oven at 100°C.

<sup>4</sup>Sigma Aldrich (product code 363081).

<sup>5</sup>Sigma-Aldrich NaCl anhydrous,  $\geq 99\%$ , reference 746398.

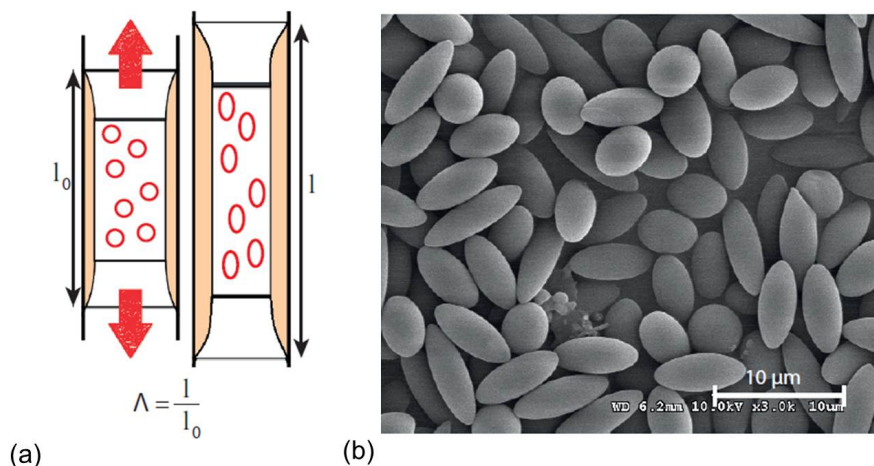


**Figure 3.1:** (a) Sketch of a PVA strip, containing spherical particles. The initial length of the strip is  $l_0$ . A stretching of the strip along the vertical axis is imposed. The new length is then  $l$ . We define an elongation parameter  $\Lambda = l/l_0$ . The same elongation is imposed also to the particles, that now show an ellipsoidal shape. (b) SEM image of the ellipsoids obtained.

The pH is varied adding given amounts of hydrochloric acid<sup>6</sup>. Since addition of HCl changes the molarity together with the pH, solutions at different pH but with constant molarity are prepared adding NaCl, whose ions are monovalent like the ones of HCl. For this reason, everywhere in the present work we use the word *molarity* without specifications we mean the molar concentration of NaCl and HCl together. We indicate it with  $c$ .

Temperature [108] and molarity [109] affect the density of solutions. Temperature is monitored with a thermometer during experiments and the effective density of each solution is carefully evaluated using data in literature with three digits of precision.

After preparation, solutions are stored in a fridge in order to slow down the possible uncontrolled development of bacteria. Molarity is verified by measuring the solution's conductivity: deionized water doubles its resistivity in one day, passing from  $0.5 \mu\text{S}/\text{cm}$  to  $1 \mu\text{S}/\text{cm}$ , due to adsorption of ions from the atmosphere and from the container's walls. Solutions at high molarities (1 mM or more) are kept for several weeks because such small variation in ions concentration doesn't affect the molarity. On the contrary, solutions at low molarity are conserved only for few days to avoid significant changes in ions concentration.

The properties of the solution may be influenced during experiments by the adsorption of ions and contaminants from atmosphere onto the air-water interface. In order to verify the stability of the solution's properties during experimental time scales we measure the solutions surface tension at different times, as the trapping of a significant amount of surfactants at the interface lower its surface tension [110]. The pendant drop tensiometer described in section 3.3.3 allows the measurement of the solutions in experimental conditions and time scales analogous to our experiment. The test shows that the surface tension remains constant at values between 72 and 72.5 mN/m, in agreement with the expected values [111], during all the du-

<sup>6</sup>*Sigma-Aldrich*, HCl 36.5-38.0%, reference H1758.

ration of the tensiometry measurement ( $> 4$  hours, more than the duration of our experiments) for all the prepared solutions .

## 3.2 The experimental cell

The sample container employed for experiments is a cell made by a glass cylinder glued on a glass microscope slide (figure 3.2). The cylinder has an internal diameter of 8 mm and a height of 4 mm. The two part of the cell are fixed with an UV glue<sup>7</sup>. Before performing experiments, the cell is cleaned several times with ethanol and rinsed abundantly with deionized water.

A volume of 250  $\mu\text{l}$  solution is injected in the cell with a syringe. Deionized water dilution of particles are previously prepared cleaning them by several cycles of centrifugation, replacing the supernatant with Millipore water at the end of each cycle, in order to remove surfactants and impurities eventually present in the sample. A volume of 2  $\mu\text{l}$  of the dilution of particles is subsequently added in the cell using a micro-pipette. The cell is then turned upside down as in a pendant drop geometry and placed on the sample stage of the microscope. The sample stage's hole for light microscopy has a diameter, of 20 mm, larger than the cell's cylinder but smaller than the microscope slide: the cell is laid on the sample stage keeping the cylinder inside the hole (figure 3.2(b)). Silicone-based high vacuum grease is spread between the cell and the stage in order to reduce evaporation. After 15 minutes enough colloids are sedimented close to the interface and the measurements can be performed.

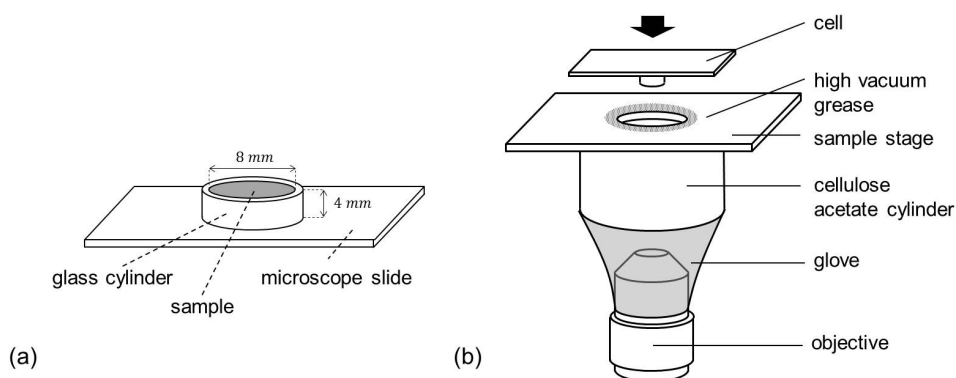


**Figure 3.2:** Sketch of the simple cell (a) and of the system of the cell, sample stage and anti-evaporation chamber (b).

To reduce evaporation, the cell has to be isolated. An attempt has been to close the cell putting a cover slip below the hole of the sample stage, but in that way the glass between the cell and the objective introduces distortions on the fringe system. We therefore decide to avoid it and chose to build a chamber between the sample stage and the objective, as depicted in figure 3.2(b). The chamber is made by a thin sheet of cellulose acetate, which forms a rigid cylinder of 20 mm radius and a height of 40 mm. It is fixed below the sample stage and connected to the objective with a cut wrist of a nitrile glove, which is fixed with the tip to the cylinder and with a rubber band to the objective. The 60 mm diameter of the chamber's cylinder has been chosen in order to allow the free displacement along  $x$  and  $y$  of the sample

<sup>7</sup>Norland Optical Adhesive 81.

stage, while its height is much larger than the geometry needed in order to keep the glove as far as possible from the cell. We indeed noticed that the electrostatic charges present on the glove induce a strong drift (hundreds of micrometers per second) on the charged colloids in the cell. To create additional protection from electrostatic charges the inner part of the cellulose acetate cylinder is coated with an aluminium sheet in order to have a Faraday cage. The efficiency of the chamber in reducing evaporation is evaluated in sec. 3.2.2.

A second type of cell was designed to tune the molarity and density of the solution during the measure. This setup was built in order to collect data on the same particle for different values of the solution's physico-chemical properties. The solution inside the cell can be changed using two input capillaries to inject/remove liquid from the cell.

However, technical problems of diffusion inside the cell renders very difficult the evaluation of the time evolution of the solution's parameters. These measurements have not therefore given significant results.

### 3.2.1 Particle's drift

Apart from the eventual effect coming from external electrostatic charges, other sources of  $xy$  drift velocity experienced by particles close to the interface are present. Among them, the main one is the air displacement around the cell. The isolation of the cell and the objective in the chamber described in section 3.2 reduces drift to values lower than  $1 \mu\text{m/s}$ , while in samples with open cell drifts up to values of the order of  $10 \mu\text{m/s}$  were observed. The reduction of the drift has been an important improvement since it avoids that particles cross the field of view so fast to make impossible the tracking. Drift velocity variations during measurements always remained small enough to be neglected.

### 3.2.2 Evaporation

Due to the time scale of the experiments of 1-2 hours the contribution of evaporation must be considered because of the appreciable displacement of the interface it causes and because of the change of the total volume of the sample, which could affect the chemicals' concentrations in the solution.

To evaluate the evaporation rate the piezoelectric actuator has been used to move the objective keeping in focus a fixed point on the interface in the center of the cell. The velocity of displacement of the surface, corresponding to the evaporation rate, is thus calculated from the piezo's displacement  $\Delta z_{piezo}(t)$  (recorded by the controlling software).

For a cell exposed to the atmosphere without protections against evaporation, the evaporation rate is constant in time with a velocity of the air-liquid interface of about  $0.2 \mu\text{m/s}$  at room temperature. This value undergoes deviations of less than 10% for a room temperature range between  $20^\circ\text{C}$  and  $28^\circ\text{C}$  and with a relative humidity of 50-60% (the average at Montpellier, France). By protecting the cell with the glove chamber, the interface velocity lowers to a stationary value of  $0.05 \mu\text{m/s}$  after half an hour from the start of the experiment. All the measurement are therefore been made after 30 minutes from cell's preparation.

The variation of the volume  $\Delta V$  as a function of the displacement of the center  $\Delta h$  of the air-liquid interface is

$$\Delta V = \frac{\pi a_{cell}^2}{2} \Delta h \quad (3.1)$$

Where  $a_{cell}$  is the radius of the cell's section. Considering the cell dimensions (cylinder with radius 4 mm and height 4 mm) and the measured velocity of the interface, the resulting volume evaporation rate is  $0.08 \mu\text{l}/\text{min}$  and the variation of the total volume of water during an experiment is of the order of 5%. Such variation of the concentration of NaCl and HCl dissolved in water is lower than the precision in the preparation of the solution and therefore can be neglected.

### 3.2.3 Drop's shape

The study of the dynamics of the particles close to the interface must take into account the shape of the interface. Both the optical analysis to recover the particle's coordinates and the dynamics theories start from the assumption of a flat surface. The evaluation of the interface's curvature and the eventual implications must therefore be discussed. The main effect inducing a curvature change in time is the evaporation: during the experimental time scale ( $10^3 - 10^4$  s) it yields a displacement in  $z$  of the center of the surface of the order of 1 mm. Accordingly, if the starting interface is flat, at the end there will be a concavity of the drop macroscopically visible. As a consequence it has been preferred to start with a convex interface with a height  $\tilde{h}$  of the center of the drop of about 1 mm (fig. 3.3(a)). In this way during experiments the curvature helps to push the particles towards the center of the cell contrasting the drift. A concave air-water interface would instead make the measurement very difficult since almost all the particles would be close the cell's walls.

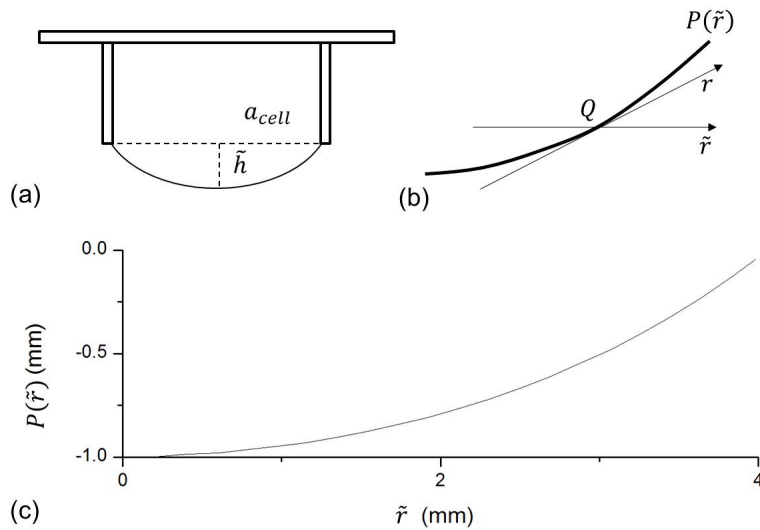


**Figure 3.3:** Geometries for the study of drop's shape. In (a) a sketch of the drop's initial convex shape is given, with  $\tilde{h}$  being the height of the convex part in the central part of the drop. In (b) the two reference systems parallel to the interface ( $r$ ) and perpendicular to the optical axis ( $\tilde{r}$ ) are depicted for a particle in the point  $Q$ . The  $r$  coordinate runs along the profile function  $P(\tilde{r})$  of the drop. In (c)  $P(\tilde{r})$  is reported as it is obtained from the Mathematica code.

The interface curvature could affect the data in two main ways. Firstly, it implies that there is a tilt angle between the optical axis and the normal to the interface everywhere except from the center of the cell. This tilt angle could induce a parallax

error in the measurement of the displacement of  $x$  and  $y$ , since this reference system parallel to the surface is different from the one of the recorded image  $\tilde{x}\tilde{y}$  (see fig. 3.3(b)). To evaluate this contribution an analysis has been made starting from a Mathematica code [112] which provides the shape of the drop starting from its radius ( $a_{cell}$ ),  $\tilde{h}$  and the surface tension. The profile function  $P(\tilde{r})$  of the drop has been recovered as a function only of the radial coordinate  $\tilde{r}$ , because of to the polar symmetry of the drop, for a drop with  $a_{cell} = 4$  mm and  $\tilde{h} = 1$  mm and the surface tension of an air-water interface (fig.3.3(c)). The definition of  $r$  is given, as a function of  $\tilde{r}$ , as the length of the function  $P$ :

$$r = \int_0^{\tilde{r}} \sqrt{1 + \left(\frac{dP}{dq}\right)^2} dq \quad (3.2)$$

Considering the drift that has been observed in the data, the maximum distance from the beginning position a particle can reach during its trajectory is less than 300  $\mu\text{m}$  (value obtained for a drift of 0.5  $\mu\text{m/s}$  in a measurement of 10 minutes). In the case where the drift is in the radial direction and towards the walls of the cell the discrepancy between the traveled path  $\Delta\tilde{r}$  and the projection  $\Delta r$  visualized on the screen is maximum. Let us thus consider this limiting case in order to find the upper limit of the error. For  $\Delta\tilde{r} = 300$   $\mu\text{m}$  the travelled path starting from  $\tilde{r}$  is:

$$\Delta r = \int_{\tilde{r}}^{\tilde{r}+\Delta\tilde{r}} \sqrt{1 + \left(\frac{dP}{dq}\right)^2} dq \quad (3.3)$$

This quantity as been evaluated and it has been found that the relative error  $\frac{\Delta r - \Delta\tilde{r}}{\Delta r}$  is the 0.1% starting from an initial position  $\tilde{r} = 3$  mm and less than 0.01% starting near the center of the cell. This parallax error is therefore negligible.

The second way the curvature can be relevant is in the particle dynamics: if the particle is studied close to a flat surface the Brownian motion in  $xy$  is free without components of the forces parallel to the surface, but for a curved surface there will be a confinement force. If the curvature of the air-water is locally relevant only because of its slope and if that slope is locally constant the component of the force will be constant and a simple constant contribution to the drift is added. Conversely, if the slope locally changes, the effect on the dynamics is more relevant, but it should be immediatly evident looking at the MSD of the motion parallel to the interface. Linearity of MSD in  $xy$  (see section 5.1) ensures the negligibility of this effect on the dynamics.

Since contributions of drop's curvature are evaluated negligible both for the tracking and for the dynamics, we can superimpose the  $\tilde{x}\tilde{y}$  reference system to the  $xy$  one.

In addition to the macroscopic curvature, there is also a local deformation of the interface operated by the particle's force exercised on it which also could affect the dynamics of the particle. The only force pushing the colloid towards the air-water interface is gravity. The sum of particle-interface interactions and gravity keeps the particle at an equilibrium mean distance  $d$  from the interface but if the amplitude of the gravity force is large enough the interface is deformed and it will no longer be superimposed to the plane  $z = 0$ . Let us consider the effect of a heavy spherical particle (see figure 3.4). The interface minimum ( $z_0 < 0$ ) is located at  $(x_c, y_c)$  below the particle center. Following [113],  $z_0$  can be evaluated as follows. Assuming the interface linearly elastic, the force exerted by the particle on it can be written as:

$$F = k_{int} z_0 \quad (3.4)$$

Where  $k_{int}$  is the effective spring constant of the interface. In the meantime the force is given by the weight of the particle together with the buoyancy, so  $z_0$  can be written as:

$$z_0 = \frac{m^* g}{k_{int}} \quad (3.5)$$

With  $m^* = \frac{3}{4}\pi a^3 (\rho_p - \rho_1)$  being the effective mass.

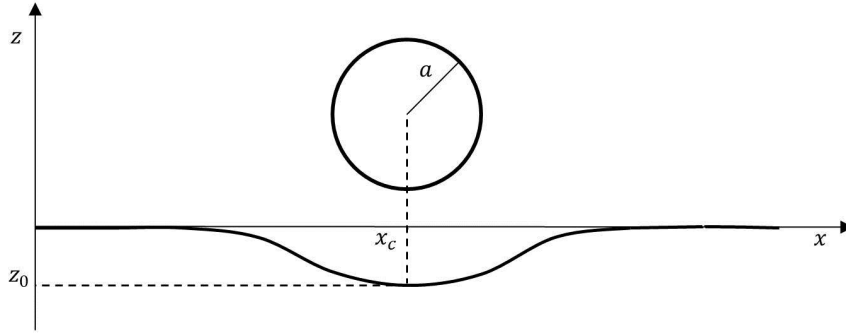


**Figure 3.4:** Bidimensional sketch of the geometry of the deformation of the air-water interface operated by the sphere due to its weight. The maximum displacement  $z_0$  of the interface from its equilibrium position is in correspondence of the center of the particle  $x_c$ .

To estimate  $k_{int}$  we can consider the surface flat at rest. The elastic free energy required to change the flat cross-sectional area,  $A_0$ , to the depressed area,  $A_1$ , can be written as:

$$E(z_0) = \gamma_{AW} (A_1 - A_0) \quad (3.6)$$

It can be shown [113] that:

$$A_1 - A_0 = \pi z_0^2$$

and so we have

$$E(z_0) = \pi z_0^2 \gamma_{AW}$$

$$F(z_0) = 2\pi z_0 \gamma_{AW}$$

from which we get

$$k_{int} = 2\pi \gamma_{AW} \quad (3.7)$$

$$z_0 = \frac{2}{3} \frac{a^3 (\rho_p - \rho_1) g}{\gamma_{AW}} \quad (3.8)$$

The evaluation of  $z_0$  for the system under study gives a value of the deformation of the order of  $10^{-13}$  m which is therefore negligible because even smaller than the molecular size.

### 3.3 Complementary techniques

#### 3.3.1 Conductometry and pH-metry

Conductivity measurements are made on the solutions employed for experiments in order to check the molarity and to monitor its time evolution due to the absorption of ions from the environment. The ratio between the measured conductivity  $\Sigma$  and the molar conductivity  $\Sigma_M$  of the dissolved species (NaCl and HCl in our case) gives the molarity value of that species in the solution. The instrument used for the measure is a **digital pH/dissolved oxygen/conductivity meter**<sup>8</sup>. It employs a cylindrical hollow probe with two electrodes on its inner wall. The probe is immersed in the solution, an alternating current is applied to the electrodes and the potential between them is measured. Conductivity could in principle be determined using the distance between the electrodes and their surface area using Ohm's law but, for accuracy, a calibration is made measuring periodically a known molar solution. The probe also has a temperature sensor since the molar conductivity is temperature-dependant.

If the pH probe is mounted on the instrument the pH of the solution can also be measured. The pH-metry is based on the measure of a voltage arising between two electrodes once they are immersed in the solution. The probe is a glass rod with a bulb containing the electrodes. It is specifically designed to be selective to hydrogen ion concentration. Once immersed in the solution, hydrogen ions are exchanged with other positively charged ions on the glass bulb, creating an electrochemical potential across the bulb. The electronic amplifier detects the difference in electrical potential between the two electrodes generated in the measurement and converts the potential difference to pH units. The magnitude of the electrochemical potential across the glass bulb is linearly related to the pH according to the Nernst equation [114].

#### 3.3.2 Zeta Potential measurements

Measure of the Zeta potential has been made during the work in order to get informations about the surface potential of the colloids at different molarities. The employed instrument is a **Zetasizer**<sup>9</sup>, which uses laser doppler micro-electrophoresis to get the Zeta potential of the particles. An electric field is applied to a dispersion of particles, which then move with a velocity depending on their Zeta potential. This velocity is measured using a patented laser interferometric technique called M3-PALS (Phase analysis Light Scattering). This enables the calculation of electrophoretic mobility, and the average Zeta potential and its distribution are calculated.

The concentration of particles must be sufficient large to get enough signal (thousands of counts) but low enough to avoid multiple scattering (light have to pass in transmission through the sample). The concentration of the measured solution is about 1 mg/ml. The solutions are prepared mixing mother solutions of *i*) deionized water and sodium chloride, *ii*) deionized water and hydrochloric acid, *iii*) deionized water and microparticles together with *iv*) bare deionized water in order to obtain the desired concentration of all the species in the solutions. Both sulfate and carboxylate beads have been measured in this way.

Once prepared, the solution is loaded in a folded capillary cell equipped with two electrodes, which is then inserted in the instrument's compartment. For each sample three measurements are made before sedimentation of the particles makes

<sup>8</sup>WTW, Multi 9420.

<sup>9</sup>Malvern Instruments, Zetasizer Nano ZS.

the concentration of suspended particles too low. As output the Zetasizer's software gives the distribution of the Zeta potential, the conductivity of the solution and the temperature.

### 3.3.3 Tensiometry

Surface tension of the interface between air and the solutions employed in experiments is measured with a **profile-analysis tensiometer**<sup>10</sup>. Its principle is based on the analysis of the shape of pendant or sessile drops of the liquid. It is controlled by its proper software and has a range spacing between 1 and 2000 mN/m with a resolution of 0.01 mN/m.

The measurement requires a manual centring of the drop in the field of view of the camera, then all is automated. The software identifies the border of the drop and makes a fit of its shape. From the fit the surface tension between air and the drop is extracted. A motorized syringe ejects a given volume of liquid forming the drop and the measure starts once the drop is formed. The evolution of  $\gamma$  over time can be thus monitored.

---

<sup>10</sup>*Sinterface*, Profile Analysis Tensiometer PAT1M.

## Chapter 4

# Interaction between a spherical particle and an air-liquid interface

In this chapter are described the measurements of the interaction potential between a spherical particle and the air-liquid interface once the particle is sedimented to the interface.

In figure 4.1, a typical trajectory obtained from the method and the analysis described in chapter 2 is shown: in 4.1(a) the whole 3D trajectory is given, while in 4.1(b) and 4.1(c) are shown the projection on the  $xy$  plane parallel to the air-liquid interface and the time dependence of the particle-interface distance  $d$ .

As illustrated in figure 4.1(c), the particle dynamics can be divided in three main regimes. In the **sedimentation regime**, the particle moves towards the interface driven by gravity. The sedimentation velocity decreases as the particle approaches to the interface because of the increasing viscous drag (section 1.2) and of the interaction with the interface.

After sedimentation, the particle reaches a metastable equilibrium at a gap distance  $d_0$  of a few hundreds on nanometers from the interface. In this **equilibrium regime**, the colloid freely diffuses in the  $xy$  plane, while the motion along  $z$  is confined by the combination of the interaction with the interface and the gravity. The equilibrium regime lasts few seconds to tens of hours depending on the considered particle and on molarity and pH of the solution.

Surprisingly, two equilibrium positions are observed. One equilibrium position ( $d_0^I$ ) can be recovered considering double-layers, van der Waals and gravity interactions, contrary to a second one ( $d_0^{II}$ ) which is not predicted by such interactions.

The final **interface crossing regime** (sec.4.3) is observed only for relatively high molarity of the aqueous solution and starts when a particle suddenly jumps from one of the two equilibrium positions, where the particle is completely wetted, to a position where the particle is only partially immersed in the liquid. Once the interface is touched the partial de-wetting of a particle region begins. Its slow dynamics ends when the receding equilibrium contact angle with the air-water interface is reached.

In this chapter results concerning the equilibrium regime (sec. 4.1 and 4.2) are reported for both sets of used polystyrene spherical particles: sulfate spheres (SS) and carboxylated spheres (CS). The interface crossing regime is described in section 4.3. Finally, a discussion on the particle-interface interaction potential is made and a comparison between data and models is given (sec. 4.4).

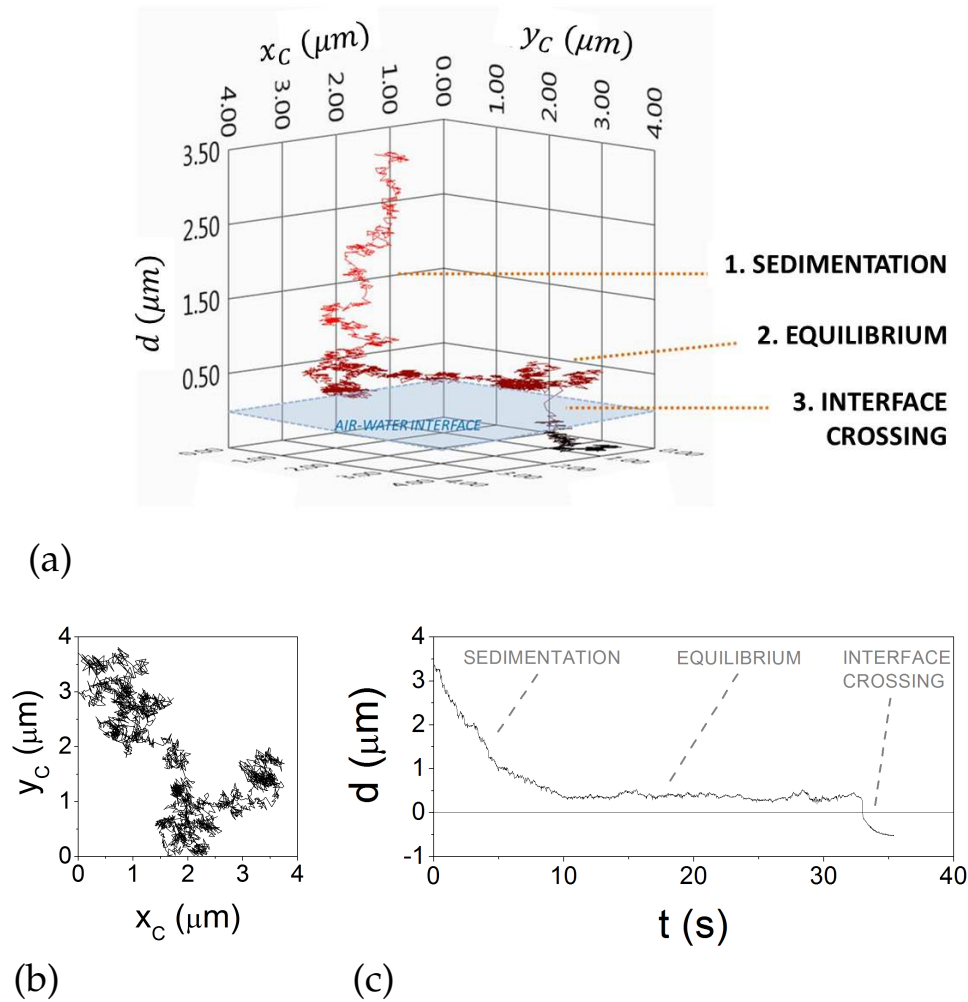


**Figure 4.1:** Complete 3D trajectory of a spherical polystyrene particle with radius  $4.5 \mu\text{m}$  approaching to the air-water interface. Data represent the position of the particle's closest point to the interface with respect to the interface. The dynamics can be decomposed in three regimes: the sedimentation towards the interface, the equilibrium at a given distance from the interface and the interface crossing. (a) 3D trajectory. (b) Projection of the trajectory on the  $xy$  plane parallel to the interface. (c) Time evolution of the particle-interface distance  $d$ .

## 4.1 Measurements of the predicted electrostatic equilibrium

Figure 4.2(a) reports a typical result obtained for the particle-interface distance  $d$  versus time during the equilibrium regime. The motion is confined along the  $z$  direction with fluctuations around an equilibrium position. Such dynamics indicates that the particle is moving by thermal energy in a potential well determined by the gravity and the interaction with the interface.

The potential energy of a particle can be studied from the fluctuations around its equilibrium position  $d_0$  using the Boltzmann equation [115], which relates the probability  $p(d)dd$  of finding the particle at a distance between  $d$  and  $d + dd$  from the interface to the potential energy  $U(d)$  of the particle according to:

$$p(d) = A \exp\left(-\frac{U(d)}{k_B T}\right) \quad (4.1)$$

In eq. 4.1,  $A$  is a normalization constant which can be conveniently eliminated dividing by the probability of finding the particle at the equilibrium position  $d_0$ :

$$\frac{p(d)}{p(d_0)} = \exp\left(-\frac{\Delta U(d)}{k_B T}\right), \quad (4.2)$$

where  $\Delta U(d) = U(d) - U(d_0)$ . In the case of a large number of observations ( $N_{tot} \rightarrow \infty$ ), the ratio  $p(d)/p(d_0)$  can be approximated by the ratio  $N(d)/N(d_0)$  between the number  $N(d)$  of observations in the interval centered in  $d$  and the number of observations in the interval of the same width centered in  $d_0$ . In our case of large but finite  $N_{tot}$ , discrepancies between  $p(d)$  and  $N(d)/N_{tot}$  are quantified by the error per bin equal to [116, 117]:

$$\sigma_N = \sqrt{N(d) \left(1 - \frac{N(d)}{N_{tot}}\right)} \quad (4.3)$$

The incertitude on the probability  $\sigma_p$  can be derived from the one on  $N(d)$  through error propagation formula:  $\sigma_p = \sigma_N/N_{tot}$ . Typical values of  $N_{tot}$  in our experiments are about  $10^4$ , resulting in relative errors on  $p(d)$  of the order of 1-10%.

The potential difference  $\Delta U$  in eq. 4.2 then reads:

$$\frac{\Delta U(d)}{k_B T} = -\ln \frac{p(d)}{p(d_0)} \approx -\ln \frac{N(d)}{N(d_0)} \quad (4.4)$$

with an error

$$\sigma_{\Delta U/k_B T} = \frac{\sigma_p}{k_B T} \left| \frac{\partial(\Delta U)}{\partial p} \right| = \frac{\sigma_p}{p(d)} \quad (4.5)$$

In figure 4.2(b) is reported the histogram  $N(d)$  corresponding to the trajectory in fig. 4.2(a). The bin size is chosen in order to have a significant number of counts in each bin and enough bins to reconstruct the shape of the potential. In figure 4.2(c) the potential energy difference  $\Delta U(d)$  obtained using eq. 4.4 is reported. The obtained

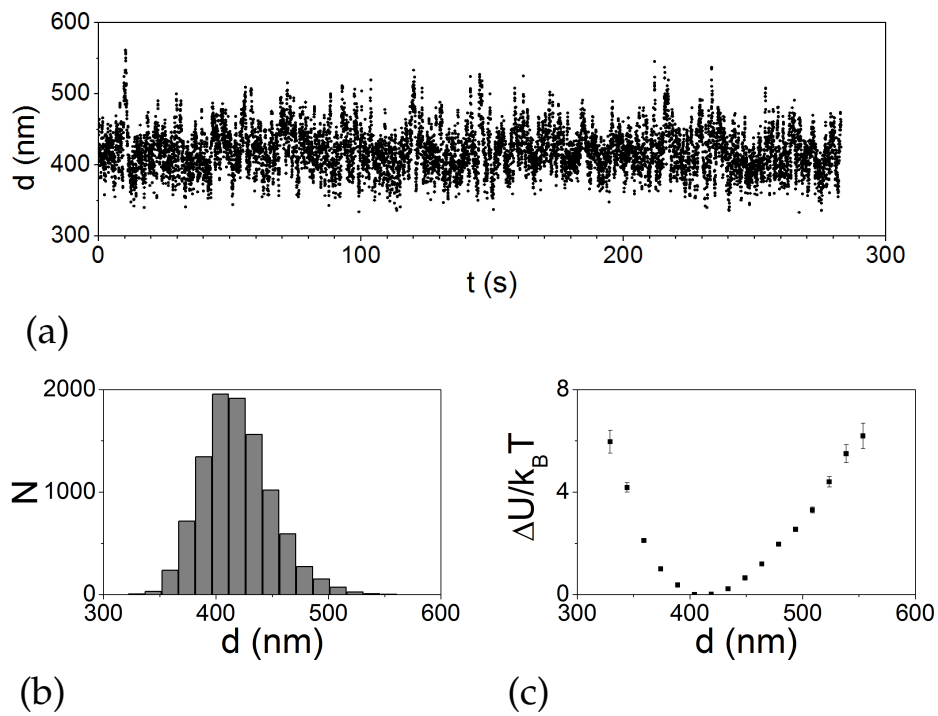


**Figure 4.2:** (a) Plot of a typical  $d(t)$  for a sulfate sphere with radius  $4.5 \mu\text{m}$  fluctuating around its equilibrium position. (b) Histogram of distances extracted from the trajectory in (a). (c) Profile of the potential energy difference  $\Delta U(d)$  obtained from (b) using eq. 4.4.

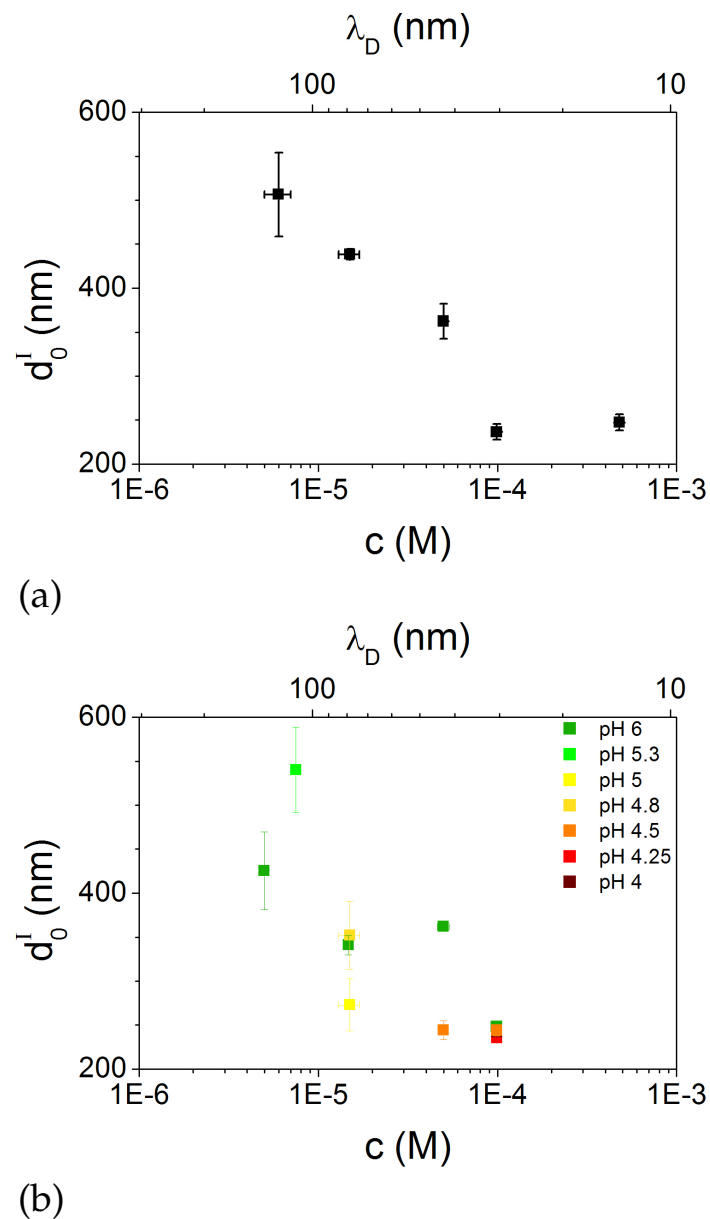


**Figure 4.3:** Plot of the average  $d_0^I$  as a function of molarity for the sulfate (a) and the carboxylated (b) spherical particles. The averages are made over 5-20 particles in solutions at same molarity. Error bars on the abscissa are due to the experimental errors in solution preparation. Top scale reports the Debye screening length  $\lambda_D$  corresponding to the molarity of the bottom scale. For CS, different colors represent different pH values as detailed in the legend.

potential well is not symmetric with respect to the minimum located in  $d_0^I$ : the slope of the attractive side ( $d > d_0^I$ ) is lower than the one of the repulsive side ( $d < d_0^I$ ).

Measurements have been made at different molarities and pH adding NaCl and HCl respectively, as described in section 3.1.3. The dependence of  $d_0^I$  on molarity<sup>1</sup> is reported in figure 4.3 for both SS (a) and CS (b) particles. Each point is the averaged value of the  $d_0^I$  made over 5-20 particles in solutions at same molarity. For the CS, whose surface charge is pH-sensitive (sec. 3.1), the figure also gives results for different pH. The top scale of figure 4.3 reports the Debye screening length<sup>2</sup>  $\lambda_D$  correspondent to the molarity of the solution. The distance  $d_0^I$  in figure 4.3 decreases with molarity for both SS and CS particles: colloids come closer to the interface as the ions concentration increases in the solution. The distances are always much larger than the Debye screening length and slightly vary with molarity: they change by a factor *ca* 3 when the Debye length varies of a factor 10. In fig. 4.3(a) it can also be seen that for molarities larger than  $10^{-4}$  M ( $\lambda_D$  lower than 30 nm) the particle-interface distance seems to become independent from molarity, suggesting that the electrostatic contribution to the potential becomes negligible at these ionic concentrations. The same conclusion is reached considering the pH dependency of  $d_0^I$  for CS colloids in fig. 4.3(b): while at  $c = 5 \cdot 10^{-5}$  M the equilibrium distance decreases with pH (*i.e.* when the surface charge of the particle increases), at  $c = 10^{-4}$  M all  $d_0^I$  obtained for different pH have the same value. This suggests that at  $c = 10^{-4}$  M the equilibrium distance is not determined by the surface charge of the spheres.

In figure 4.4, the equilibrium distance  $d_0^I$  of SS particles is reported versus particles radii. Each point corresponds to a single sphere. For a given molarity (a given color in figure 4.4),  $d_0^I$  has no a trend with  $a$ . Accordingly, the dispersion in  $d_0^I$  cannot be related to the radius polydispersity of the particles.

From the measurements reported in fig. 4.4, the dispersion in  $d_0^I$  decreases with molarity, thus suggesting that it is related to electrostatics. Different behaviours of different particles in the same solution may arise from the variability in their surface electric charge.

In order to access to the particles surface charge  $\sigma_q$  we made Zeta potential ( $\zeta$ ) measurements at different NaCl concentrations for both sulfate and carboxylated spherical particles.

The determination of the effective charge associated to a given potential  $\zeta$  can be made by different methods depending on the characteristics of the system [118]. Here we use the O'Brien-White-Ohshima method, which is applicable under conditions of small ions and low Zeta potentials ( $\zeta \leq 100$  mV) [118], which are satisfied in our case. Accordingly to this model  $\sigma_q$  results in:

$$\sigma_q = \frac{2\epsilon_0\epsilon k k_B T}{j e} \sinh\left(\frac{j e \zeta}{2 k_B T}\right) \cdot \left[1 + \frac{1}{ka} \frac{2}{\cosh^2(j e \zeta / 4 k_B T)} + \frac{1}{(ka)^2} \frac{8 \ln [\cosh(j e \zeta / 4 k_B T)]}{\sinh^2(j e \zeta / 2 k_B T)}\right]^{1/2} \quad (4.7)$$

<sup>1</sup>Here, and wherever nothing different is specified, molarity is considered in moles per litre.

<sup>2</sup>The Debye screening length, defined by relation 1.11, for monovalent species reduces to:

$$\lambda_D = \sqrt{\frac{k_B T \epsilon \epsilon_0}{2 c L e^2}} \cdot 10^3, \quad (4.6)$$

where  $c$  is the molarity and  $L$  the Avogadro Number.

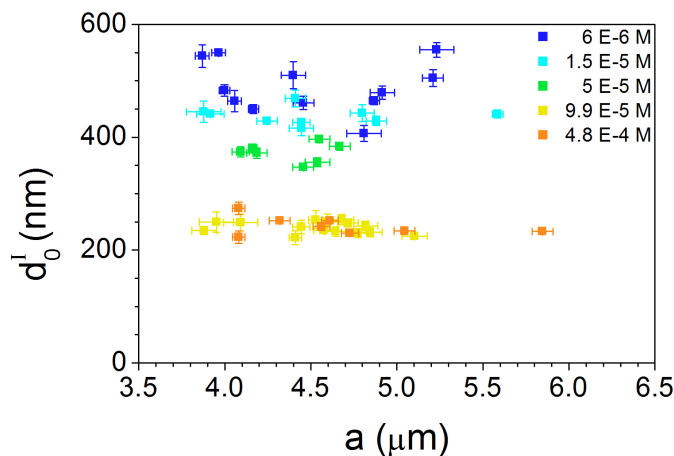


Figure 4.4: Equilibrium positions  $d_0^I$  of sulfate spheres versus particle radius  $a$  for solutions at different NaCl molar concentrations. Molarity increases from blue to red points as listed in the legend.

In the formula  $k = 1/\lambda_D$  and  $j$  is the electrolytes valency<sup>3</sup>. The measurements have been made at different molarities to check that  $\sigma_q$  is not  $k$ -dependent. The surface charge densities obtained for SS and CS are respectively  $\sigma_q = -0.005 \pm 0.001$  C/m<sup>2</sup> and  $\sigma_q = -0.0011 \pm 0.0003$  C/m<sup>2</sup>.

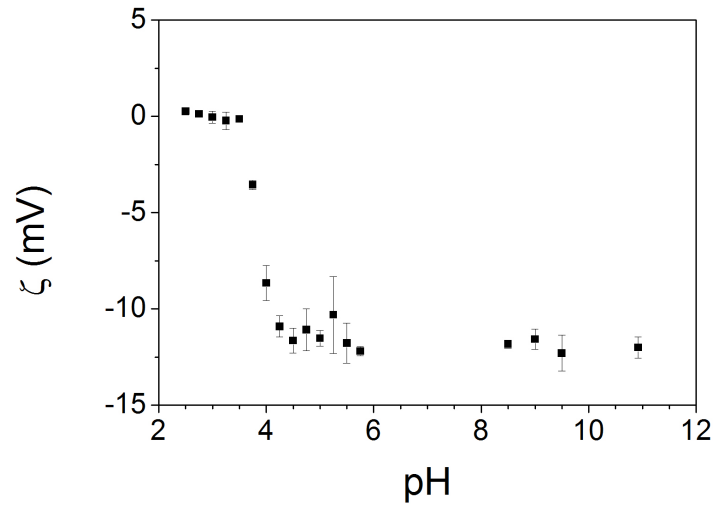
While molarity only affects  $\lambda_D$  without varying  $\sigma_q$ , the pH tuning allows to change the surface charge density of the CS particles. Figure 4.5(a) reports the  $\zeta$  measured for samples at different pH and constant molarity (4 mM). In all the prepared samples, molarity is kept constant while varying the pH by mixing NaCl together with HCl. In figure 4.5(b) the corresponding  $\sigma_q$  obtained from equation 4.7 is reported. Both the Zeta potential and the charge have the same trend: constant zero value at low pH, followed by a fast step descent and then by the stabilization at a constant negative value. The interesting pH region is the one between the values 3.5 and 4.5, where surface charge significantly changes with pH. Unfortunately, no results for  $d_0^I$  are available for solutions at  $\text{pH} < 4$  because at such pH values the particles get directly adsorbed at the air-liquid interface after sedimentation.

## 4.2 Measurements of the unexpected equilibrium

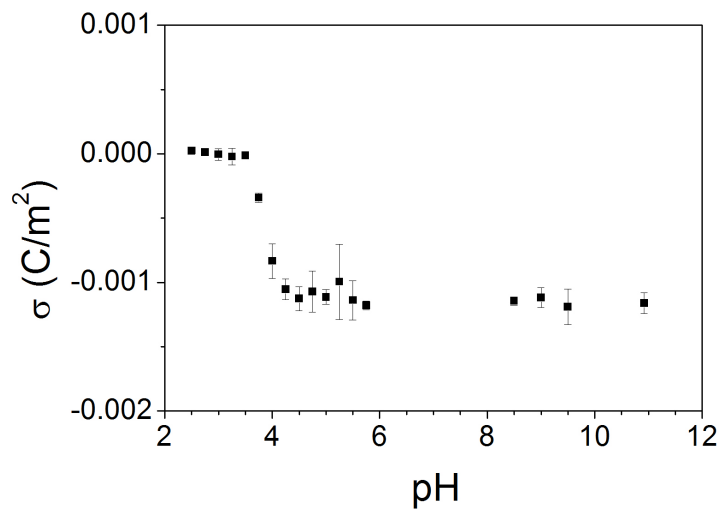
Depending on the solution molarity and on the particle surface charge, a particle may have a second equilibrium distance  $d_0^{II}$  closer than  $d_0^I$  to the air-liquid interface ( $d_0^{II} < d_0^I$ ). In figure 4.6, is reported an example of  $d(t)$  where both equilibrium positions are present: initially  $d$  fluctuates around  $d_0^I$ , then at  $t \simeq 50$  s it jumps to a second equilibrium position  $d_0^{II}$  closer to the interface. The transition is very rapid: it happens in a time interval of 300 ms. The amplitudes of fluctuations around  $d_0^{II}$  are weaker than the ones around  $d_0^I$ .

The energy profiles extracted from the two equilibrium positions of figure 4.6 are reported in figure 4.7. In the figure  $\Delta U^I$  and  $\Delta U^{II}$  refer to the potential wells

<sup>3</sup>The formula 4.7 is valid for  $j : j$  symmetrical electrolytes.



(a)



(b)

**Figure 4.5:** (a) Zeta potential measurements of carboxylated spheres at constant molarity ( $c = 4$  mM) as a function of the pH. (b) Corresponding values of  $\sigma_q$  obtained using eq. 4.7. Both  $\zeta$  and  $\sigma_q$  vary in the interval  $3.5 < \text{pH} < 4.5$  and are constant elsewhere.

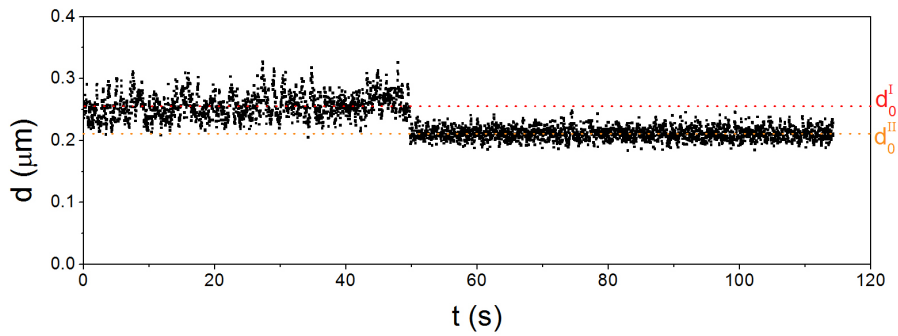


**Figure 4.6:** Typical transition between the first ( $d_0^I$ , on the left) and the second ( $d_0^II$ , on the right) equilibrium position for a sulfate polystyrene sphere of radius  $4.5 \mu\text{m}$  in a water solution of molarity  $c = 4.8 \cdot 10^{-4} \text{ M}$ . The two equilibrium positions are at  $d_0^I = 250 \pm 5 \text{ nm}$  and  $d_0^II = 211 \pm 5 \text{ nm}$ . The transition from  $d_0^I$  to  $d_0^II$  happens in about 300 ms.

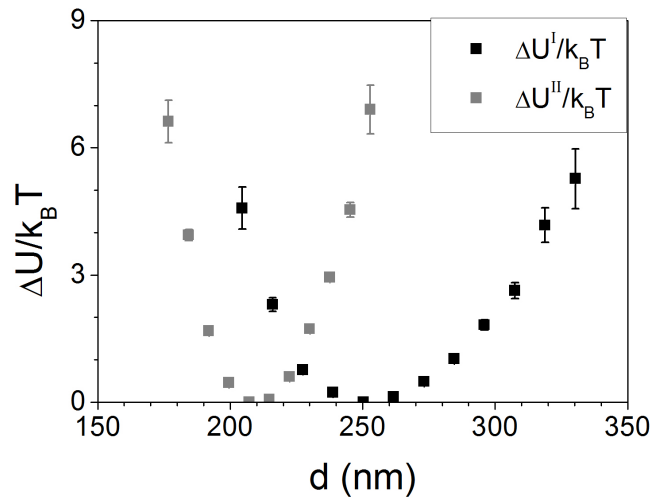


**Figure 4.7:** Plot of  $\Delta U/k_B T$  for the first (black squares) and the second (grey squares) equilibrium positions obtained from  $d(t)$  of figure 4.6 as described in section 4.1. It must be noted that the origin of the energy scale is arbitrary. For this reason the relative heights of the two minima cannot be compared. Dashed lines reproduce the slope of the attractive gravity potential: it can be seen how the attractive right side of the potential well corresponding to  $d_0^II$  is steeper than the gravity potential

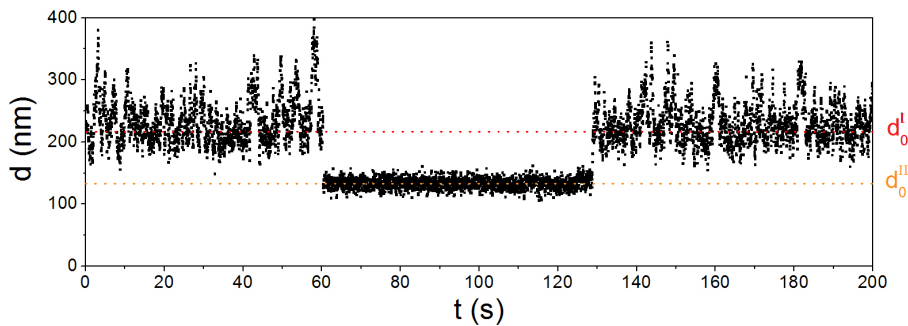


**Figure 4.8:** Example of reversible transition between the two measured equilibrium position. The particle is a sulfate polystyrene sphere of radius  $4.5 \mu\text{m}$  in a water solution of NaCl at  $4.8 \cdot 10^{-4} \text{ M}$ .

around  $d_0^I$  and  $d_0^{II}$  respectively. The second potential well  $\Delta U^{II}$  (grey points) is more symmetric and narrower than the first one  $\Delta U^I$ . Moreover, the two potential wells overlap: surprisingly, for the same values of  $d$  in the range  $200 \text{ nm} < d < 250 \text{ nm}$  there are two possible values of  $U$ , corresponding either to a repulsive or an attractive force acting on the sphere. It must be noted that  $\Delta U^I = U(d) - U(d_0^I)$  and  $\Delta U^{II} = U(d) - U(d_0^{II})$ , where in principle  $U(d_0^I) \neq U(d_0^{II})$ . Hence, it is not possible to infer from such measurements the absolute scale of energy and, in particular, which of the two minima is the deepest one.

The moment of the transition  $d_0^I \rightarrow d_0^{II}$  is very unpredictable: considering different spheres in the same sample, the transition can be very rapid (the sedimenting sphere directly crosses the first potential well), it can occur few seconds or minutes after reaching the first equilibrium position or it can never occur in the experimental time scales<sup>4</sup>. Since the typical recorded videos are 10 minutes long and a typical experiment last few hours, documenting the transition is a rare event. For this reason only for less than the 10% of the measured particles both equilibrium positions has been observed: in all other cases particles stay either in the first or in the second equilibrium position for the whole duration of the recording.

The transition from the second equilibrium back to the first one has also been observed, as shown in figure 4.8, but is a much more rare event (about 1% of observed events). Thus, the transition is reversible and the second equilibrium position seems more stable.

The probability to find a particle in the second equilibrium position increases with the molarity of the solution and it is greater for carboxylated spherical particles. For the sulfate ones the probability goes from zero to almost 100% for molarities ranging from  $c < 10^{-5} \text{ M}$  to  $c = 10^{-3} \text{ M}$ . In the case of carboxylated particles some specimens are at the second equilibrium position for any value of  $c$ , and for  $c \geq 10^{-4} \text{ M}$  it is difficult to find particles in the first equilibrium position after time scales of 100 min.

Figure 4.9 reports for each molarity the value of  $d_0^{II}$  averaged over 5-20 sulfate particles (grey points). For comparison, the average  $d_0^I$  of fig. 4.3(a) are also reported (black points). For identical molarities, second equilibrium positions appear to be systematically 50-100 nm closer to the interface.

<sup>4</sup>In some experiments particles has been found in  $d_0^I$  more than 24 hours after cell preparation.

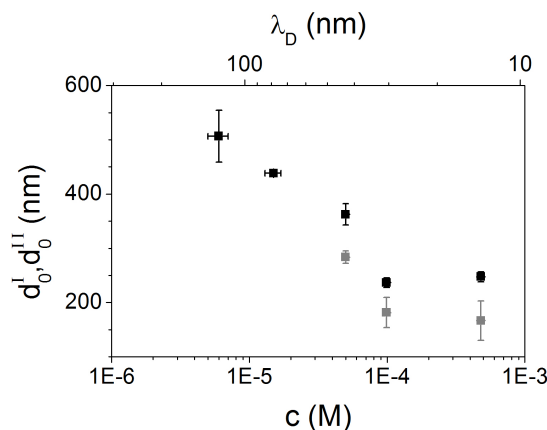


**Figure 4.9:** Plot of the average  $d_0^I$  (grey points) and  $d_0^{II}$  (black points) as a function of molarity for the sulfate spheres. The averages are made over 5-20 particles in solutions at same molarity. Top scale reports the Debye screening length  $\lambda_D$  correspondent to the molarity of the bottom scale.

### 4.3 Interface crossing: data and discussion

After the sedimentation regime a particle can remain in the equilibrium regime and then, from either the first or the second equilibrium position, get adsorbed. We have also observed that the interface crossing can occur right after the sedimentation regime without any measurable equilibrium position. As well as for the transition from  $d_0^I$  to  $d_0^{II}$ , also the probability of the adsorption at the interface depends on solution properties (pH and molarity) and on particle types (SS or CS). Adsorption of sulfate spheres is a very rare event and over more than 250 particles only one time it has been observed. On the contrary, for the carboxylated spheres the adsorption probability can be tuned by changing molarity and pH, as shown in figure 4.10. There, empty circles represent samples for which the particles are trapped at the interface, while full circles represent the ones for which the particles are in one equilibrium close to the interface (observations made at 1 hour elapsed time). Half filled points represent samples where two significant populations (trapped and at an equilibrium position) coexist. Note that the trapping probability increases with the molarity and, for a fixed molarity, with the pH.

In figure 4.11 a sketch of a spherical particle in the interface crossing regime is shown. The contact angle  $\theta'$  is defined as the angle between the air-liquid interface and the wetted surface of the particle as represented in the figure.

As described in chapter 2, a particle trapped at the interface doesn't exhibit interference fringes in its center, due to the absence of a liquid film between the particle and air. However, the  $z$ -tracking is still possible because of interference fringes originating from the still submerged region of the sphere<sup>5</sup>.

Compared to previous works on the interface-breaching dynamics of colloids [14, 101] which needed a calibration looking at the pre-wetting dynamics, our technique allows the precise determination of the contact time between the particle and the interface without needing any assumption on the hydrodynamics close to the interface.

<sup>5</sup>Unfortunately, the tracking program developed in chapter 2 cannot be used in this case as the interference pattern is different (no fringes in the central part). Consequently the pattern is tracked manually.

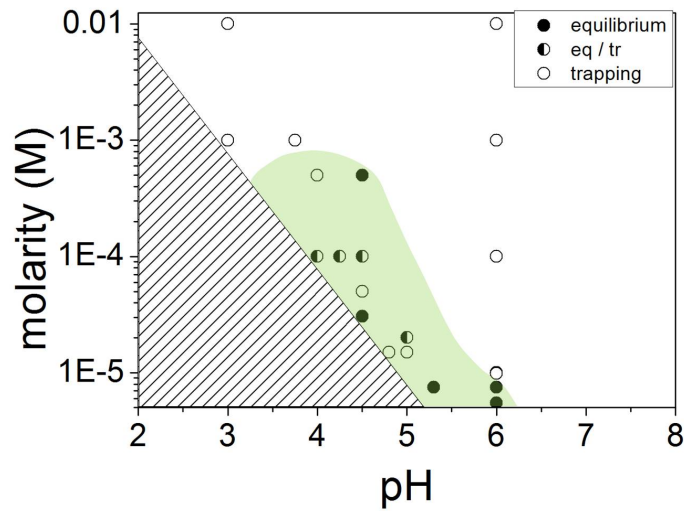


**Figure 4.10:** Diagram of the trapping probability of CS as a function of pH and molarity. Empty and full circles represent samples for which (after 1 hour) most of particles are trapped and at equilibrium respectively. Half filled points represent samples where two consistent populations (trapped and in an equilibrium position) coexist. The hatched region of the plot cannot be explored as the addition of HCl to lower the pH also increases the molarity. The green color highlights the region close to the border of the hatched region where the equilibrium regime as been observed.

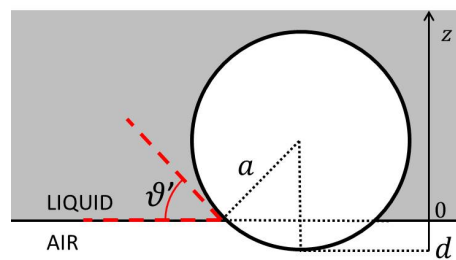
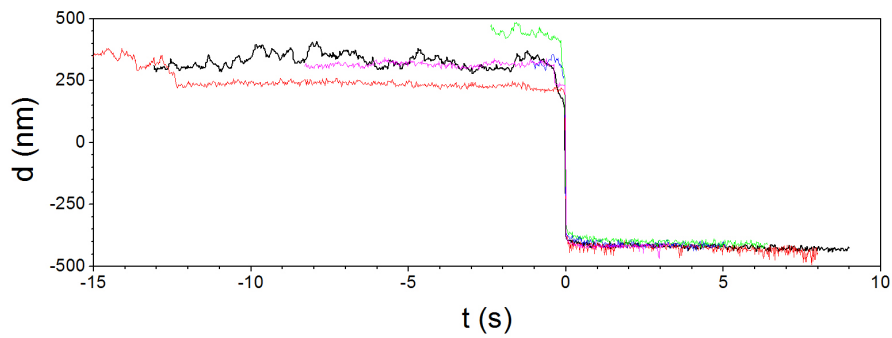
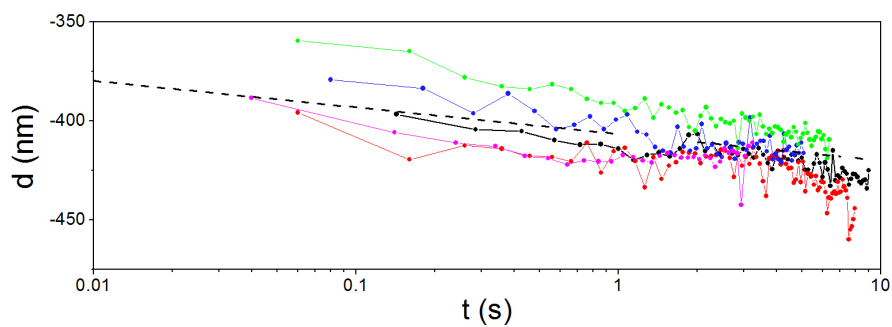


**Figure 4.11:** Sketch representing the contact angle  $\theta'$ . It can be obtained from the particle radius  $a$  and measuring  $d$  as  $\theta' = \arccos\left(\frac{a+d}{a}\right)$ . Note that  $d$  in this case is negative.



(a)



(b)

**Figure 4.12:** (a) Interface crossing dynamics of 5 different CS particles in solutions whose parameters are reported in table 4.1. Particles represented in black, blue and green directly cross the interface from  $d_0^I$ , while the ones represented in red and magenta first pass from  $d_0^{II}$  (for the red one it is also possible to see the transition  $d_0^I \rightarrow d_0^{II}$ ). For each particle  $t = 0$  has been chosen as the time corresponding to interface breaching. (b) Semi-Log representation of data in (a) after interface breaching ( $t > 0$ ). In dashed line is reported the average of fits made with eq. 1.61 over the five  $d(t)$ .

particle (referred to fig. 4.12)	$c$ (M)	pH	defect area (nm <sup>2</sup> )
black	$1.5 \cdot 10^{-5}$	5	79
red	$5 \cdot 10^{-5}$	4.5	85
blue	$1.5 \cdot 10^{-5}$	4.8	58
green	$1.5 \cdot 10^{-5}$	4.8	46
magenta	$1.5 \cdot 10^{-5}$	4.8	159

**Table 4.1:** Defect areas of CS obtained fitting the data in fig. 4.12(b) with eq. 1.61.

In figure 4.12 data of interface crossing for different CS particles are reported. Each particle starts from a different equilibrium position, either  $d_0^I$  (black, blue and green) or  $d_0^{II}$  (red and magenta), corresponding to positive  $d$  values, and attaches to the interface. Negative values of  $d$  means the particle has crossed the interface. In the plot the after-breaching data are reported only for the first ten seconds, but the dynamics observed at larger times is the same. It is noteworthy that all particles fluctuates dissimilarly and have different equilibrium distances when they are totally in the fluid, while they behave in the same fashion after interface breaching. This happens either for particles in same conditions (blue and green, suspended in solutions with same molarity and pH, and both in  $d_0^I$ ) and for particles at different equilibrium positions (black, blue and green at  $d_0^I$  and red and magenta at  $d_0^{II}$ ) and/or in different solutions ( $c = 5 \cdot 10^{-5}$  for the red and  $c = 1.5 \cdot 10^{-5}$  for the others). This proves the irrelevance of the particle-interface interaction determining the equilibrium position once the particle touches the interface.

The initial transition of the interface crossing is faster than the acquisition time step between two frames and cannot be resolved until the dewetting process slows down the motion. It starts to be time-resolved from contact angles of about  $24^\circ$ .

In figure 4.12(b) the after interface-breaching dynamics ( $t > 0$ ) of fig.4.12(a) is represented in semi-Log scale. It appears to be a slow logarithmic dynamics, in agreement with what Kaz *et al.* [14] described for spherical particles breaching an oil-water interface (section 1.5).

Because of the analogy with their case, we analyzed our measured dynamics considering their model describing activated hopping of the contact line over nanoscale surface heterogeneities of the particle. From the fit with equation 1.61 of the data reported in fig. 4.12(b) we obtained the defect areas  $A$  reported in table 4.1. They are larger of the ones found by Kaz *et al.*, even if of the same order of magnitude. This fact is not surprising as it is reasonable that the defect areas depend on the particles coating. We find an average value of  $A$  equal to  $90 \pm 40$  nm<sup>2</sup>, while on the other side the surface charge of the CS corresponds to an average area per charge of  $150 \pm 40$  nm<sup>2</sup>. The defect and the charge areas are thus comparable, supporting the idea that the nanometric surface heterogeneities are due to the discrete charges present at the surface.

From the data we find that the equilibrium receding contact angle  $\theta'$  is lower than  $30^\circ$  (we do not know the precise value as the slow dewetting dynamics can last months [14]), much lower than what literature reports for polystyrene beads at air-water interfaces [119, 120]. The lower value of the receding contact angle means that the carboxyle coating of the beads plays a decisive role in its determination, probably because of the significant large measured defect area. As a matter of fact, larger is the distance between two defects, more difficult is the contact line hopping between them.

## 4.4 Modelling and discussion of the interaction potential

The measured particle-interface potential energies have been compared to a model which takes into account gravity, van der Waals and double-layers interactions.

Gravity potential arises from the effective mass of the spherical particle:

$$m^* = 4\pi a^3 (\rho_{col} - \rho_1) / 3, \quad (4.8)$$

being  $\rho_{col}$  and  $\rho_1$  the densities of the particle and of the solution respectively. Gravity drives the particle towards the interface in order to minimize the energy  $U_g$ :

$$U_g = m^* g d \quad (4.9)$$

The van der Waals interaction is instead modelled using the exact expression for the plane-sphere case reported in section 1.1.4:

$$U_{VdW} = \frac{A_H}{6} \left[ \frac{a}{d} + \frac{a}{d+2a} + \ln \left( \frac{d}{d+2a} \right) \right] \quad (4.10)$$

The Hamaker constant  $A_H$  is defined using the convention of positive values for repulsive van der Waals interactions.

In order to experimentally determine  $A_H$ , we consider data relative to high molarity samples ( $4.8 \cdot 10^{-4}$  M) for which the electrostatics is expected to give negligible contributions<sup>6</sup>. For these samples we compare the equilibrium position of the potential given by  $U_g + U_{VdW}$  to the measured<sup>7</sup>  $d_0^I$ .

The value of the Hamaker constant found with this method is  $A_H = 2.0 \pm 0.4 \cdot 10^{-20}$  J, greater by 27% than tabulated value of  $1.57 \cdot 10^{-20}$  J [121] for polystyrene-water-air systems. The agreement is quite good considering that surface groups can change the effective Hamaker constant [16]. The determined  $A_H$  can be considered independent from molarity in the range of ions concentration used in the experiment [122].

The sum of van der Waals interaction and gravity potential is plotted in figure 4.13 versus  $d$  for a polystyrene sphere of radius  $4.5 \mu\text{m}$ . The resulting potential energy has a minimum at  $d = 260$  nm, in the range of the measured equilibrium positions. Such potential is incompatible with the observed crossing of the interface because of the large van der Waals repulsion. Since both the particle and the air-liquid interface are negatively charged (sections 4.1 and 1.1.3), a third contribution to the potential arises from the interaction of their double-layers. Its decisive role in particle trapping is experimentally proved by the molar dependency of the trapping probability (sec. 4.3). In order to introduce the possibility of interface crossing, an attractive contribution is needed, in contrast with the expected repulsive double-layers interaction. Looking more deeply into the problem, if the two objects have different electric boundary conditions, namely one with fixed surface charge and the other

<sup>6</sup>We then verified the validity of this assumption once the fit of the total potential was made including the double layer interaction (section 4.4.1).

<sup>7</sup>We only consider  $d_0^I$  because is the one whose potential well can be successfully compared with  $U_g + U_{VdW}$ . As it will be detailed in section 4.4.3,  $\Delta U^H$  is incompatible with a potential having gravity as the only long-range attractive force.

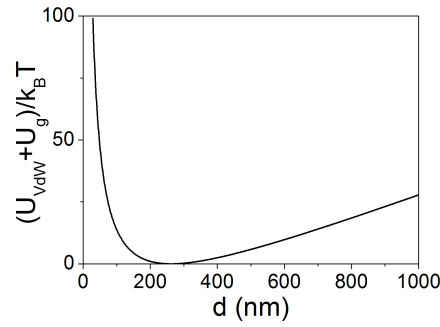


**Figure 4.13:** Gravity (eq. 4.9) plus van der Waals (eq. 4.10) potential acting on a spherical polystyrene particle of radius  $4.5 \mu\text{m}$  versus  $d$ . The used Hamaker constant is  $A_H = 2 \cdot 10^{-20}$  J. The potential has a minimum at  $d = 260$  nm.

with fixed surface potential, an attractive interaction may emerge when the two objects are closer together (see sec. 1.1.2). These considerations drove Del Castillo *et al.* [5] to include such boundary conditions in a model describing the interaction between an air-liquid interface and a dielectric solid wall.

We therefore consider the double-layers interaction between a sphere with fixed charge  $\sigma_q$  and a plane with fixed potential  $\psi_{AL}$ . We use equation 1.19 describing two spheres with dissimilar electric boundary conditions in the limit where one of the two radii goes to infinite. It results in:

$$U_{DL}^{\psi-\sigma} = \pi a \left[ \frac{2\psi_{AL}\sigma_q}{k} \left( \frac{\pi}{2} - \arctan \sinh(kd) \right) - \left( \frac{\sigma_q^2}{k^2 \epsilon \epsilon_0} - \psi_{AL}^2 \epsilon \epsilon_0 \right) \ln \left( 1 + e^{-2kd} \right) \right] \quad (4.11)$$

Please note that expression 4.11 has been obtained using Derjaguin and Debye-Hückel approximations (sec. 1.1). While Derjaguin limit ( $ka \gg 1$  and  $d \ll a$ ) in our case is verified<sup>8</sup>, the condition for PB equation linearization ( $e\psi/k_B T \ll 1$ ) is poorly satisfied as for SS and CS particles we have that  $e\psi/k_B T \sim 39$  and  $8.6$  respectively. At first sight, thus, the relation 4.11 is not valid in our case. However, numerical calculations shown that, in the limit of  $ka \gg 1$  and for  $kd > 1$ , the expression 4.11 overlaps with the exact numerical solution [123]. As in our experiments  $ka > 20$  and  $kd > 5$ , we can thus safely use relation 4.11 to fit the data.

To complete the model, an important question that must be addressed is whether the motion of the interface due to evaporation alters the particle-interface interaction. Since the velocity of the interface is practically constant (sec. 3.2.2), the air-liquid interface is an inertial system. In this reference system water velocity at an infinite distance from the interface is

$$\vec{v}_{\text{inf}} = -v_{ev} \hat{z} \quad (4.12)$$

<sup>8</sup>In the present system  $ka \geq 20$  and  $d/a \leq 0.1$ .

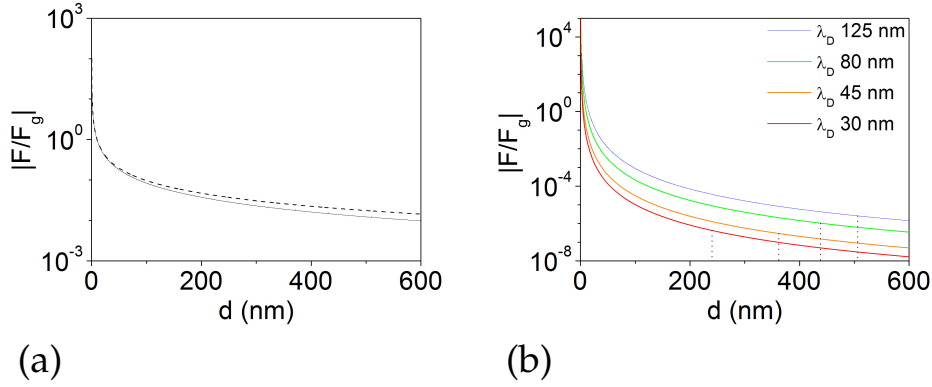


**Figure 4.14:** (a) Scaled amplitude (with gravity) of the diffusive force arising from  $\delta_z \xi_z$  versus  $d$  for a  $4.5 \mu\text{m}$  polystyrene sphere. Continuous (dashed) line correspond to slip (no-slip) hydrodynamic boundary conditions on the air-liquid interface. (b) Scaled amplitude (with gravity) of the electrokinetic lift force versus  $d$  for the same particle and for different debye lengths. Dotted lines indicates the average distances measured from the data at same molarities.

Since the flux is due to the evaporation of a volume of water, the interface can be considered a planar hydrodynamic sink and therefore such flow field is not affected by the interface boundary conditions. Close to the particle the fluid's velocity field will therefore be the one in the laboratory reference system plus a net flow at  $-v_{ev}\hat{z}$  pushing the particle towards the interface. Accordingly, the resulting additional force exerted on the particle results in:

$$F_{ev} = -6\pi\eta av_{ev}\hat{z} \quad (4.13)$$

Approximating the measured potential well with an harmonic potential characterized by an effective elastic constant  $\tilde{k}$ , the additional force along  $z$  will cause a deviation  $\Delta d$  from  $d_0$  given by:

$$\Delta d = -6\pi\eta av_{ev}/\tilde{k} \quad (4.14)$$

Considering  $\tilde{k} = 3 \cdot 10^{-6} \text{ N/m}$  (as obtained from typical measurements) and considering the measured interface velocity  $v_{ev} = 0.05 \mu\text{m/s}$ , from relation 4.14 we obtain  $\Delta d \simeq 1 \text{ nm}$ . Such nanometric value is at the detection limit of our setup. For completeness, the correspondent potential  $U_{ev} = 6\pi\eta av_{ev}d$  has been included in the gravity potential  $U_g$  in order to group together all the linear terms of the total potential.

### Negligible contributions

Beside the contributions discussed, different phenomena occur close to an air-liquid interface which can in principle alter the particle-interface interaction. The *hydrodynamic lift* force due to the motion parallel to the interface can be neglected. Considering equation 1.45, indeed, in our case  $Re_a \sim Re_z < 10^{-3}$ , thus implying an hydrodynamic lift absolutely negligible on the typical scales of  $v_{\parallel} < 10^{-4} \text{ m/s}$ . Moreover, Brownian diffusion and electrokinetics also may cause additional forces, both acting

on the particle in the direction perpendicular to the interface (see chapter 1). *Brownian diffusion* in presence of a gradient of drag predicts a second non dissipative term in the expression for the friction force which drives the particle in the direction of decreasing  $\xi$  (sec. 1.3.1), which in our case is the normal to the interface. In figure 4.14(a) a plot of the amplitude of this force is reported for a particles of radius  $4.5 \mu\text{m}$ . It is evaluated using eq. 1.47 and scaled by gravity force modulus  $F_g$ . The evaluation of the normal drag ( $\xi_{\perp}$ ) and of its gradient along  $z$  ( $\partial_z \xi_{\perp}$ ) are made using the described theory for the drag for both slip (continuous line) and no-slip (dashed line) hydrodynamic boundary conditions (sec. 1.2). In the interval of observed equilibrium distances ( $240 - 500 \text{ nm}$ ) the modulus of the diffusive force term ranges between  $3 \cdot 10^{-2} F_g$  and  $10^{-2} F_g$  for slip boundary conditions and between  $4 \cdot 10^{-2} F_g$  and  $2 \cdot 10^{-2} F_g$  for the no-slip ones. Its contribution is negligible.

*Electrokinetic lift* has been evaluated using eq. 1.52 for a  $4.5 \mu\text{m}$  radius sphere with a surface charge of  $-0.005 \text{ C/m}^2$  which moves parallel to the interface. Particle's velocity is chosen as the maximum measured drift ( $0.5 \mu\text{m/s}$ ) in order to evaluate the limiting case with the bigger electrokinetic lift force. For the same reason we consider no-slip hydrodynamic boundary conditions, in order to have the maximum relative motion between the particle and the interface. Figure 4.14(b) represents the obtained predictions for Debye lengths equal to:  $125 \text{ nm}$  (blue line),  $80 \text{ nm}$  (green),  $45 \text{ nm}$  (orange) and  $30 \text{ nm}$  (red). The experimental mean distances correspondent to these Debye lengths have been highlighted with the dotted lines. At small distances electrokinetic lift force has a relevant contribution, reaching very high values for nanometric distances from the interface. However, increasing  $d$  the contribution strongly decrease and for all the considered Debye lengths it is negligible at the typical equilibrium distances.

#### 4.4.1 Total potential energy model

Considering the described contributions, the particle potential  $U_{tot}$  results in:

$$U_{tot} = U_{VdW} + U_{DL}^{\psi-\sigma} + U_g \quad (4.15)$$

In order to discuss the importance of the double-layers potential, in figure 4.15(a) are compared the sum of gravity and van der Waals potentials and the total potential given by eq. 4.15. Because of van der Waals repulsion both potentials positively diverge for  $d \rightarrow 0$ . Unlike  $U_{VdW} + U_g$ , however,  $U_{tot}$  presents two minima. A first one at large  $d$  (hundreds of nm), close to the one determined by  $U_{VdW} + U_g$ , and a second one (not shown in the figure) very close to the interface ( $d < 1 \text{ nm}$ ). An energy barrier of few  $k_B T$  separates the first relative minimum from the much deeper second absolute minimum. The energy barrier divides attractive from repulsive  $U_{DL}^{\psi-\sigma}$  1.1.2. The absolute minimum at  $d < 1 \text{ nm}$  must not be confused with the  $\Delta U^{\text{II}}$  described in section 4.2 whose equilibrium position  $d_0^{\text{II}}$  is measured at hundreds of nanometers from the air-liquid interface. The presence of an equilibrium position at less than 1 nm from the liquid surface is extremely difficult to observe experimentally as any kind of fluctuation (evaporation of few water layers, air-bridge between interface and gas-bubbles in the liquid, capillary waves, ...) can cause contact between the particle and the interface inducing the interface breaching. Moreover, at such short-range distances, the Hamaker constant does not necessarily have the same value it has at large distances as for nanometric  $d$  particle's coating play a major role in determining it [16]. Finally, short-range attractive hydrophobic interactions are known to be also determinant as in many situations they have been supposed to be the responsible of the interface breaching of the particle [3].

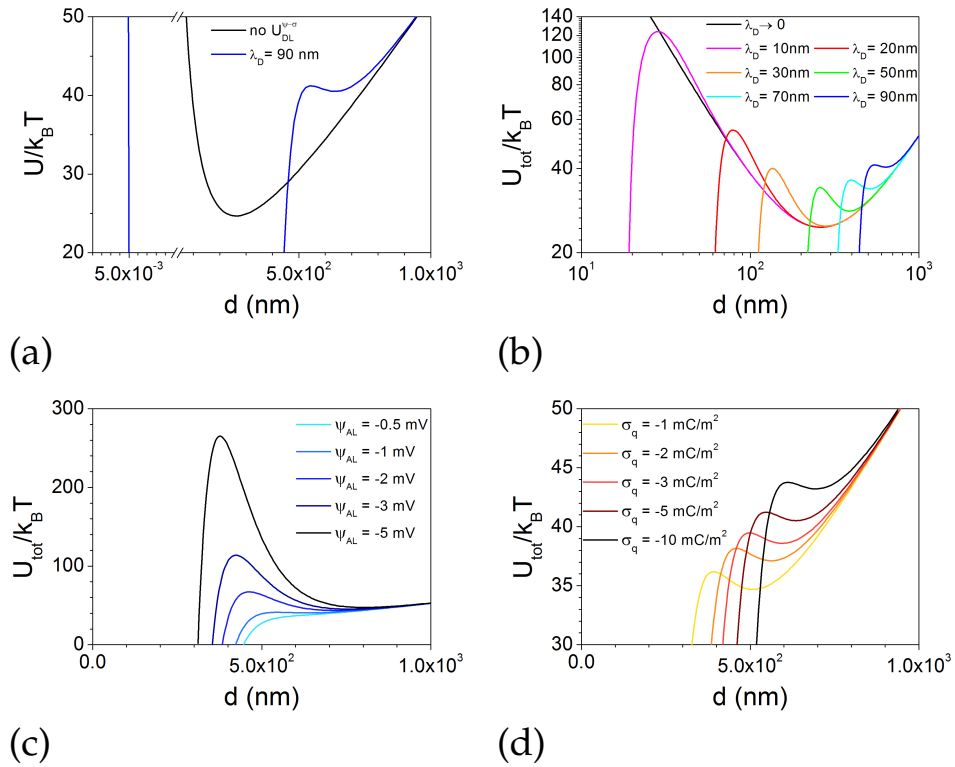


**Figure 4.15:** Plots of  $U_{tot}$  versus  $d$  for a polystyrene sphere of radius  $a = 4.5 \mu\text{m}$  varying potential parameters. (a) Comparison between the potential energy  $U_{VdW} + U_g$  (black) and  $U_{tot}$  (blue) for  $\lambda_D = 90 \text{ nm}$ ,  $\sigma_q = -5 \text{ mC/m}^2$  and  $\psi_{AL} = -1 \text{ mV}$ . (b)  $U_{tot}$  dependency from  $\lambda_D$  fixing  $\sigma_q = -5 \text{ mC/m}^2$  and  $\psi_{AL} = -1 \text{ mV}$ . (c)  $U_{tot}$  dependency from  $\psi_{AL}$  fixing  $\sigma_q = -5 \text{ mC/m}^2$  and  $\lambda_D = 90 \text{ nm}$ . (d)  $U_{tot}$  dependency from  $\sigma_q$  fixing  $\psi_{AL} = -1 \text{ mV}$  and  $\lambda_D = 90 \text{ nm}$ .

The  $\lambda_D$  dependency of  $U_{tot}$  can be seen in 4.15(b), where the Debye length is varied in the range of its experimental values. The relative minimum approaches the interface as  $\lambda_D$  decreases, until it reaches its lower limit in correspondence of the minimum of  $U_{vdW} + U_g$ . Such dependence of the relative minimum position from  $\lambda_D$  has the same trend of the experimental  $d_0^I$  (fig. 4.3). At the same time, as  $\lambda_D$  decreases the potential barrier separating attractive from repulsive  $U_{DL}^{\psi-\sigma}$  increases and its position approaches to the interface, until in the limit case of  $\lambda_D \rightarrow 0$  (black line) the potential energy positively diverges for  $d \rightarrow 0$  and we get back purely van der Waals repulsion. This implies that the crossing of the energy barrier should be easier at low molarities, in contrast with experimental observations. Such discrepancy may be due to the existence of the unpredicted second equilibrium position in  $d_0^{II}$ , as discussed in section 4.4.3.

In figure 4.15(c) the potential energy is reported varying  $\psi_{AL}$  close to the fitted values reported in section 4.4.2. The air-liquid interface potential affects  $U_{tot}$  mainly by varying the height of the potential barrier: the latter decreases with  $\psi_{AL}$  until disappears (in fig. 4.15(c) it happens for  $\psi_{AL} = -0.5$  mV).

Finally, the influence of particle surface charge density is reported in fig. 4.15(d), where  $U_{tot}$  is represented for values of  $\sigma_q$  in the range between the one corresponding to SS and the one of CS particles. As  $\sigma_q$  approaches zero, the relative minimum approaches the air-liquid interface.

#### 4.4.2 Fit of the potential energy around the first equilibrium position

The measured  $\Delta U^I$  are fitted using eq. 4.15 with fitting parameters  $a$ ,  $\lambda_D$ ,  $\psi_{AL}$  and an additive  $U_0$  offset. Solution's density and viscosity are obtained from tabulated data knowing  $c$  and  $T$  and are kept fixed in the fit.

Figure 4.16 reports examples of the result of the fits made for three different sulfate spheres in NaCl solutions with  $c = 1 \cdot 10^{-5}$  M (squares),  $c = 5 \cdot 10^{-5}$  M (circles) and  $c = 5 \cdot 10^{-4}$  M (triangles). For each data set the corresponding fit (black lines) is superimposed to the points.

The agreement between model and data is good with a confidence higher than 95%. Fits made using instead a model for the double-layers interaction  $U^{\sigma-\sigma}$  with boundaries of constant charge on both the objects give similar results but with a lower confidence level. In figure 4.17(a) the ratio between the best fitting radii  $a_{fit}$  found for sulfate spheres and the corresponding radii  $a_{meas}$  measured from particle's bright field image are given as a function of  $a_{meas}$ . Similarly, in fig. 4.17(b) the ratio between the best fitting Debye lengths  $\lambda_{D,fit}$  found for sulfate spheres and the corresponding expected values  $\lambda_{D,exp}$  known from sample's molarity are given as a function of  $\lambda_{D,exp}$ . The found values for the radii are on average greater by a factor 1.09 than the measured ones. Small variations of the radius affect the potential mostly on its attractive side, where gravity potential dominates: fits made fixing  $a = a_{meas}$ , indeed, returns same values of  $\psi_{AL}$  and  $\lambda_D$ . In this case, however, the fit confidence level reduces due to the discrepancy with the data on the attractive side of the potential.

The fitted values of  $\lambda_D$  are lower than the expected ones by a factor dependent on  $\lambda_D$ : decreasing the molarity the ratio  $\lambda_{D,fit}/\lambda_{D,exp}$  goes from 0.9 to 0.6. Debye screening length is defined for linearized PB equation [81] (see section 1.1); because of the high value of  $e\psi/k_B T$  in our system,  $\lambda_D$  is therefore not well defined. This can explain the observed discrepancy between the Debye length calculated from experimental  $c$  and the one obtained from the fit. This explanation is supported by the

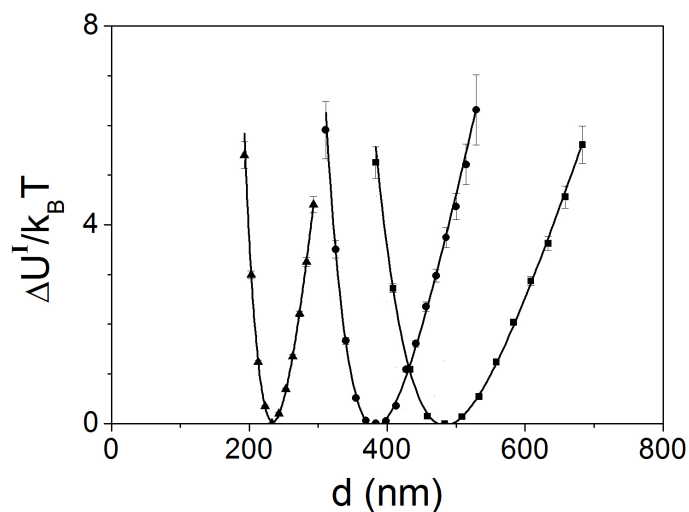


**Figure 4.16:** Examples of data (points) of  $\Delta U^I$  and relative best fits (lines) made with eq. 4.15. Data corresponds to three sulfate spheres in solutions at different molarity:  $a = 5.84 \mu\text{m}$  in a  $5 \cdot 10^{-4}$  M solution (triangles),  $a = 4.92 \mu\text{m}$  in a  $5 \cdot 10^{-5}$  M solution (circles) and  $a = 4.25 \mu\text{m}$  in a  $1 \cdot 10^{-5}$  M solution (squares).

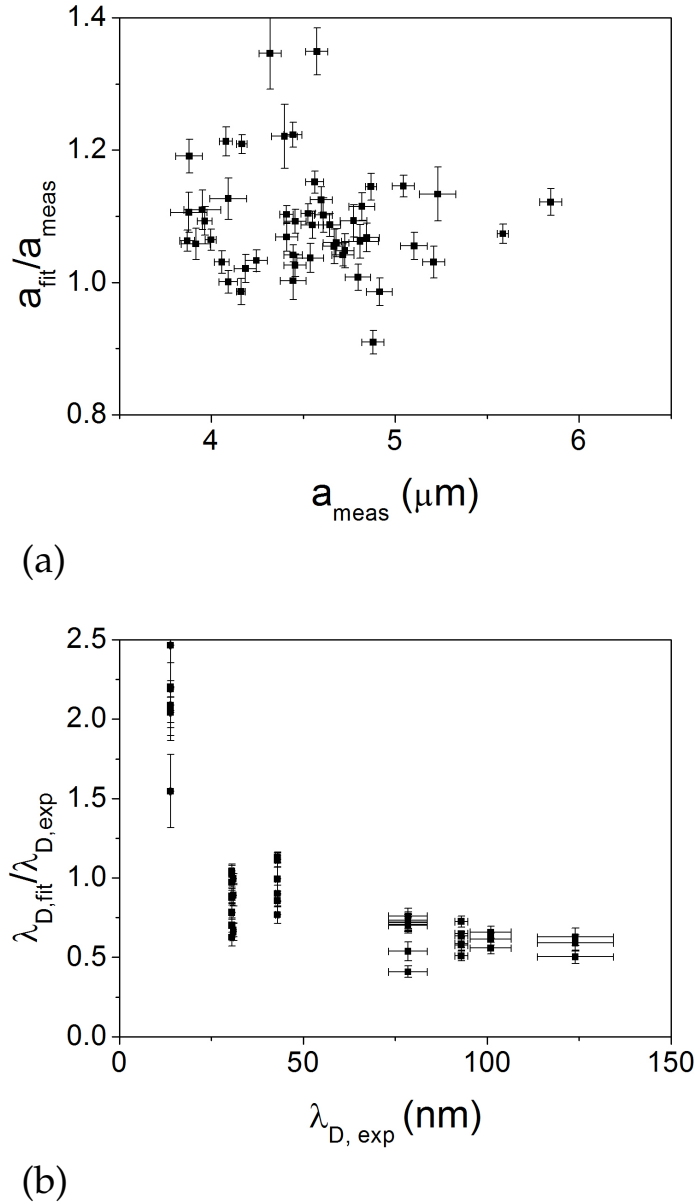
better agreement observed at high molarities, when the error made linearizing PB is lower.

Figure 4.18 reports for CS the same ratios ( $a_{fit}/a_{meas}$  (a) and  $\lambda_{D,fit}/\lambda_{D,exp}$  (b)) as in fig. 4.17. The trends are the same as the ones of SS for both the radius and the Debye length.

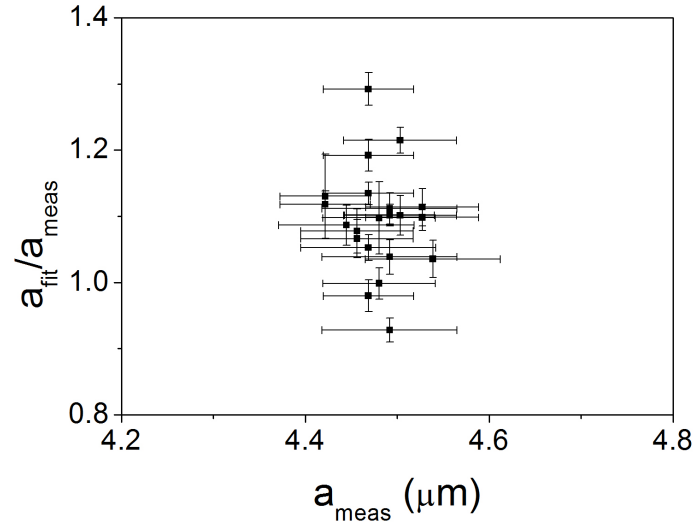
The best fit values of  $\psi_{AL}$  found for SS and the CS have an average value of  $-1.3 \pm 0.2$  mV and  $-1.1 \pm 0.2$  mV respectively. The averages are made over all the single-particle best fit values found for molarities  $\leq 10^{-4}$  M, for which the electrostatics carries significant contributions to  $U_{tot}$ . The air-liquid surface potentials found for the two set of sphere are the same within the error bar: as expected  $\psi_{AL}$  is independent from the particle. Moreover, no significant dependence from the molarity has been observed. As reported in section 1.1.3, measurements of air-water potential given in literature range in a very wide interval from  $-10^{-1}$  mV up to  $-10^2$  mV, even if most of them attest between  $-10$  mV and  $-80$  mV. Interestingly, both in our case and in the previous works where data are analyzed with models involving constant-potential boundary conditions [4, 5], the found  $\psi_{AL}$  has a modulus lower than what previously reported in literature. This highlights the importance of the choice of the electric boundary conditions for the determination of the potential of the air-water interface.

#### 4.4.3 Possible origins of the second equilibrium position

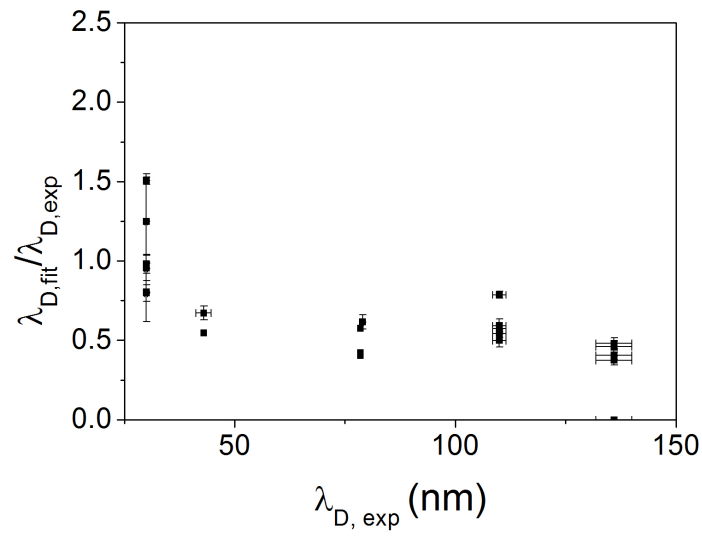
The second equilibrium position is not predicted by the total potential of eq. 4.15. We saw that  $\Delta U^{II}$  cannot be fitted with eq. 4.15, even if we drastically change the electric boundary conditions (positive interface potentials and/or particle's surface charge). Such results demand to consider new physical phenomena. Our hypothesis is that the presence of nano-bubbles pinned on particle's surface can alter the



**Figure 4.17:** Sulfate spheres: (a) Ratio  $a_{fit}/a_{meas}$  between the particle radius  $a_{fit}$  obtained from the fit of  $\Delta U^I$  and the corresponding one  $a_{meas}$  measured from the particle's bright field image versus  $a_{meas}$ . (b) Ratio  $\lambda_{D,fit}/\lambda_{D,exp}$  between the Debye screening length  $\lambda_{D,fit}$  obtained from the fit of  $\Delta U^I$  and the corresponding expected one  $\lambda_{D,exp}$  calculated from the solution's molarity  $\lambda_{D,exp}$ .



(a)



(b)

**Figure 4.18:** Carboxylated spheres: (a) Ratio  $a_{fit}/a_{meas}$  between the particle radius  $a_{fit}$  obtained from the fit of  $\Delta U^I$  and the corresponding one  $a_{meas}$  measured from the particle's bright field image versus  $a_{meas}$ . (b) Ratio  $\lambda_{D,fit}/\lambda_{D,exp}$  between the Debye screening length  $\lambda_{D,fit}$  obtained from the fit of  $\Delta U^I$  and the corresponding expected one  $\lambda_{D,exp}$  calculated from the solution's molarity  $\lambda_{D,exp}$ .

particle-interface interaction making it dependent from particle's orientation. In this section are summarised the arguments which drive us to formulate such hypothesis.

In literature, among the works dealing with similar physical systems no one reports the existence of a second equilibrium position. Only in one case TIRM measurements of spherical particles close to water-oil interface shown a dynamics very similar to our data for the transition from  $d_0^I$  to  $d_0^{II}$  [8]. However, TIRM is unable to detect the absolute particle-interface distance and the authors interpreted the data as the trapping of the particle at the interface.

The fact that in our data both the transitions, from  $d_0^I$  to  $d_0^{II}$  and from an equilibrium position to the interface, are more probable at high molarities - although crossing probability should decrease because of the larger energy barrier - suggests that the two phenomena have a common origin. It is possible that the rising of the second equilibrium is responsible of the interface crossing events.

The reversibility of the transition  $d_0^I \rightleftharpoons d_0^{II}$  (fig. 4.8) excludes irreversible phenomena like surface pollution as possible origin of the appearance of the second equilibrium position. The conservative character of the transition is also confirmed by the analysis of the potentials of fig. 4.8: the fit of  $\Delta U^I$  made over the data recorded either before and after the time interval spent in  $d_0^{II}$  returns the same best fit parameters, thus implying that the potential is not changed.

### Other possible interactions

The transition from  $\Delta U^I$  to  $\Delta U^{II}$  could be caused by an additional attractive force which activates at a given time adding its contribution to the total interaction. This hypothesis is supported by the observations of the shapes of the potential wells (fig. 4.7), as the slope of the repulsive part of the potential (on the left of  $d_0$ ) remains similar for both  $\Delta U^I$  and  $\Delta U^{II}$  while the slope of the attractive part (on the right of  $d_0$ ) is much more pronounced for  $\Delta U^{II}$  than for  $\Delta U^I$  and cannot be explained only with gravity. Furthermore, the additional attraction we are looking for should increase with molarity, in order to justify the increasing of the probability of the  $d_0^I \rightleftharpoons d_0^{II}$  transition as  $\lambda_D$  decreases (fig. 4.10).

Here is given a brief review of the effects that have not been considered in eq. 4.15 which can in principle alter the interaction.

The PB equation is obtained in the mean field hypothesis. Such hypothesis impedes the prediction of *ionic correlation*, a phenomenon described by more general theories which can introduce additional equilibrium positions originated from charge inversions. Charge inversion consists of binding excess counterions to a charged particle so that its net charge changes sign [124, 125]. This mechanism has been however predicted only in the case of multivalent ions at high concentrations. Sodium chloride's and hydrochloric acid's monovalent ions used in this study cannot therefore produce such effect. On the other side other possible ions dissolved in the solution from air and from glass cell walls have a concentration too low (see sec. 3.1.3) to provoke charge inversion.

A second class of effects that can alter the particle-interface interaction are the external influences. In this class are included interfacial phenomena whose effects propagates in the bulk, as evaporation and capillary waves. The additional force associated to the net flux of water generated by evaporation which pushes the particle towards the interface has been already evaluated in section 3.2.2 and cannot justify the insurgence of the second equilibrium position. On the other side, as already mentioned by Benavides-Parra *et al.* (2016) for a similar setup [11], it is not necessary to consider the contribution of *capillary waves* because for our experimental conditions they have negligible amplitude (few ångstroms [126]).

An external perturbation altering the particle-interface interaction could be the *approaching of other particles* to the one we are measuring. Such perturbation could also justify the time dependence and the reversibility of the transition from  $d_0^I$  to  $d_0^{II}$ . We always check that only one particle is present in the field of view of the camera (50x50  $\mu\text{m}$ ). Nevertheless, we can not *a priori* exclude the passage of a second particle at 50  $\mu\text{m}$  or more from the one we are measuring. In order to evaluate this effect we analyzed the particle-interface potential energy of couples of CS diffusing at a distance of few microns in the  $xy$  plane and fluctuating around either  $d_0^I$  or  $d_0^{II}$  along  $z$ . A significant influence on the particle-interface interaction due to the presence of a second particle has been observed only in the case of a gap distance between the two particles  $\leq 1 \mu\text{m}$ . For larger distances any difference from the case of isolated particles is detected. We can thus exclude also the contribution of particles outside the camera's field of view.

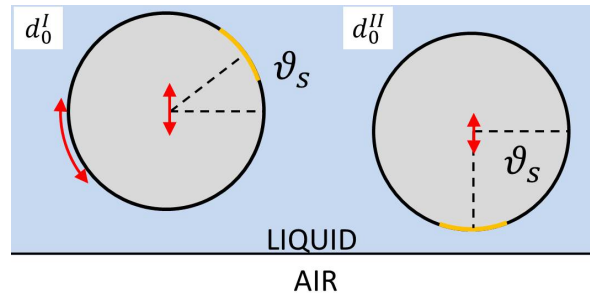
### Temporal dependence of the transition

The overlapping of  $\Delta U^I$  and  $\Delta U^{II}$  reported in fig. 4.7 can be only explained with a sudden time evolution of the potential. However, none of the possible additional interactions we considered can justify the additional attraction found in  $\Delta U^{II}$  or can explain the temporal evolution of the potential. Still, another possibility is to consider an implicit time dependence of the potential energy: the existence of two different values of the potential for the same particle-interface distance can be explained by admitting that  $U$  is not only a function of  $d$  but at least of a second variable which varies in time. A reasonable candidate is the sphere's tilt angle  $\theta_s$ , which, as  $d$ , evolves in time due to thermal agitation. The potential  $U(d, \theta_s)$  can therefore exhibit different profiles in  $d$  for different values of  $\theta_s$ , corresponding to the two observed equilibrium positions.

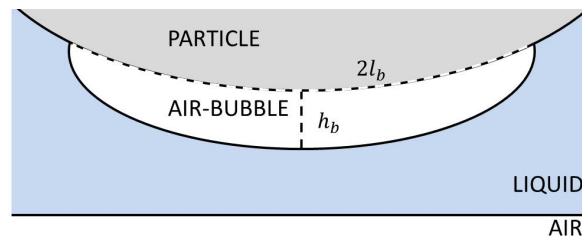
Considering the low value of the ratio  $d/a$  and the exponential decay of the double-layers interaction, only the side of the sphere turned towards the air-liquid interface is relevant for the particle-interface electrostatic interaction. Heterogeneities of the particle's surface can thus induce significant changes in the particle-interface interaction when the angle  $\theta_s$  change in time due to thermal fluctuations (figure 4.19(a,b)). Rotational diffusion time-scale, of the order of thousands of seconds for the considered particle [56], would explain why some particles remain in  $d_0^I$  for the whole duration of the experiment.

Surface's heterogeneities can be due to the discretization of the charge, which can modify the interaction potential. Simulations however show [127] that discretization of charge is relevant only in determining the charge inversion originating from ion-ion correlation. Besides that, considering the charge densities of the particles, the mean distance between two discrete charges is of the order of  $l_{dc} \sim 10 \text{ nm}$  and therefore at the typical particle-interface distance of 200-400 nm the surface charge distribution can be considered homogeneous.

A much more relevant possible cause of heterogeneity is the presence of air-bubbles attached to the particle. Rotations bringing the region of particle's surface with the bubble close to the interface can in principle induce an additional attraction as two air-liquid interfaces (the one the bubble and the one of the water surface) attract by van der Waals interaction. The air bubble should however be characterized by an height  $h_b$  (figure 4.19(c)) of the order of 10 nm, since bigger bubbles attached on the particles would be clearly visible on the interference pattern. In 2014 Li *et al.* [128] found that the size of the bubbles on a polystyrene planar substrate depends on the roughness of the latter. They shown that, for nanometric surface roughness, the air-bubbles can have a contact area  $\pi l_0^2$  which overcomes the squared microm-



(a)



(b)

**Figure 4.19:** (a) Sketch illustrating what happens accordingly to the hypothesis of an heterogeneity on particle's surface affecting the interaction between the particle and the air-water interface: once the heterogeneity is far from the interface it does not contribute to the interaction and the particle diffuses both in  $z$  and  $\theta_s$ . Conversely, once for particle's rotational diffusion the heterogeneity turned towards the air-water interface the azimuthal angle  $\theta_s$  is fixed because of the additional attraction between the heterogeneity and the interface. As a result, the equilibrium gap distance change from  $d_0^I$  to  $d_0^{II}$ . (b) Sketch of the lower region of the particle with an air-bubble pinned on its surface. The dashed lines represent the characteristic size of the particle-bubble contact surface  $2l_b$  and the bubble's height  $h_b$ .

eter keeping an height  $h_b$  of tens of nanometers. Such a wide bubble's area, not much smaller than particle's radius, would imply a large attractive van der Waals contribution added to the particle-interface interaction. Such explanation does not account for the increasing probability of the  $d_0^I \rightarrow d_0^{II}$  transition with molarity (fig. 4.10). However one should also take into account the complex way the bubble alters the double layers interaction as, considering the air-bubble, a third double layer is introduced in the system.

### The puzzle of long range hydrophobic interactions

Before concluding the discussion a remark should be made on the subject of long-range hydrophobic interactions as it can be related to our observations. Various experiments made over years pointed out the unexpected adhesion of hydrophobic objects to air-water interfaces in different systems, despite both double-layers and van der Waals interactions are repulsive [3]. As such effect has been observed between hydrophobic objects, it has been named *hydrophobic interaction*. First evidence

of its relevance has been provided by Israelachvili and Pashley [129, 130] who found that hydrophobic forces have a decay length of 1 nm and can be stronger than van der Waals repulsion. Experiments on the critical rupture thickness of liquid films [131] impute also the rupture of water films of much larger thickness (60-220 nm) between air and silica to *long-range* hydrophobic forces (LRHFs), despite a lack of explanation of their exact nature. After more than 30 years of research on this subject, a deep and quantitative understanding of hydrophobic interactions remains elusive [132, 133]. Several mechanisms have been proposed, including: entropic effects due to molecular re-arrangement of water near hydrophobic surfaces [134, 135], correlated charge fluctuations or correlated dipole interactions [136], bridging by nanobubbles [137] and separation-induced cavitation due to the metastability of the water film [138, 139]. We can relate the additional attraction we clearly measured to the still not understood context of such LRHFs. None of the listed explanations which can be found in literature can justify both the time evolution and the reversibility we observe. If the hypothesis of the air-bubble attached at the particle's interface is correct it can be read as a promising new and plausible interpretation of the LRHFs.

## 4.5 Conclusions

In this chapter we shown our experimental results on the particle's potential energy obtained from the probability distribution of the particle-interface distances. Unexpectedly, we found two different potentials yielding two distinct equilibrium positions  $d_0^I$  and  $d_0^{II}$ . A bead can reversibly and rapidly switch from one potential to the other.

The first equilibrium position corresponds to a potential well which can successfully be fitted considering gravity, van der Waals repulsion and double-layers interaction. Following recent works, we shown that the best double-layers interaction model is the one considering the boundary condition of a constant surface potential - and not constant surface charge - at the air-water interface. From the best fit of the potential wells we found an average air-water surface potential of  $-1$  mV, independently from solution's molarity and particle surface charge.

The second equilibrium position  $d_0^{II}$  is not reported in literature and is not predicted by the models. Its clear and unambiguous detection is permitted by the absolute determination of the particle-interface distance  $d$  that our interferometric technique allows. The equilibrium in  $d_0^{II}$  is more stable than the one in  $d_0^I$  and is systematically 50-100 nm closer to the interface. Moreover, the two potential wells  $\Delta U^I$  and  $\Delta U^{II}$  overlap, thus implying different values of the potential for the same value of the distance  $d$ . The system appears to evolve in a reversible way from  $\Delta U^I$  to  $\Delta U^{II}$  when an additional attractive force arises modifying the potential well. The reversibility of the transition implies that the insurgence of  $d_0^{II}$  is not due to eventual pollution of the air-water interface and neither to other non conservative effects. All the observations suggest a potential depending on the tilt angle  $\theta_s$  of the particle as well as on the particle-interface distance  $d$ . The angular dependence can be due to a consistent heterogeneity of the surface of the particle. When  $\theta_s$  is such that the spherical particle turns a region of 'regular' surface towards the interface, the measured potential is the one of the first equilibrium position. Conversely, once for thermal agitation the sphere rotates turning a local anomaly towards the interface, the additional attraction arises. This would cause the approaching of the sphere to the interface and the onset of the second equilibrium position, more stable than the first one. The presence of big air-bubbles pinned on particle's surface, whose presence has been reported on the same material [128, 140], is the most probable source

of heterogeneity, but further studies of the problem are requested.

We also measured the dynamics of particle's partial dewetting after the interface breaching, observing that it is independent from the before-breaching particle-interface interaction. We obtained results similar to what Kaz *et al.* found for a water-oil interface and evaluated the defect area of the surface of our particles from a fit with their model. We verified that the defect area ( $90 \pm 40 \text{ nm}^2$ ) is comparable to the area per charge ( $150 \pm 40 \text{ nm}^2$ ) calculated from the measured values of the Zeta potential of our particles.

The interface crossing is experimentally more probable at high salt molarities, in opposition to the predictions and in a way similar to the probability of the transition  $d_0^I \rightarrow d_0^{II}$ . The two phenomena could therefore be connected.

Even if in previous works there are no evidences of  $\Delta U^{II}$ , its phenomenology is similar to the ones grouped under the name of long-range hydrophobic interactions, observed on different systems but still not successfully described and explained. The verification of the hypothesis of the air-bubbles attached on particle's surface - that we made to justify the angular-dependent additional attraction - is therefore of paramount importance not only to enhance the comprehension of colloids trapping at the air-water interface but also to bring a contribution in the debate on the origin of the long-range hydrophobic interactions.

## Chapter 5

# Dynamics of a spherical particle near an air-liquid interface

In this chapter the analysis of the three-dimensional dynamics of a spherical particle close to an air-liquid interface is described and the corresponding experimental results are illustrated and discussed.

In section 5.1 the diffusion of a colloidal particle close to an interface is studied by computing the Mean Square Displacement (MSD) of particles trajectories measured in chapter 4. The MSD has simple analytical expressions in the case of free diffusion and in the case of diffusion in simple potentials, like the harmonic one. In section 5.1.2 an approach we developed is presented which allows to extract the particle drag perpendicular to the interface from MSD data in a generic potential.

Possible influences on the measured drag related to particle's fluctuations along  $z$  and to the vicinity of other spheres are discussed in section 5.1.3. Then, the obtained results on the drag experienced by the particle in its motion parallel and perpendicular to the interface are given in section 5.2. Curiously, the air-liquid interface behaves as a liquid boundary once the particle moves parallel to the interface and as a solid boundary as it moves in the normal direction. As discussed in section 5.3, this peculiar phenomenon may be related to Marangoni stress arising from a weak concentration of surface active species present at the air-liquid interface. This explanation is not completely satisfying as discrepancies remain with experimental data.

For the sulfate spherical particles an anomalous double population is observed in the parallel drag data (sec. 5.2): for the same air-water interface some particles 'feel' the interface as a liquid boundary while others as a solid one. This intriguing result, also discussed in section 5.3, may possibly be due to electrokinetic effects. This hypothesis, however, requires further studies, as the absence of an established model makes difficult a quantitative assessment of the effect.

### 5.1 Analysis of the dynamics

Before reporting and discussing the drag data, in this section the analysis of the particle dynamics used to recover particle drag coefficients for both the motion parallel ( $\xi_{\parallel}$ ) and perpendicular ( $\xi_{\perp}$ ) to the interface is described.

For a trajectory of  $N_{tot}$  points, the position of the center of each measured particle in the  $n$ -th frame, with  $n$  ranging from 0 to  $N_{tot} - 1$ , is

$$\vec{x}_c(t_n) = x_c(t_n)\hat{e}_x + y_c(t_n)\hat{e}_y + z_c(t_n)\hat{e}_z, \quad (5.1)$$

where  $t_n = n\delta t$  and  $\delta t$  is the time interval between two frames, ranging between 1/50 s and 1/35 s. Here we consider the particle's coordinates  $x_c$  and  $y_c$  after the removal from the data of an eventual drift contribution<sup>1</sup>. For consistency with chapter 4, we consider the gap distance  $d$  and not  $z_c$  as the coordinate in the direction perpendicular to the interface. Considering a given lag time  $\tau_i$ , all possible displacements which occur along the three coordinate axes during this interval are:

$$\Delta x_i(t_n) = x_c(t_n + \tau_i) - x_c(t_n) \quad (5.2)$$

$$\Delta y_i(t_n) = y_c(t_n + \tau_i) - y_c(t_n) \quad (5.3)$$

$$\Delta d_i(t_n) = d(t_n + \tau_i) - d(t_n), \quad (5.4)$$

where  $0 < t_n < (N_{tot}\delta t - \tau_i)$  and the index  $i$  denotes the dependence on the chosen time lag.

Figure 5.1(a,b,c) reports histograms of the displacements along the three axes at lag time  $\tau_i = \delta t$ . They have a Gaussian distribution which suggests a Brownian origin of the motion. The distributions of  $\Delta x_i$  (fig. 5.1(a)) and  $\Delta y_i$  (fig. 5.1(b)) are identical at the resolution of the measurements, thus implying that the motion in the plane parallel to the interface is isotropic. Conversely, in figure 5.1(c) it can be seen that the correspondent distribution of  $\Delta d_i$  is narrower than the ones of  $\Delta x_i$  and  $\Delta y_i$ . This is the signature of a dynamics perpendicular to the interface slower than the parallel one, in agreement with theoretical predictions (sec. 1.2).

The viscous drag can be obtained from the measurements of the MSDs along the three axes, defined for a lag time  $\tau_i$  as  $\langle \Delta x_i^2 \rangle_n$ ,  $\langle \Delta y_i^2 \rangle_n$  and  $\langle \Delta d_i^2 \rangle_n$ .

### 5.1.1 Measurement of the parallel drag

In figure 5.1(d) the MSDs evaluated along the three directions are reported. It can be seen that  $\langle \Delta x_i^2 \rangle_n$  and  $\langle \Delta y_i^2 \rangle_n$  are linear and that superimpose. The superposition is a consequence of the isotropy of the motion in the plane parallel to the interface, while the linearity in the lag time is the signature of a freely diffusive regime as in such regime hold the following relations:

$$\langle \Delta x_i^2 \rangle_n = 2D_x\tau_i \quad (5.5)$$

$$\langle \Delta y_i^2 \rangle_n = 2D_y\tau_i, \quad (5.6)$$

where  $D_x$  and  $D_y$  are the diffusive coefficients along  $x$  and  $y$ . The linear fit of the  $x$  and  $y$  MSDs gives therefore access to the diffusion coefficients. Because of the  $xy$  isotropy, from now we consider instead of  $D_x$  and  $D_y$  their average<sup>2</sup>  $D_{||}$ . The parallel drag  $\xi_{||}$  is then obtained from  $D_{||}$  using the relation 1.44.

<sup>1</sup>The measured drift velocities along  $x$  and  $y$  are constant in the experimental time scales (sec. 3.2.1). They are therefore obtained dividing the total path traversed along  $x$  and  $y$  by the duration time of the measurement. The corrections of the trajectories are then made by subtracting to  $x_c(t_n)$  and  $y_c(t_n)$  the corresponding drift velocities multiplied for  $t_n$ . The drift subtraction is not made for  $z_c$  as we just consider particles moving in the equilibrium regime, confined along  $z$  in the potential wells described in chapter 4.

<sup>2</sup>Before making the average, however, for each measured particle we verify that  $D_x$  and  $D_y$  coincide in the experimental error bars. This check is made to exclude the possibility that anomalous values of  $D_{||}$  could arise from an anisotropy between  $x$  and  $y$ .

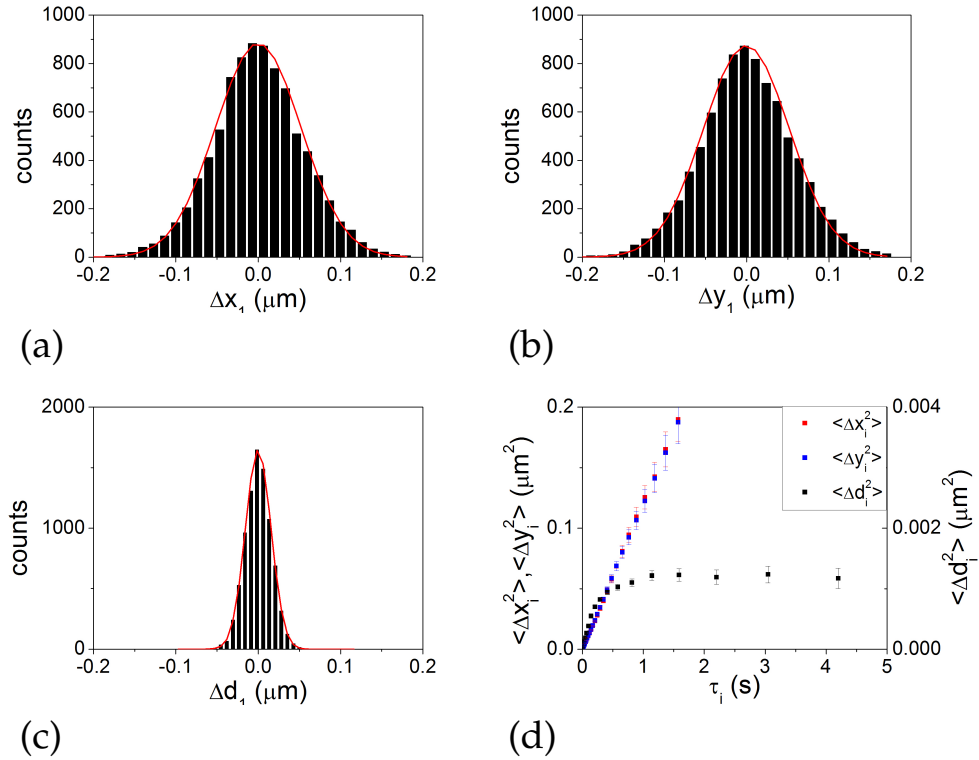


**Figure 5.1:** Typical histograms of the displacements along the three axes at lag time  $\tau_i = \delta t$ : (a) histogram of  $\Delta x_1$ , (b) histogram of  $\Delta y_1$  and (c) histogram of  $\Delta d_1$ . (d) Typical Mean Square Displacements along the three axes as a function of  $\tau_i$ . Note that the MSD in the perpendicular direction  $\langle \Delta d_i^2 \rangle_n$  is reported in an enlarged different scale (on the right) for a better visualization.

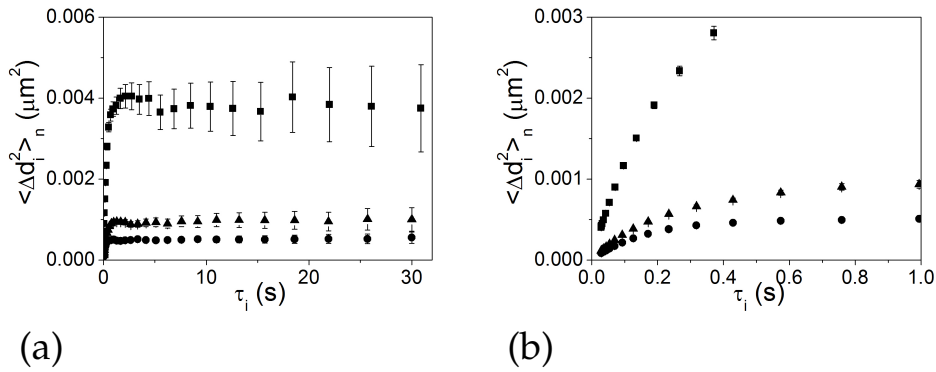


**Figure 5.2:** Examples of  $\langle \Delta d_i^2 \rangle_n$  versus  $\tau_i$  for three different particles at different distances from the interface (see table 5.1). Two different zooms of the same MSD are reported: (a) a wider one, where the plateaux can be seen, and (b) another at short lag time, where the differences in the transient's slopes are more evident.

symbol	$d_0$ (nm)	$c$ (mM)	$\sqrt{MSD(\infty)}$ ( $\mu m$ )	potential half-width ( $\mu m$ )
squares	450	0.015	0.063	0.060
triangles	248	0.1	0.032	0.028
circles	238	0.5	0.022	0.023

**Table 5.1:** Measured parameters of the three particles whose MSD is reported in figure 5.2. In column's order: equilibrium distances ( $d_0$ ), solution molarities ( $c$ ), square root of the plateau value of the MSDs ( $\sqrt{MSD(\infty)}$ ) and half-width of the potential wells at  $1 k_B T$  as they are measured in chapter 4.

### 5.1.2 Measurement of the perpendicular drag

The MSD along  $z$  reported in figure 5.1(d) is not linear but reaches a plateau value after a transient. This is a clear signature of a confined motion. The fact that the distribution of  $\Delta d_i$  in figure 5.1(c) appears to be Gaussian implies that at lag time  $\tau_i = \delta t$  the particle's motion is weakly affected by the confinement in the potential well.

In figure 5.2 three more examples of  $\langle \Delta d_i^2 \rangle_n$  are shown for three particles at different distances from the interface, as reported in table 5.1.

In 5.2(a) the value of the plateau decreases when the particle is closer to the interface. This is a direct consequence of the narrowing of the particle's potential wells as the particle approaches to the interface ( $d_0$  decrease), as reported in table 5.1 (note the correspondence between the square root of the MSD's plateau values reported in the fourth column and the potential half-widths at  $1k_B T$  of the fifth column). In fig. 5.2(b) is shown the zoom of the transient regime at short lag time before reaching the plateau. The slope at the origin of  $\langle \Delta d_i^2 \rangle_n$  is lower for particles closer to the interface, thus indicating that the normal drag  $\xi_\perp$  is higher.

For the motion perpendicular to interface the MSD depends on the expression of the potential [141]. Noting  $F(d)$  as the conservative force acting on the particle and  $\sqrt{2k_B T \xi_\perp} W(t)$  the stochastic force ( $W(t)$  is the white noise), the Langevin equation along  $z$  reads:

$$m\dot{v}_z = F(d) - \xi_\perp v_z + \sqrt{2k_B T \xi_\perp} W(t), \quad (5.7)$$

where  $m$  is the mass of the particle and  $v_z$  its velocity along  $z$ .

In the case of an harmonic potential, an analytical expression for the MSD can be found. Noting  $\omega_0$  the resonant frequency of the harmonic potential, the correspondent force is

$$F(d) = -m\omega_0^2 (d - d_0) \quad (5.8)$$

Defining  $\tilde{\omega}_0 = \sqrt{\omega_0^2 - \left(\frac{\xi_\perp}{2m}\right)^2}$  and following ref. [142, 76], the MSD results in:

$$\langle \Delta d_i^2 \rangle_n = \frac{2k_B T}{m\omega_0^2} \left\{ 1 - \exp\left(\frac{-\xi_\perp \tau_i}{2m}\right) \left[ \cos(\tilde{\omega}_0 \tau_i) - \frac{\xi_\perp}{2m\tilde{\omega}_0} \sin(\tilde{\omega}_0 \tau_i) \right] \right\} \quad (5.9)$$

This equation is commonly employed to fit data for particles confined in harmonic potentials, as for example in the case of particle diffusing inside an optical trap [76].

In the overdamped regime ( $\xi_\perp/m > 2\omega_0$ ) eq. 5.9 has the same qualitative trend of the measured MSDs reported in figure 5.2. Driven by such qualitative agreement, we checked if the harmonic approximation was suitable in our case. In order to do this, we simulated the diffusion of particles in the measured potentials (chapter 4) and analyzed the obtained trajectories with eq. 5.9. In order to implement the simulations, we generalized the procedure followed by Volpe and Volpe [143], who simulated a motion confined in the simpler case of an harmonic potential. In the overdamped limit of our experiment we can neglect the inertial term of Langevin equation (non-inertial approximation) as the time scale of the recall force  $\xi/(m\omega_0^2)$  is much greater than the ballistic relaxation time  $m/\xi$  (*i.e.* the time scale of the transition from ballistic to diffusive behaviour). By replacing the harmonic term with a generic force  $F(d)$  and by neglecting the inertial term of Langevin equation, eq. 5.7 can be rewritten as [143]:

$$\dot{d}(t) = \frac{F(d)}{\xi_\perp} + \sqrt{2 \frac{k_B T}{\xi_\perp}} W(t) \quad (5.10)$$

The corresponding finite differential equation is

$$d_i = d_{i-1} + \frac{F(d_{i-1})}{\xi_\perp} \delta t + \sqrt{2 \frac{k_B T}{\xi_\perp}} \delta t w_i, \quad (5.11)$$

where  $w_i$  is a Gaussian random number with zero mean and unit variance<sup>3</sup>. The force  $F(d)$  is given by the  $d$ -derivative of the potential ( $F(d) = -\partial U/\partial d$ ) and can be evaluated from the probability distribution of  $d$ . Using equation 4.4 we obtain:

$$F(d) = k_B T \left[ \frac{1}{N(d_0)} \frac{\partial N}{\partial d} \frac{N(d_0)}{N(d)} \right] \quad (5.12)$$

The discretized expression for the force is therefore:

$$F(d_{i-1}) = - \frac{k_B T}{N(d_{i-1})} \left. \frac{\partial N}{\partial d} \right|_{d_{i-1}} \quad (5.13)$$

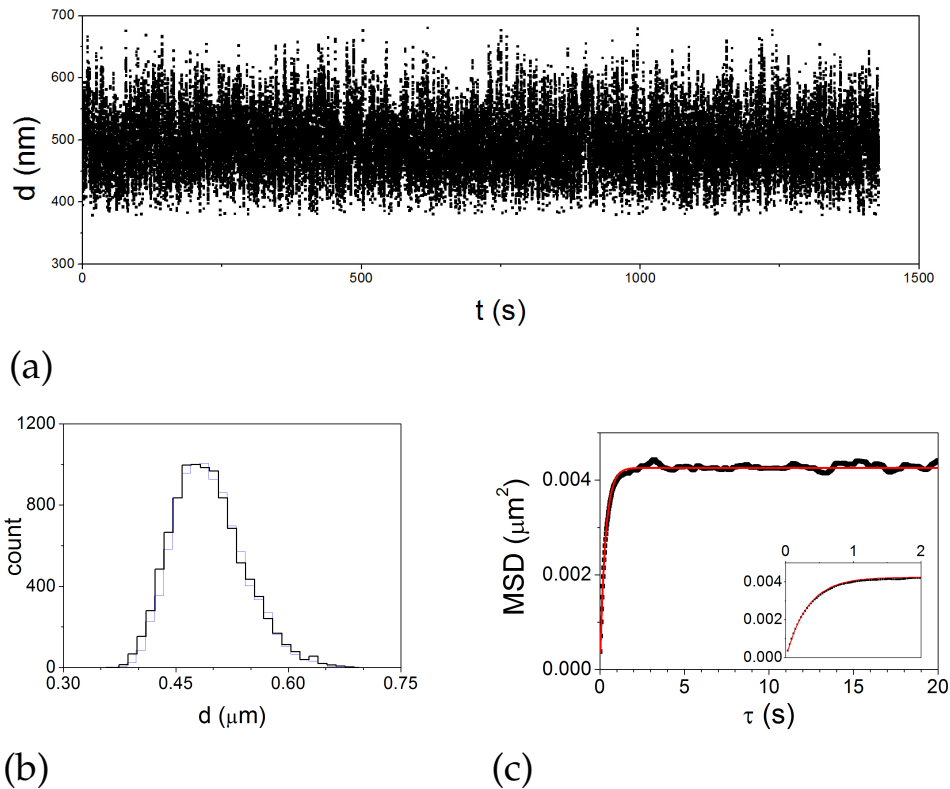


**Figure 5.3:** Typical result of the simulation of particle motion along  $z$  obtained from the measured  $N(d)$ . (a) Simulated  $d(t)$ . (b) Comparison of the measured  $d$ -histogram used for the simulation (blue) with the one obtained from the simulation (black). (c) MSD (black points) of the trajectory reported in (a) fitted with eq. 5.9 (red line). In the inset of (c) is reported a zoom at short lag time of the MSD to visualize the transient of the MSD.

An algorithm has been written combining eq. 5.11 with eq. 5.13 which generates simulated trajectories from the measured probability distribution of  $d$  and for different drag coefficients. In figure 5.3 an example of the obtained result is reported. In figure 5.3(b) the histogram of the simulated  $d$  (black line) is plotted together with the histogram of the measured  $d$  from which the simulation has been made.

The MSD recovered from the simulation, in figure 5.3(c), is fitted with the analytical expression for an harmonic potential (eq. 5.9). The obtained drag  $\xi_{\perp,fit}$  is then compared with the input one  $\xi_{\perp,in}$  of the simulation. The result of this comparison is reported in figure 5.4 for three different series of simulations. Each series is made using a different measured potentials having equilibrium positions at 230 nm (black squares), 420 nm (red squares) and 550 nm (blue squares). For each potential well several simulations are made for different input drags. In figure 5.4 the ratio  $\tilde{r} = \xi_{\perp,fit}/\xi_{\perp,in}$  is reported versus the adimensional input drag coefficient  $f_{\perp,in} = \xi_{\perp,in}/\xi_{\infty}$  (being  $\xi_{\infty}$  the drag in the bulk, sec. 1.2). For low drag coefficients the fit undervalues the input drag. On the other side, as the input drag increases,  $\tilde{r}$  also increases well over unity. Besides this, there is not a clear trend with the potential concavity (as reported in chapter 4, potential's concavity increases with  $\langle d \rangle$ ). The  $\tilde{r}$  for the halfway equilibrium position (red squares), for example, does not exhibit an intermediate behaviour between the ones for the largest (blue squares) and the lowest (black squares) equilibrium positions.

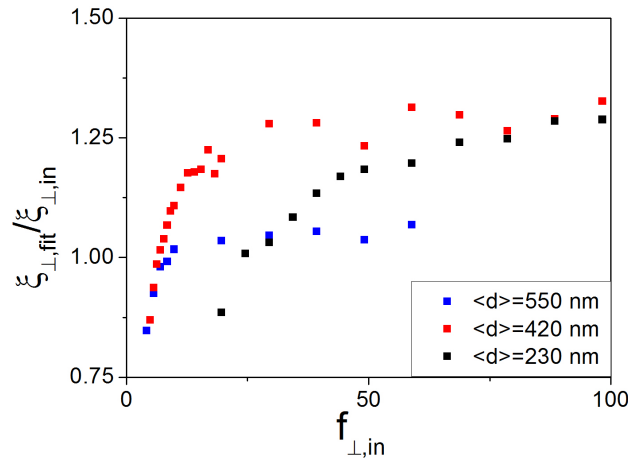


**Figure 5.4:** Results of the analysis of the simulations: ratio  $\tilde{r} = \xi_{\perp,fit}/\xi_{\perp,in}$  versus the adimensional (input) drag coefficient  $f_{\perp,in} = \xi_{\perp,in}/\xi_{\infty}$ . Each point correspond to a different simulation. Each set of simulations (different colors) differs in the measured histogram  $N(d)$  used to settle the simulations. The three corresponding real trajectories have average distances from the interface equal to:  $\langle d \rangle = 550 \text{ nm}$  (blue),  $\langle d \rangle = 420 \text{ nm}$  (red) and  $\langle d \rangle = 230 \text{ nm}$  (black).

The results shown in figure 5.4 suggest that the use of the harmonic approximation to extract the drag from the measured MSD brings a very imprecise result. Drag recovered by such fit in some cases revealed discrepancies of more than 100%. In addition, the complexity of the model potential (eq. 4.15) discourages the search of

<sup>3</sup>For the reason why  $W(t)$  can be discretized as  $w_i/\sqrt{\delta t}$ , see Volpe and Volpe [143] and Øksendal [144] dissertations.

an analytical expression for the MSD. We thus chose to work with a simulation approach as summarized in table 5.5. For each particle the measured distribution of  $d$  is used to settle a series of simulations of corresponding  $z$ -trajectories having the same number of points of the measured one. The input drag of the simulation,  $\xi_{\perp, in}$ , is changed until the  $d$ -MSD of the simulation reproduces the experimental one. In practice, the criterion of convergence is when the fit with eq. 5.9 of both MSDs returns the same parameters in the range of the error bars. Because of the randomly generated white noise and the finite number of points per simulation, two simulations made with identical parameters return slightly different MSDs. To evaluate the incertitude a number of simulations are thus generated (with same parameters) and fitted with eq. 5.9 until the standard deviation of the fitted drag stabilizes at a given value  $\sigma_{\xi}$ . If the drag obtained from the fit on the measured MSD falls within the interval of the standard deviation, we attribute to particle's normal drag the correspondent input value of the simulation with an incertitude equal to<sup>4</sup>  $\sqrt{2}\sigma_{\xi}$ .

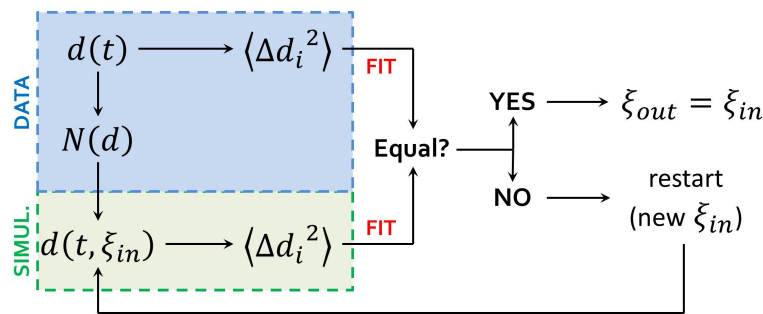


**Figure 5.5:** Sketch summarizing the procedure to measure the perpendicular drag starting from data and simulations, as described in the text. The output drag  $\xi_{out}$  is the resulting value of the perpendicular drag associated to the particle.

### 5.1.3 Effects of vertical fluctuations and neighbourhood particles

Before reporting the experimental results, we need to discuss possible issues related to the measurement and analysis of the drag.

Firstly, we have to take into account that drag coefficients depend on the distance from the interface (sec. 1.2). Because of the diffusive motion of the particles along  $z$ , the drag experienced by the particle instantaneously changes during the trajectories. From the MSDs analysis we therefore get a mean diffusion which in principle is different from the correspondent diffusion evaluated in the mean position  $\langle d \rangle$ :

$$\langle D(d) \rangle_t \neq D(\langle d \rangle_t) \quad (5.14)$$

However, looking at the distributions of displacements of figure 5.1(a,b,c) we expect this effect to be small in our case. Indeed, a time-dependent diffusion should in principle lead to non-Gaussian distributions of the displacements  $\Delta x$ ,  $\Delta y$  and  $\Delta d$  [145]. The Gaussian character of the measured distributions thus suggest that in our case such contribution is negligible.

<sup>4</sup>The factor  $\sqrt{2}$  arise from the sum of the uncertainty due to the finite number of data in simulations,  $\sigma_{\xi}$ , and the same uncertainty (the number of observations is the same) associated to the measured data.

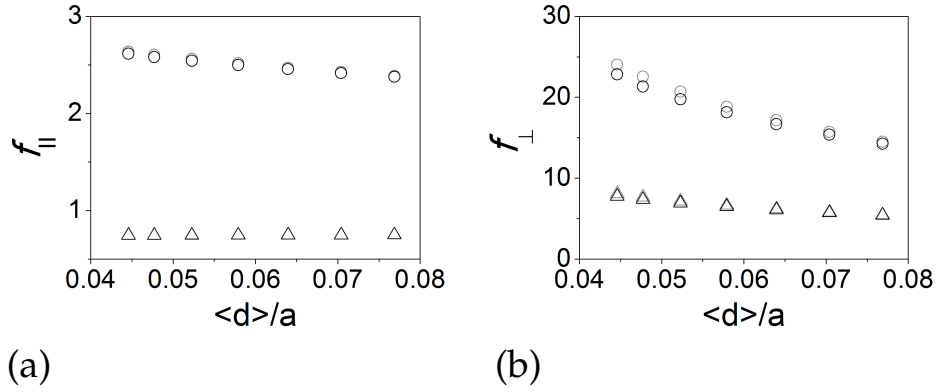


**Figure 5.6:** Predicted adimensional drags  $f_{\parallel}$  and  $f_{\perp}$  for a motion at fixed distance from the interface (grey points) and for a motion with fluctuating distances  $d$  having a typical measured probability distribution with average  $\langle d \rangle$  (black points) as a function of the normalized average distance from the interface  $\langle d \rangle / a$ . (a)  $f_{\parallel}$  for a liquid-air (void triangles) and a liquid-solid (void circles) interface. (b)  $f_{\perp}$  for a liquid-air (void triangles) and a liquid-solid (void circles) interface.

In order to rigorously quantify the effect we evaluated the average diffusion weighted on the probability distribution of distances  $p(d)$  measured in chapter 4. The resulting formula for the drag coefficient reads:

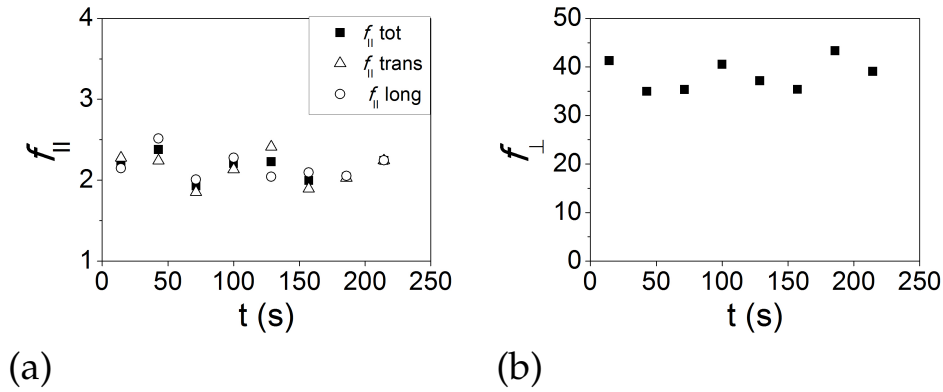
$$\langle \xi_{\parallel, \perp} \rangle = \frac{\int p(d) dd}{\int \frac{p(d)}{\xi_{\parallel, \perp}(d)} dd} \quad (5.15)$$

Figure 5.6 shows the comparison between the predicted drag for an instantaneous motion at fixed distance (grey points) and the one obtained using eq. 5.15 and a typical measured  $p(d)$  (black points).

The considered effect principally affects the perpendicular drag close to a liquid-solid interface, reducing it by a factor 5% when  $d/a < 0.05$  (fig. 5.6(b)), and is negligible if the liquid-air boundary conditions are considered.

Measurements of the particle drag can be affected by the presence of other spheres in the proximities. When two particles suspended in a liquid are close enough, propagation of fluid flow generated by their motion results in an hydrodynamic coupling of the two particles. As a consequence, the resulting drag a particle experienced is altered by the vicinity of the other one. It is important to know at which inter-particles distance this effect becomes significant in order to assess that the dynamics of a particle we are measuring is not affected by the presence of a second one (or more) outside the camera's field of view. In 3D bulk fluids, the intensity of the hydrodynamic coupling decays as the inverse of particles' distance. When fluid flow is confined in two dimensions with full-slip boundary conditions the coupling becomes long range as it decays logarithmically with their distance [146].

A simple test has been made to assess the relevance of hydrodynamic coupling. In figure 5.7, the time evolution of the drag ratios  $f_{\parallel} = \xi_{\parallel} / \xi_{\infty}$  and  $f_{\perp} = \xi_{\perp} / \xi_{\infty}$  for a sphere moving close to the air-liquid interface is reported. The evolution of the



**Figure 5.7:** (a) Time evolution of  $f_{\parallel}$  for a spherical particle while a second one is approaching. In the plot are reported the two  $f_{\parallel}$  transversal (void triangles) and the longitudinal (void circles) to the axis between the two particles, together with the total  $f_{\parallel}$  (plain squares). (b) Time evolution of  $f_{\perp}$  for the same sphere of (a).

drag has been evaluated by computing the MSD in trajectory's subintervals of 1000 frames. At the beginning of the video the sphere is alone in the microscope field of view, and thus at a distance from other spheres of more than  $50 \mu\text{m}$ . During the recording, a second particle approaches and at the end of the measurement the two particles are  $22 \mu\text{m}$  apart. Figure 5.7 shows that both  $f_{\parallel}$  and  $f_{\perp}$  remain constant during the approaching of the second particle, meaning that at the experimental resolution there is no contribution from the coupling to the drag.

The absence of hydrodynamic coupling is also confirmed by the identical measurement of the parallel drag in the directions transverse (void triangles) and longitudinal (void circles) to the axis connecting the particles.

## 5.2 Measured drag coefficients

Figures 5.8(a) and 5.8(b) report the measured adimensional drag coefficients parallel and perpendicular to the interface respectively. They are obtained, as described in sec. 5.1, from the measured 3D trajectories of particles moving around the equilibrium positions  $d_0^I$  and  $d_0^{II}$ . The values of  $f_{\parallel}$  and  $f_{\perp}$  are given as a function of  $\langle d \rangle / a$ , where  $\langle d \rangle$  is the particle-interface distance averaged over the duration of the measurement. Each point corresponds to a different particle.

In the plots the theoretical predictions for the drag parallel and perpendicular to both a liquid-air (LA) - eq. 1.31 and 1.28 - and a liquid-solid (LS) - eq. 1.32 and 1.30 - interface are also reported<sup>5</sup>.

A first observation is that the measured drag doesn't correspond to the expected predictions for a full-slip boundary condition. The parallel drag is always larger than LA prediction, with values mostly scattered between LA and LS and sometimes larger than LS. The perpendicular drag follows roughly LS prediction with a large number of values below and above the LS curve.

In figure 5.9 the parallel drag values are reported separating data relative to SS particles (a) from the ones relative to CS particles (b). Different colors represent different molarities of the solution, while different symbols in fig. 5.9(b) correspond

<sup>5</sup>The LA theory considers full-slip boundary conditions at the air-liquid interface, under the limit  $\eta_2/\eta_1 \rightarrow 0$ . Conversely, the liquid-solid (LS) theory considers perfectly no-slip boundary conditions.

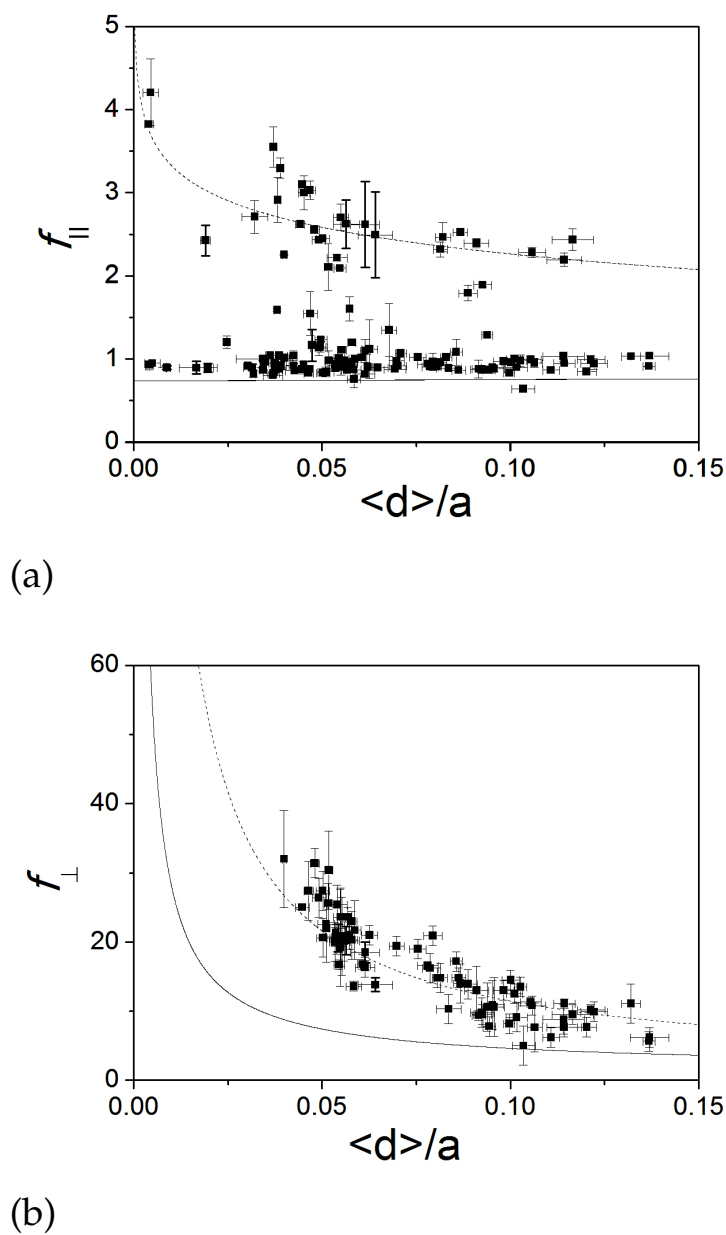
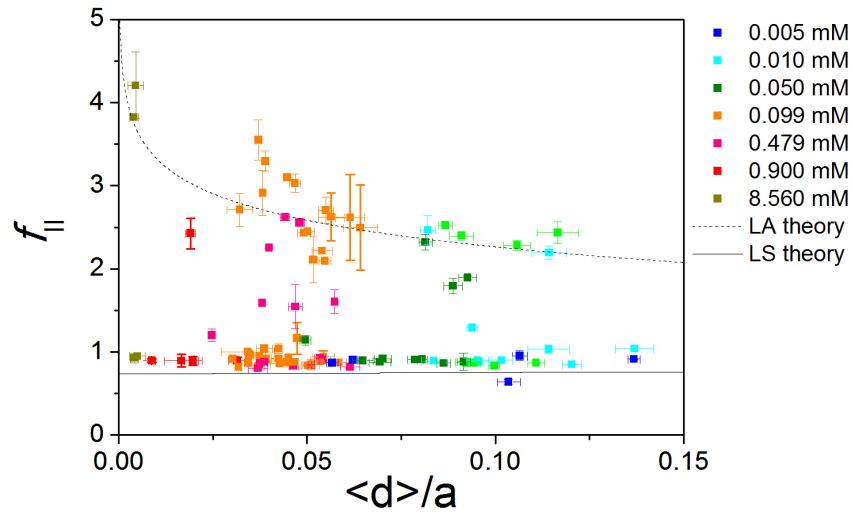
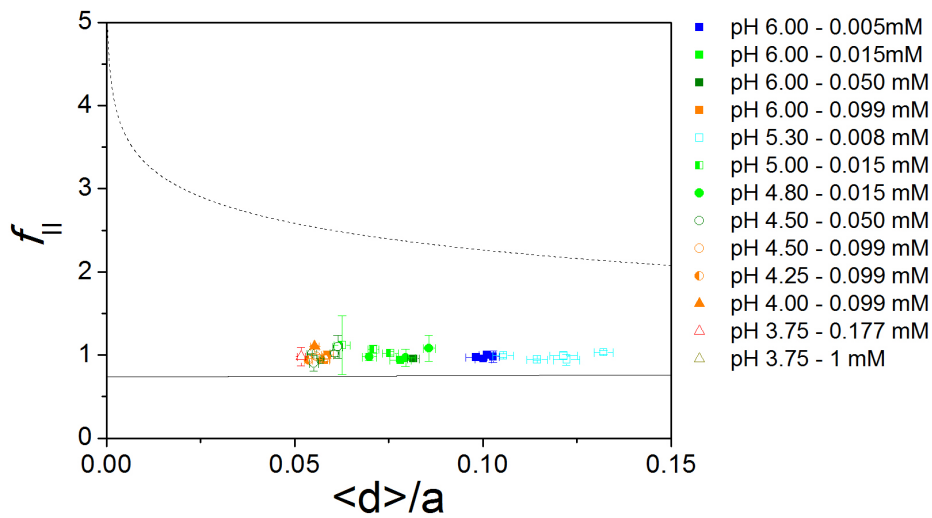


**Figure 5.8:** Adimensional parallel  $f_{\parallel}$  (a) and perpendicular  $f_{\perp}$  (b) drag coefficients measured for SS and CS particles in water solutions versus the average distance from the interface scaled on the radius. Data refer to different molarities and, for carboxylated particles, pH. Theoretical predictions are also reported for no-slip (dashed line) and full-slip (continuous line) boundary conditions.



(a)



(b)

**Figure 5.9:** Adimensional parallel drag coefficient  $f_{\parallel}$  measured for SS (a) and CS (b) particles in water solutions versus the average distance from the interface scaled on the radius. Data refer to different molarities and, for carboxylated particles, pH. Different colors indicate different molarities and different shapes indicate different pH, accordingly to the legends. Theoretical predictions are also reported for no-slip (dashed line) and full-slip (continuous line) boundary conditions.

to different values of  $\text{pH}$ . Both these parameters mainly affect data as they change the average distance  $\langle d \rangle$  from the interface.

Parallel drags of SS particles are widespread between LA and LS curves, but with larger concentration of values close to the LA and slightly larger than it, and a less populated group closer to LS. In same samples (*i.e.* same air-liquid interface) different particles belong either to the first population or to the second one (*e.g.* the dark green points corresponding to data for  $c = 0.05$  mM). Unlike SS particles, CS particles all show a parallel drag close and slightly above the LA prediction.

No substantial differences exist between the drag measured on particles fluctuating around  $d_0^I$  and  $d_0^{II}$ : in the latter case particles are closer to the interface and exhibits a larger drag, but follow the same described trend.

### 5.3 Discussion on drag values and comparison with theoretical models

The results shown in figure 5.8 open a number of questions that are addressed in the following. First, how does a full-slip LA interface may behave like a no-slip LS boundary as we observe for the perpendicular drag of both kind of particles? For particles sharing the same interface, why is the drag close to the LS prediction for some of them and to LA ones for others? Why is the parallel drag systematically larger than the one expected for a LA interface?

#### 5.3.1 Surface incompressibility

A first mechanism one need to discuss is the effect of a possible presence of surface active species other than water molecules at the interface which may modify boundary conditions. Indeed, a recent experimental study [66, 67] showed that the full-slip boundary condition is not always realized at a liquid interface. Even if great precautions is paid to keep clean the interface, it is quite impossible to avoid the existence of a low concentration of surface impurities. Nevertheless, dramatic contamination of the interface during experiments affecting interface viscosity (sec. 1.2.2) has to be excluded, as surface tension measurements proved (section 3.1.3). As described in section 1.2.2, apart from the modification of interface viscosity, an effect on the boundary conditions can arise at very low surface concentration of active species ( $c_0^i \sim 10^{-4}$  nm<sup>-2</sup>): a non-uniform concentration of them, induced by the motion of a particle, can produce tangential stress that resists to the particle motion.

Maali *et al.* (2017) [12] observed that viscous drag corresponds to the one of the LA prediction at high frequencies<sup>6</sup> ( $\geq 400$  Hz) and to the one of the LS when the frequency is lowered down to 100 Hz (see figure 5.10). The authors explain such result considering a 2D ideal gas of surface impurities trapped at the interface<sup>7</sup>. According to their model, the presence of impurities gives rise to surface incompressibility because of the Marangoni stress opposing to concentration distortions. At high frequencies, impurities have not sufficient time to respond to the particle motion and the interface behaves as a pure LA one. When the frequency is lowered below a threshold frequency related to  $c_0^i$  (eq. 1.36), the opposite happens, *i.e.* the interface behaves as a LS boundary.

Unlike the cited paper, in our measurements the particle spontaneously moves in a potential and is not forced to oscillate at a given frequency. The analysis of the

<sup>6</sup>As detailed in section 1.2.2, Maali *et al.* made measurements on particles forced to oscillate at given frequencies perpendicular to an air-water interface.

<sup>7</sup>see section 1.2.2 for more details on the model.

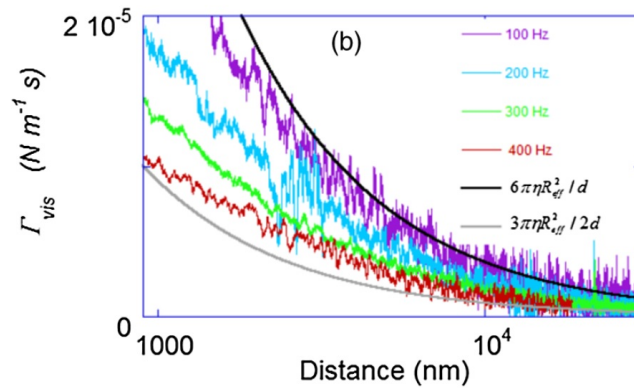


**Figure 5.10:** Drag coefficient (here reported as  $\Gamma_{vis}$ ) versus particle-interface gap distance ( $D$ ) measured in ref. [12] for a  $50 \mu\text{m}$  particle oscillating in water at different frequencies perpendicular and close to an air-water interface. The calculated drag coefficient corresponding to full-slip and no-slip boundary conditions on the interface are represented by the gray and dark line, respectively. Note that the covered range of adimensional distances  $d/a$  is comparable to the one of the present work.

power spectrum  $|\mathcal{F}[d]|^2$  of the trajectories we measure (fig. 5.11) shows that at 10 Hz the frequency components are already 2-3 order of magnitude smaller than the maximum of the power spectrum. It is therefore conceivable to consider only lower frequency components as responsible for the value of the drag. Since 10 Hz is a frequency much lower than Maali *et al.* lower limit, our perpendicular drag data can thus in principle be interpreted using their model. Nevertheless, looking closer to fig. 5.8(b) a significant number of drag values are found larger than LS boundary curve. This is unexpected and cannot be explained with pure hydrodynamic arguments, as the reported LS theory is the upper hydrodynamic limit for the drag close to a plane interface.

Concerning the effect of surface incompressibility on the parallel drag, numerical calculations by Blawdziewicz *et al.* [65] shown a drag coefficient at  $d = 0$  of  $f_{\parallel}^c = 0.82$ , slightly higher than the corresponding value for a compressible interface  $f_{\parallel}^i = 0.73$ . The effect of surface active species on parallel drag is thus expected to be much lower than the one on perpendicular drag.

To physically grasp the origin of this difference one can refer to fig. 5.12(a) and fig. 5.12(b). In fig. 5.12(a) is reported the case of the perpendicular drag: a particle is approaching to the interface generating a radial flux on it. It is clear that a flux of this kind is not compatible with a zero-divergence of the 2D flow field correspondent to the condition of surface incompressibility. From a microscopic point of view, the initial homogeneous concentration  $c_0^i$  of surface active species is modified as they are dragged by the flux. The gradient of active species concentration results in a Marangoni stress which generates a flux opposing to the one generated by the motion of the particle. If the typical times associated to the particle motion are large enough compared to the impurities typical times (*i.e.* if we are in the quasi-static limit) the fluid cannot flow any more at the interface. The boundary conditions thus become the no-slip ones.

On the other side, for a particle moving parallel to the interface (fig. 5.12(b)) the 2D flow field at the interface can satisfy the zero-divergence condition requested by the interface incompressibility. Clearly, also in this case a gradient of active species is established (high concentration in front of the particle and low behind it) giving rise

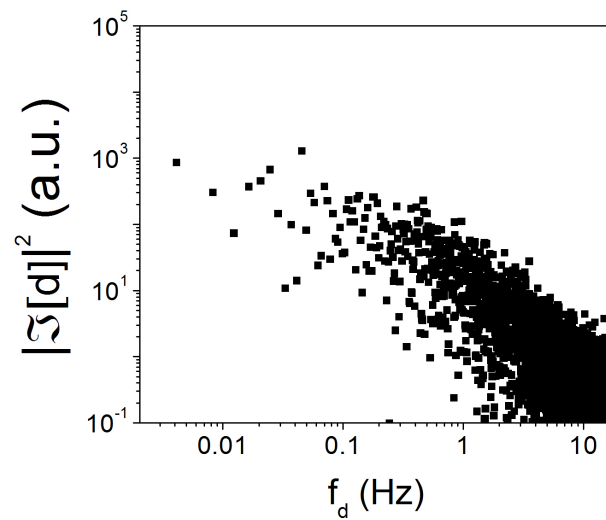


**Figure 5.11:** Power spectrum of  $d$  for a sulfate sphere versus the frequency  $f_d$ .

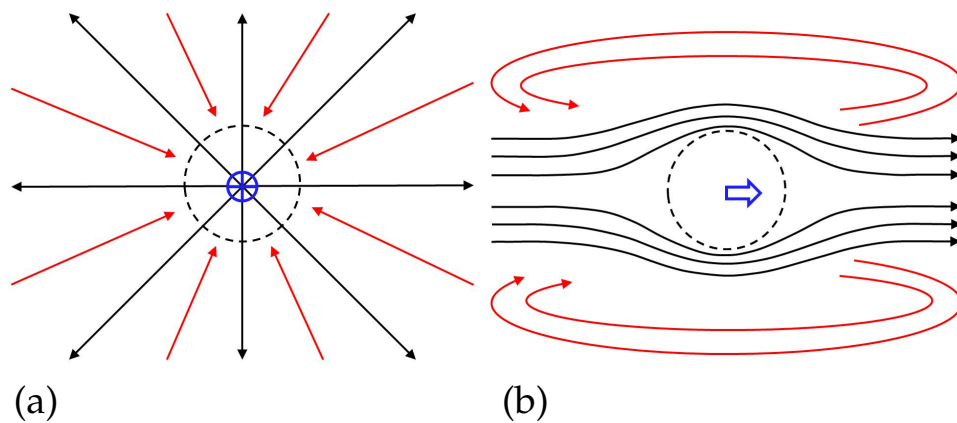


**Figure 5.12:** Sketch of the top view of the hydrodynamic fields produced at the interface when a spherical particle (dashed line) moves normal (a) and parallel (b) to the interface. The 2D flux on the interface (black arrows) associated to the motion of the particle (blue arrow) induces gradients in the distribution of active species at the interface. The correspondent Marangoni flow (red arrows) restoring the homogeneous concentration  $c_0^i$  directly opposes to the particle's flux in (a) while a 2D flow at zero-divergence is still possible in (b).

to a Marangoni flow which adds to the viscous one. The particle drag is thus larger than the one expected for a pure LA interface but doesn't reach the value expected close to a solid wall.

In figure 5.13 the predicted  $f_{\parallel}$  drag ratio for an incompressible (dotted line) and compressible (continuous line) LA interface are reported together with the measured values for SS (a) and CS (b) particles. Data deviates from the incompressible interface theory less than from the compressible one, even if a discrepancy between models and experimental values still remains.

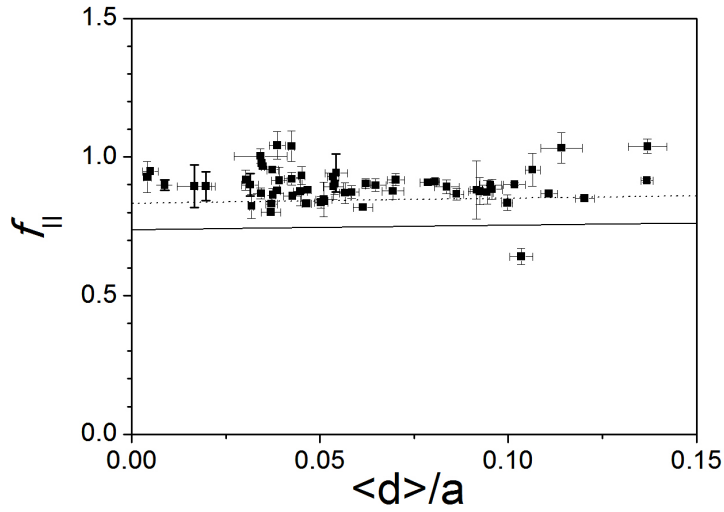
Apart from adsorbed impurities, surface active species originating surface incompressibility condition may also be ionic species such as  $\text{OH}^-$  or carbonate and bicarbonate ions (section 1.1.3). As described in section 1.1.3, the interface is negatively charged probably due to a specific adsorption of such ions. As well as inhomogeneity in the concentration of the impurities would produce a tangential stress, the same in principle can arise from a non uniform concentration of surface ions. Their concentration can be evaluated from the measured surface potential (chapter 4) as of the order of  $10^{-5} - 10^{-6} \text{ nm}^{-2}$ , lower than the concentration of impurities  $c_0^i \sim 10^{-4} \text{ nm}^{-2}$  estimated from eq. 1.36 for a threshold frequency of 100 Hz. However, the stress induced by the gradient of concentration of ions is enhanced by their electrostatic repulsion, absent in the case of the ideal gas of independent molecules supposed by Maali *et al.*

### 5.3.2 Possible electrokinetic effects on the drag

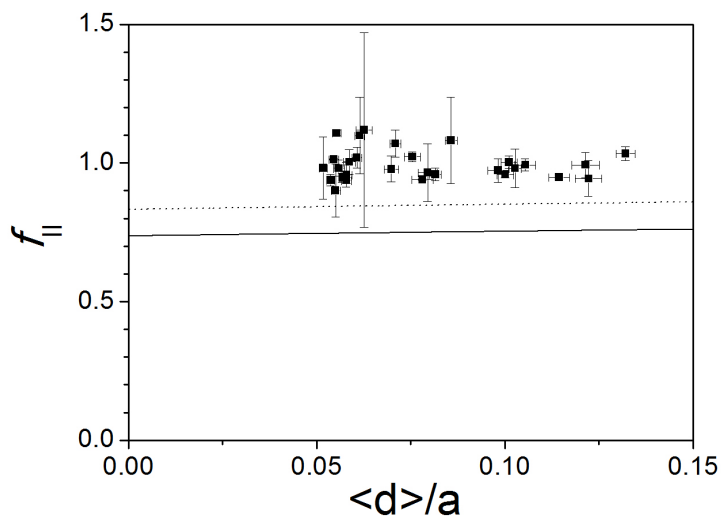
Interface incompressibility due to the presence of surface active species gives reason for the  $f_{\perp}$  measured close to LS predictions, but is not sufficient to entirely reconcile the model with the experimental data. In the parallel direction,  $f_{\parallel}$  is still always significantly larger than the predicted value. In particular, surface incompressibility is not able at all to rationalize the parallel drag values 2-3 times higher than  $\xi_{\infty}$  we observed only in the case of sulfate spheres. Such behaviour is not sample-dependent, as samples have been observed where both particles exhibiting low ( $\sim 1$ ) and large ( $\sim 2 - 3$ )  $f_{\parallel}$  have been measured. It is not even time-dependent, as shown in fig. 5.14 where measured  $f_{\parallel}$  are reported versus time  $t'$  from the sample preparation. This excludes that the ambivalence is due to surface contamination occurring in the experiment time interval<sup>8</sup>. The hypothesis of a patchy contamination of the surface affecting only the motion of some spheres seems unrealistic as concentration gradients tend to zero. Moreover, the eventual presence of drops of viscous contaminants not miscible with water can be excluded as they would be easily detected by the interferometric setup. It seems therefore that the measured behaviour is determined by characteristics of the single spheres. No dependence on particle radius is observed in the data and all particles have been cleaned by several dilution cycles before experiments in order to remove possible surfactants from their solution. A last possible difference can be in the charge distribution on the surface of each particle.

In figure 5.15 the perpendicular drag data for sulfate spheres are reported marking with different colours particles whose parallel drag (see figure 5.9(a)) follows LA prediction (black) and particles whose parallel drag is closer to the LS prediction (grey). It can be seen that grey points are systematically above the black ones. In particular, for  $\langle d \rangle / a \lesssim 0.06$  the normal drag of the particles which exhibit higher values of parallel drag is not compatible with the theoretical LS curve: the viscous

<sup>8</sup>As reported in chapter 3, we indirectly monitored surface contamination by surface tension measurements of the samples in experimental conditions and time scales analogous to our experiment. The test showed that the surface tension remains constant, but since it has not been made for every measured sample we cannot *a priori* exclude accidental contamination of the interface during single experiments.



(a)



(b)

**Figure 5.13:** Adimensional parallel drag  $f_{\parallel}$  measured for SS (a) and CS (b) particles versus the normalized average distance  $\langle d \rangle / a$ . Theoretical predictions refer to slip boundary conditions for a compressible (continuous line) and incompressible (dotted line) interface.

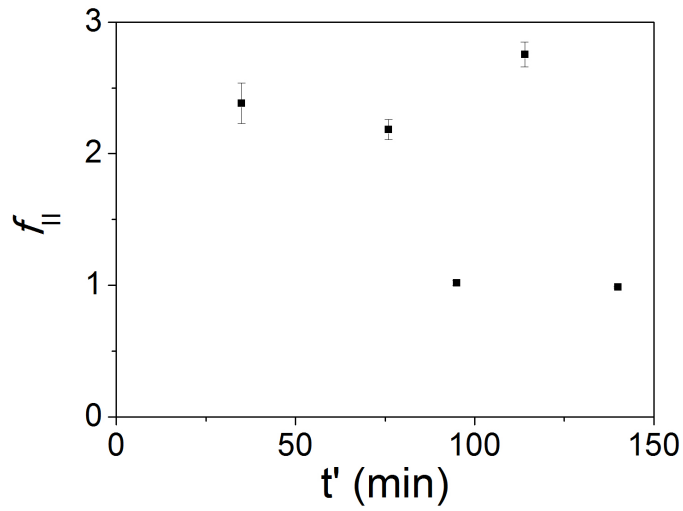


Figure 5.14: Measured adimensional parallel drag for different carboxylated spheres in the same water solution at NaCl molar concentration  $c = 10^{-4}$  M. The values are given as a function time interval  $t'$  between the begin of the experiment and the measurement of the different particles.

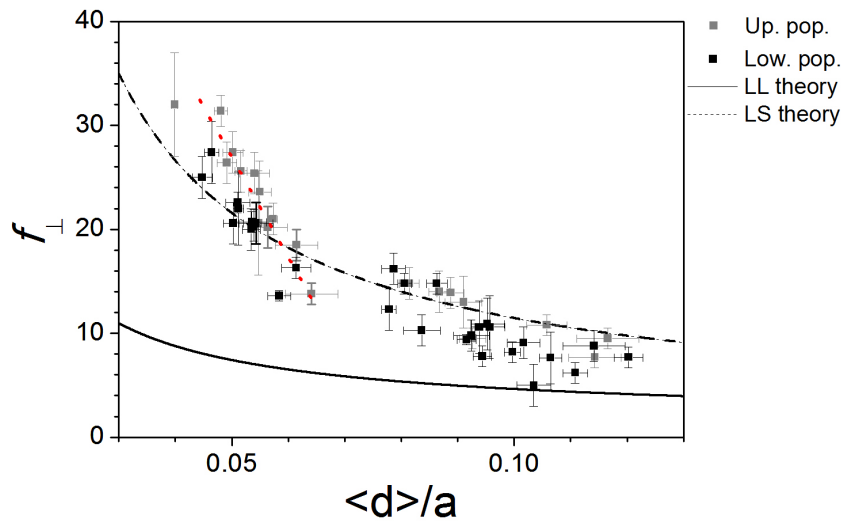


Figure 5.15: Adimensional perpendicular drag measured for sulfate spheres in water solutions at different molarities dividing points belonging to the lower population of fig. 5.9(a) (black) from points belonging to the upper population of fig. 5.9(a) (grey).

drag these particles undergo is even higher than the one they would find approaching to a solid surface. Moreover, the slope of the distribution of such points (dotted line) is more pronounced than the one of predictions.

Such anomaly, affecting both normal and parallel drag of sulfate spheres, is quite surprising and beyond hydrodynamic predictions, as with purely hydrodynamic arguments it is not possible to justify the overcoming of the LS curve. Moreover, its absence for carboxylated spheres, whose main difference with sulfate spheres consists in the lower surface charge, suggests that electrokinetic effects may be involved.

Literature reports models for the electroviscous drag for a sphere moving in liquid bulk (eq. 1.48) and parallel to a solid wall at homogeneous constant surface charge density (eq. 1.51). Nowadays, no predictions exist for the electroviscous drag in the case of the hydrodynamic and electrostatic boundary conditions of the present work.

Because of the complexity of these models, in order to have a first idea of the relevance of electroviscous drag, we made a rough evaluation. We consider a sphere of radius  $4.5 \mu\text{m}$ , with the Zeta potential  $\zeta$  measured in section 4.1 and diffusing in a water solution at the typical molarities of our experiments. The bulk electroviscous drag (BED) evaluated using equation 1.48 is less than 0.1% of the bulk hydrodynamic drag (BHD) and is therefore negligible. The same cannot be said once the spherical particle gets very close to a solid wall: using relation 1.51 the electroviscous drag has been evaluated for a sphere moving parallel to a solid interface at distances from the air-liquid interface in the typical range of the ones of the experiments<sup>9</sup>. The predicted parallel drag increment is in the range of 10-60% of BHD for sulfate particles and of 2-20% of BHD for carboxylated ones. The drag experienced by a particle moving close to a solid wall should be therefore significantly enhanced because of electroviscous drag if the particle is charged. Moreover, for the most charged sulfate spheres such increment is expected to be more pronounced than for the less charged carboxylated ones.

The absence of a model for our peculiar case makes difficult a quantitative comparison with our measurements, but the rough evaluation points out that the electroviscous effect may be relevant in determining the particle dynamics. This is even more true if we consider the increasing of electrokinetic effects passing from no-slip to slip boundary conditions documented in recent works on streaming potential and electro-osmotic flow [147, 148, 149, 150].

In particular, in 2018 Blanc *et al.* [150] studied the flow of surfactants trapped at air-water interface during electro-osmotic experiments. Unexpectedly, they saw that the surfactant layer remained motionless despite the 3D water flow below the interface and parallel to it. They probed such phenomenon down to surfactant concentrations of  $10^{-3}$  cmc and deduced that an unexplained additional friction is exerted on the liquid surface. In common with our experiment, the anomaly affects the liquid displacement parallel to the interface through the suppression of the slip and has an electrokinetic origin. The analogy between the two systems is not complete, but these evidences stress the importance of the still not fully understood electrokinetic effects close to air-liquid interfaces.

---

<sup>9</sup>The surface potential attributed to the interface of the model is the one obtained from the fit of chapter 4. We noticed that surface potentials of that order of magnitude slightly affects the electroviscous drag predicted for the sphere.

## 5.4 Conclusions

In this chapter we reported the results for the parallel and perpendicular drag of spherical particles whose interaction with the air-water interface has been analyzed in chapter 4. The present work is one of the first where the dynamics in both directions with respect to a liquid interface has been explored at high spatial resolution. Moreover, it is the first time that together with the drag also the interaction with the interface has been reported. The coupling of the analysis of particle's dynamics and potential energy allowed us to properly treat the subtle problem of the diffusion in a generic potential. In order to do this, we developed a method to obtain the perpendicular drag coefficient by comparing data and simulations based on the measured interaction. This approach is important to avoid the insurgence of dramatic artefacts arising when data are analyzed under the approximation of harmonic confinement.

The analysis of the drag revealed consistent deviations from hydrodynamic classical theories for the motion close to a full-slip boundary. First, most of the particles are subject to a parallel viscous drag close to the one expected near a liquid-air interface and to a perpendicular viscous drag similar to the one expected near a liquid-solid interface. Apparently, they *see* the air-liquid interface either as a liquid surface or as a solid wall depending on the direction of their motion. Following existing models, such a peculiar behaviour has been rationalized by adding the condition of incompressibility of the interface flow field. This latter can be due either to the presence of impurities at the interface or to the ions responsible for water surface electric charge.

The inclusion of the condition of surface incompressibility does not completely remove the discrepancies between data and expectations. The main question which remains open concerns the anomalous drag measured on a significant number of sulfate spheres. The fact that such anomaly manifests on the most charged spheres and the fact that the correspondent perpendicular drag is slightly higher than the hydrodynamic upper limit suggests that it may be due to electrokinetic phenomena. However, such hypothesis needs further investigations.

## Chapter 6

# Conclusion and outlook

In this thesis, the behaviour of a colloidal particle close to an air-water interface has been experimentally addressed. More specifically, the characterization has been realized for both the interaction energy between the particle and the interface and the viscous drag acting on the particle as it diffuses in the directions parallel and perpendicular to the interface. Finally, the dynamics of particle breaching of the interface has been measured.

In order to track the three-dimensional motion of the particle an adapted dual-Wave Reflection Interference Microscopy (DW-RIM) setup has been developed, made of a low-coherence interferometric system mounted on a custom optical microscope. Proper algorithms have been developed to obtain particle's trajectory from interferometric data. DW-RIM allows overcoming typical limitations of other techniques previously used to study similar systems. In particular, it ensures an high resolution (50 nm in the imaging plane and 10 nm along the optical axis) thus enabling to probe very small particle-interface distances. DW-RIM also allows the determination of the absolute particle-interface distance, making possible the analysis of the data without any assumption on the dynamic properties of the system.

The study of the interaction between a spherical particle and the interface revealed two different potential energy landscapes resulting in two different equilibrium particle-interface distances, both of hundreds of nanometers. The furthest one fairly corresponds to model predictions which take into account van der Waals, double-layers and gravity interactions. The fit of the measured potential provides a value of water surface potential of 1 mV, in the range of the values measured in previous works even if lower in modulus than most of them [4]. This value is found to be independent from the surface charge of the particle.

On the other side, the measured potential closest to the interface shows an additional particle-interface attraction not predicted by the models. The documented partial overlap of such second potential well to the first one implies a double valued potential. This observation, together with the ascertained reversibility of the transition from one equilibrium to the other, suggests that a supplementary degree of freedom is missing in our analysis. A possibility is that the measured additional attraction depends on the orientation of the sphere and thus that it is caused by a particle surface heterogeneity. This heterogeneity may be due to large and thin air-bubbles pinned on the surface of the particle affecting the energy potential of the system.

In order to study the dynamics of a sphere close to the air-water interface without suppressing the informations on the potential energy of the system, the problem of the Brownian diffusion confined in a generic potential has been addressed. It has

been seen that the analysis of the mean square displacements (MSD) through the approximation of an harmonic potential generates huge errors in the measured drag. In order to access the right value of the drag, a simple and refined analysis of the MSD has been developed which takes into account the measured potential and is based on comparison of data with simulations.

The measured drag values have been compared with models differing in the boundary conditions on the air-water interface. Peculiarly, the main trend of the data is partially coherent with boundary conditions which depend on the direction of the particle's motion: the air-water interface acts as a slip boundary for the particle's motion parallel to it and as a no-slip boundary for the particle's motion perpendicular to it. This behaviour, recently predicted [65, 12] but never measured for the same particle, can be explained considering surface incompressibility. Physically, incompressibility can be due either to an extremely weak surface contamination [12], or to the negatively charged ions populating water's surface. In both cases a surface concentration of surface active agents causes a Maragnoni stress which opposes to the surface hydrodynamic flow induced by the particle's motion. Nevertheless, discrepancies remain as large values of both parallel and perpendicular drag cannot be explained considering surface incompressibility alone. Even more, such large measured values cannot be accounted for with purely hydrodynamic boundary conditions. The observed dependence of the drag from particle's electrical charge indicates electrokinetics phenomena, like the electroviscous effect, as possible responsible for these large particle drags.

The presented results open interesting questions and suggest new hypothesis whose verification would be of paramount importance to improve the comprehension of the phenomena leading to interface breaching. The presented results are noteworthy as the size and the surface charge of the studied particles are in the typical range of the ones of commercial microparticles and of micrometric objects present in nature like clays [151, 152], cells [153] and oil in water emulsions [154]. The dynamics close to the air-water interface of these natural colloids and their interface breaching trigger mechanism are relevant in a big number of applications and processes [3]. Furthermore, if the presence of air-bubbles at the particle interface is confirmed, it could shed new light on the long-range hydrophobic interactions, whose nature is still subject of debate in the scientific community.

The choice made in the present thesis has been to study the behaviour of a colloidal particle close to an air-water interface without perturbing the system, in order to have experimental conditions close to the ones present in natural and industrial processes. A further step in this direction would be the extension of the investigation to particles with a shape anisotropy like ellipsoids. As described in chapter 2, the requested tracking algorithms have been already developed. Preliminary measurements verified the capability of the technique to precisely measure all the spatial degrees of freedom of ellipsoidal particles. For illustrative purpose in figure 6.1 are reported the data relative to an ellipsoid of aspect ratio 5 and volume-equivalent radius  $3.9 \mu\text{m}$  while it approaches and breaches the air-water interface. In the figure are reported the gap distance ( $a$ ) and the tilt angle with respect to the interface  $\theta_e$  ( $b$ ) versus time.

Research effort will be also focused on enhancing the comprehension of the unexpected results obtained both on the particle-interface energy potential and on the particle hydrodynamics close to the interface. For the investigation of the additional particle-interface attraction, we plan to verify the angular dependence of the potential by improving the technique enabling also the measurement of particle rotation, using for example optically anisotropic spherical particles coupled with polarized light sources [155]. In parallel to this analysis, the role of the air-bubbles pinned on

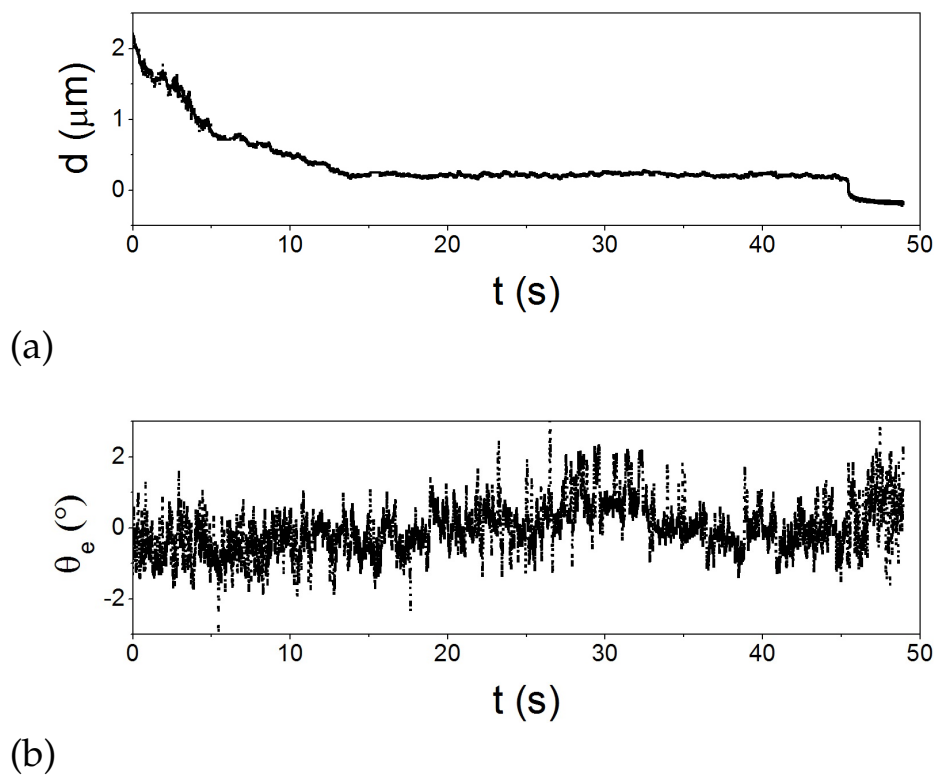


**Figure 6.1:** a) Time evolution of the particle-interface gap distance  $d$  for an PS ellipsoidal particle of aspect ratio 5 and equivalent radius  $3.9 \mu\text{m}$ . Negative values of  $d$  means the particle is partially dewetted. (b) Corresponding time evolution of the ellipsoid tilt angle with respect to the direction normal to the interface  $\theta_e$ .

the particle surface and of eventual other sources of heterogeneities will be inquired by a systematic study of the particle-interface interaction as a function of the coating and the roughness of the surface of the particle.

On the other side, the anomalies on the measured drag can be further investigated by probing the role of electric charges present both on the particle and on the interface. This objective can be pursued by comparing the described drag results with drag measurements in systems where the particle charge is neutralized either by tuning the pH of the aqueous solution at the isoelectric point or by using non-polar solvents. In this last case also the interface with air is expected to remain uncharged.

Finally, in this work the particle-interface distances have been *tuned* by changing the particle and the solution molarity. The drawback of this procedure is that each drag value has been obtained from a different particle. Since the used particles differ in the charge distribution as well as in the size, a systematic characterization of the dynamics of the same particle would help to clarify the occurring phenomena. During this thesis an attempt has been made to build a cell enabling the tuning of the double-layers and gravity interactions while measuring the same particle, by adding a known amount of sodium chloride and deuterium oxide respectively. The measurement proved however to be very difficult because of the long diffusive time needed to have an homogeneous solution. A possible way to improve the statistics and to enhance the comprehension could be a systematic study of the diffusive properties of the same particle restrained into an optical trap. This would allow the measurement of the viscous drag as a function of the particle-interface distance by directly tuning the latter moving the optical trap focus. In a second step the optical trap should be switched off in order to study the potential energy as described in chapter 4. The optical trap can be implemented on the existing setup but problems of calibration and of retaining force have to be solved before starting the data collection.

# Notations

## Acronyms and abbreviations

AFM	Atomic Force Microscopy
CS	carboxylated spheres
DI	deionized (water)
DL	Double layer
DLS	dynamic light scattering
DVM-3D	Three-dimensional digital video microscopy
DW-RIM	Dual Wave Reflection Interference Microscopy
FFT	Fast Fourier Transform
LA	Liquid-air (boundary conditions)
LED	Light-emitting diode
LRHF	Long-Range Hydrophobic Force
LS	Liquid-solid (boundary conditions)
PB	Poisson-Boltzmann (equation)
PVA	Poly(vinyl alcohol)
RICM	Reflection Interference Contrast Microscopy
RLM	Reflected light microscopy
ROI	Region of Interest
SEM	Scanning Electron Microscopy
SFA	Surface Force Apparatus
SS	Sulfate spheres
TFPB	Thin Film Pressure Balance
TIRM	Total internal reflection microscopy
TLM	Transmitted light microscopy

## Physical quantities and constants

### Optics

$\alpha_{coll}$	One-half angular aperture of the objective
$\alpha_{lim}$	Maximum reliable collecting angle
$\lambda_R, \lambda_B$	Wavelengths of the LED illumination sources
$N_A$	Numerical aperture of the microscope objective $N_A = n \sin \alpha_{coll}$
$n_1$	Refractive index of the medium containing the particle (water)
$n_2$	Refractive index of the second medium (air)
$z_R$	Rayleigh range
$w_0$	Waist radius

**Geometry**

$\theta$	Polar angle in the particle's reference system
$\theta_e$	Tilt angle between the normal to water surface and the minor semiaxis of the ellipsoid
$\theta_s$	Sphere's tilt angle
$\theta'$	Contact angle with the solution of a trapped spherical particle
$\Lambda$	Mechanical elongation on the sphere for ellipsoid's fabrication $\Lambda = S_a/a$
$\varphi$	Azimuthal angle in the particle's reference system
$\varphi_e$	Ellipsoid's orientation in the $xy$ plane
$a$	Particle's radius
$A$	Average area of particle's surface defects
$Ar$	Ellipsoid's aspect ratio $S_a/S_b$
$d$	Gap distance between the particle and the air-water interface
$d_0$	Equilibrium $d$
$\langle d \rangle$	Average value of $d$
$\hat{e}_{\parallel}, \hat{e}_{\perp}$	unit vectors
$\tilde{h}$	Ratio between $z_c$ and $a$
$\tilde{h}$	Height of the convex part of the drop in its center
$R(x, y, z)$	Distance from particle's center
$r$	Projection of $R$ on the AW interface $r = [(x - x_c)^2 + (y - y_c)^2]^{1/2}$
$S_a$	Ellipsoid's major semiaxis
$S_b$	Ellipsoid's minor semiaxis
$(x_c, y_c, z_c)$	Particle's center coordinates
$(x_o, y_o, d)$	Coordinates of the point of particle's surface closer to water surface $(x_o, y_o, d) = (x_c, y_c, z_c - a)$ for the sphere
$(x', y')$	Axes of the Cartesian coordinate system solidal to the ellipsoid

## Fluidodynamics

$\eta_1$	Viscosity of the medium containing the particle (water solutions)
$\eta_2$	Viscosity of the second medium (air)
$\eta_d$	Dilatational interface viscosity
$\eta_{sh}$	Shear interface viscosity
$\nu$	Particle's frequency for its motion $\perp$ to the interface
$\nu_0$	Characteristic frequency in the model of Maali <i>et al.</i>
$\xi_{ev}$	Electroviscous drag coefficient
$\xi_x, \xi_y, \xi_z$	Particle's drag coefficients along the three axes
$\xi_{\parallel}$	Particle's drag coefficient in the direction $\parallel$ to the interface
$\xi_{\perp}$	Translational drag coefficient in the direction $\perp$ to the interface
$\xi_{\infty}$	Translational drag coefficient in unbounded fluid
$\xi_{\omega}$	Rotational viscous drag coefficient
$\Pi$	Surface 2D pressure due to active species
$\rho_1$	Density of medium 1 containing the particle
$\rho_2$	Density of medium 2 (air)
$\rho_{col}$	Density of the particle
$\tau_B$	Relaxation time of the particle velocity
$\vec{\omega}$	Angular velocity
$\vec{\Omega}$	Torque
$c$	Molar concentration of both NaCl and HCl in the solution
$c_s^i$	Surface concentration of active species
$D_i$	Diffusion coefficient of the ionic species $i$
$D_x, D_y, D_z$	Particle's diffusion coefficients along the three axes
$D_s$	Interfacial diffusion coefficient of active species
$f_{\parallel}$	Adimensional parallel drag coefficient
	$f_{\parallel} = \xi_{\parallel}/\xi_{\infty}$
$f_{\perp}$	Adimensional perpendicular drag coefficient
	$f_{\perp} = \xi_{\perp}/\xi_{\infty}$
$\vec{F}_v$	Friction force
$\vec{F}_r$	Random force acting on the diffusing particle
$g$	Gravity acceleration
$m$	Particle mass
$m^*$	Reduced particle mass considering buoyancy
	$m^* = 4/3\pi a^3 (\rho_p - \rho_1)$
$P$	Hydrodynamic pressure
$Pe$	Peclet number
$\tilde{r}$	Ratio between the drag obtained from the fit of the MSD of a simulation and the input drag of the simulation
$Re$	Reynolds number
$\vec{v}_l$	Hydrodynamic lift velocity
$\vec{v}_s$	2D Flow velocity at the interface

## Energy interactions

$\epsilon$	Relative permittivity
$\epsilon_0$	Vacuum permittivity ( $8.854187 \cdot 10^{-12}$ C/m·V)
$\zeta$	Zeta Potential
$\lambda_D$	Debye screening length
$\mu_i$	Chemical potential of the ionic species $i$
$\rho_q$	Volume density of charge
$\Sigma$	Conductivity
$\Sigma_M$	Molar conductivity
$\sigma_q$	Particle's surface charge
$\psi$	Electric potential
$\psi_0$	Surface electric potential
$\psi_{AL}$	Air-water surface electric potential
$A_H$	Hamaker Constant
$e$	Modulus of the electron charge ( $1.602 \cdot 10^{-19}$ C)
$n_i$	Number density of the ionic species $i$
$n_i^0$	Bulk number density of the ionic species $i$
$j_i$	Valency of the ionic species $i$
$k$	Debye-Hückel parameter ( $k = 1/\lambda_D$ )
$U(d)$	Potential energy of the particle-interface system
$U^{\sigma-\sigma}$	DL potential energy: 2 objects at constant surface charge
$U^{\psi-\psi}$	DL potential energy: 2 objects at constant surface potential
$U^{\psi-\sigma}$	DL potential energy: 2 objects with mixed boundary conditions

## Various

$\gamma$	Surface tension between the liquid and air
$\gamma_{lm}$	Surface tension between two phases $l$ and $m$
$L$	Avogadro constant ( $6.022 \cdot 10^{23}$ )
$k_B$	Boltzmann constant ( $1.3806 \cdot 10^{-23}$ N·m/K)
$T$	Temperature

# Appendix A

## Basics of optics and microscopy

### A.1 Beam properties

The Rayleigh range  $z_R$  of a light beam is the distance from the beam waist (in the propagation direction) where the beam radius is increased by a factor of the square root of 2. For Gaussian beams, the Rayleigh range is determined by the waist radius  $w_0$  and the wavelength  $\lambda$ :

$$z_R = \frac{\pi w_0^2}{\lambda} \quad (\text{A.1})$$

The Rayleigh range can be taken as an estimate of the depth of focus of the beam, *i.e.* the distance along the optical axis over which the beam can be considered focused. In an imaging system, two objects at two different positions will be focused in the meantime if the distance between the focal planes is equal or smaller than the depth of focus.

The waist radius is inversely proportional to the amplitude of the cone of light coming from the objective. Defining  $\alpha_{coll}$  one-half of the angular aperture of the objective, its relation with the  $w_0$  is:

$$w_0 = \frac{\lambda}{\pi \alpha_{coll}} \quad (\text{A.2})$$

Using equations A.1 and A.2, and using the definition of numerical aperture for a microscope objective ( $N_A = n \sin \alpha_{coll}$ ), we obtain:

$$z_R = \frac{\lambda}{\pi \alpha_{coll}^2} = \frac{\lambda}{\pi \arcsin \alpha_{coll}^2} \quad (\text{A.3})$$

Evaluating eq. A.3 for the objective and the wavelengths used in our setup, we find a Rayleigh range of the order of 0.4-0.5  $\mu\text{m}$ , close to the nominal depth of focus of the objective (0.6  $\mu\text{m}$ ). This was expected because the depth of focus, given as a technical specification of the objective, is a rough estimation of the Rayleigh range neglecting the  $\lambda$  dependency.

### A.2 Interference calculations

In this section the derivation of an expression for the fringe system generated by the interference of the light reflected by a flat interface with the one reflected by a sphere is given.

As explained in 2.1.3, the difference in the optical path of the two reflected beams arises in first approximation from the double of the optical path between the particle and the interface, in the direction normal to the interface. The used coordinate system (fig. A.1(a)) is cylindrical with  $r = \sqrt{x^2 + y^2}$  lying on the plane of the air-water interface, and with the  $z$  axis directed versus the medium containing the particle. The origin of the system has been put on the interface in correspondence of the projection of the center of the sphere. Because of the polar symmetry, everything is independent from the azimuthal angle  $\varphi$ .

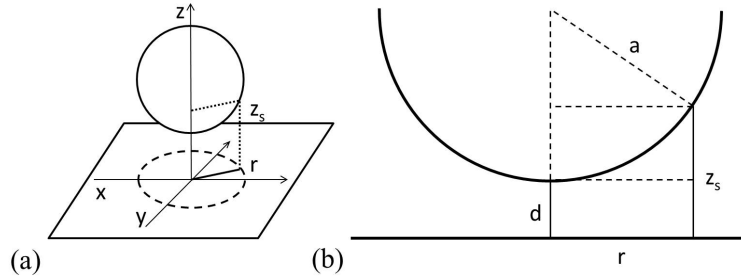


**Figure A.1:** (a) Cylindrical coordinate system. (b) Geometry for the evaluation of the optical paths.

In fig.A.1(b) the simple geometry of the problem is illustrated. Defining  $z_s(r)$  a generic point on the sphere's surface, its value is equal to the distance  $d$  plus a quantity dependent from  $r$ :

$$z_s(r) = d + \left( a - \sqrt{a^2 - r^2} \right) \quad (\text{A.4})$$

The additional optical path travelled by the beam reflected by the sphere is therefore  $2z_s$ .

The interference pattern can be now calculated by the square of the total field:

$$\begin{aligned} I &\propto |E_{awi,0} + E_{col,0} \exp\{-2ikz_s\}|^2 \\ I &\propto E_{awi,0}^2 + E_{col,0}^2 + 2E_{awi,0}E_{col,0} \cos 2kz_s \end{aligned} \quad , \quad (\text{A.5})$$

where  $E_{awi,0}$  and  $E_{col,0}$  are the amplitudes of the fields coming respectively from the air-water interface and from the colloid and with  $k = \frac{2n_1\pi}{\lambda}$  being the wave number. The phase equal to zero has been chosen to be the one of the field reflected from the water interface. If the two initial field amplitudes are equal we get:

$$I = 2I_0 (1 + \cos 2kz_s) \quad (\text{A.6})$$

The final expression 2.4 is finally obtained by replacing  $k$  and the equation A.4 in equation A.6.

## Appendix B

# Evolution of tracking algorithms

### B.1 Evolution of the algorithm for spheres' tracking

During the present work different methods have been tested, weighing up their efficiency and velocity. Here below I will list the main attempts we tried that didn't reach the requested precision and versatility. Their weaknesses and the way they failed brought us to the final solution of the 2D fit described in chapter 1.

- **search for the center of mass:** The ROI is binarized using as a threshold given by the mean value of the intensity times a factor between 0 and 2, depending on the contrast of the video. Without noise what it is expected in that the binary image is made of a series of objects representing concentric rings corresponding to the maxima of the fringe pattern. However, the presence of the noise caused the objects to be not close but mincing knife-shaped. The program look for the center of mass of the binary matrix. In the ideal case it corresponds to the coordinates of the center of the sphere in the plane, but in practice what remains of the asymmetry due to illumination together with all the noise shift the center of mass away from the geometrical center of the fringe system. This is the fastest method but also the one which gives the worst result, missing the correct value by several hundreds of nm.
- **search for peaks and valleys:** Due to the circular symmetry of the interference pattern its center has to be a relative maximum or minimum. This method starts from this and looks for all the extrema in the ROI. Then it identifies the center as the extremum closer to the center found in the previous frame (input center). Also in that case the noise makes however the method ineffective.
- **best circumference:** The idea of this method comes trying to solve the mincing knife problem encountered in the method of the center of mass: instead of taking all the pixels of the binarized image, here these pixels are grouped in objects: an amount of connected pixel higher than a defined threshold is considered as an object, which can have a certain number of holes (a group of connected pixels equal to zero). Among the objects with one hole (which should be good circular maxima) the one closer to the input center and with the lower diameter is selected and its center of mass is taken as the output center.
- **circumferences fit:** After seeing that the previous technique misses the goal since the identification of the objects with the fringes doesn't work properly,

this evolution of the method as been tried. The binarized image of the ROI is taken and its azimuthal average is evaluated (the considered center for the average is the input one) and its histogram is plotted as a function of the radial distance (fig. B.1(a)). On this function the maxima are found and each one of them is identified with an annulus in the binarized image. Its borders are the half distances from the confining annuli in the histogram. After the objects are identify in this way, each one of them is considered as a set of coordinates  $x, y$  and is separately fitted with a circle. From the subset of circles with their centres at a reasonable distance from the input one, a mean center is evaluated and given as the output. In figure B.1(b) an example is given, where the green and blue fitted circles are good, while the red one is wrong and rejected from the average computation. Such method represents an improvement but the precision in determining the enter is still low.

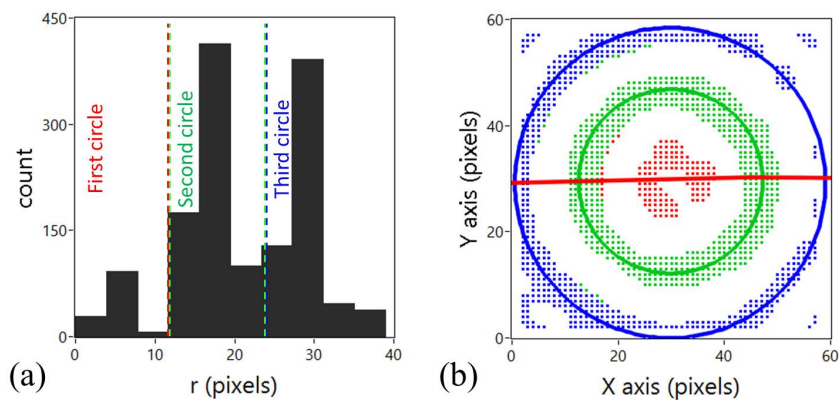


**Figure B.1:** Example of two passages of the circumferences fit method to find the center of the sphere: on the histogram of the azimuthal average of the binary image (a) the different circles are distinguished, then each one of them is fitted with a circle (b). In (b) it can be seen that the fit of the red object doesn't give a reasonable center (located far below the image, outside from the field of view) and therefore it is rejected.

What the listed methods pointed out is that passing from the binary image is not the best option for the individuation of the center. Binarization is a valid option with imaging data, where the object is all brighter or all darker than the background and so it can be easily identified with a threshold. But here the object is an interferometry pattern with a lot of maxima and minima and all the shades of gray between them. This consideration drove us to directly consider the un-binarized frame.

## Appendix C

# Contributions to the experimental error

### C.1 Error on the radial coordinate arising from the azimuthal average

As reported in section 2.2.1 the precision on the determination of  $x_c$  and  $y_c$  for a sphere is 0.05 nm. As a consequence, when the intensity profile is extracted from the frame averaging  $I$  over the azimuthal angle, the center is shifted in  $xy$  by  $\delta_{xy} = \sqrt{\delta_x^2 + \delta_y^2}$ , with both  $\delta_x$  and  $\delta_y$  between 0 and  $\sigma_x$ . Let's here consider for simplicity  $\delta_{xy} = \delta_x$ <sup>1</sup>. We want to evaluate the radial coordinates  $r$ , after the azimuthal average, where we will find an extremum which is at a distance  $r_e$  from the true center of the interference fringe system (figure C.1).

Centring the Cartesian reference system on the found  $x_c y_c$  coordinates, the equation for the circumference describing the extremum coordinates is given by:

$$(x - \delta_x)^2 + y^2 = r_e^2 \quad (\text{C.1})$$

If we pass to polar coordinates  $r\varphi$  the equation becomes

$$(r \cos \varphi - \delta_x)^2 + (r \sin \varphi)^2 = r_e^2 \quad (\text{C.2})$$

The radial coordinate of the extremum as a function of  $\varphi$  is therefore:

$$r = \delta_x \cos \varphi + \sqrt{\delta_x \cos \varphi^2 - \delta_x^2 + r_e^2} \quad (\text{C.3})$$

It can be averaged over all the angles to find the average coordinate of the extremum  $\tilde{r}_e$

$$\tilde{r}_e = \frac{1}{2\pi} \int_0^{2\pi} \delta_x \cos \varphi + \sqrt{\delta_x \cos \varphi^2 - \delta_x^2 + r_e^2} d\varphi \quad (\text{C.4})$$

$$= 0 + \frac{\delta_x}{2\pi} \int_0^{2\pi} \sqrt{-\sin \varphi^2 + \frac{r_e^2}{\delta_x^2}} d\varphi \quad (\text{C.5})$$

---

<sup>1</sup>This can be done because the error is independent from an arbitrary rotation of the  $xy$  reference system.

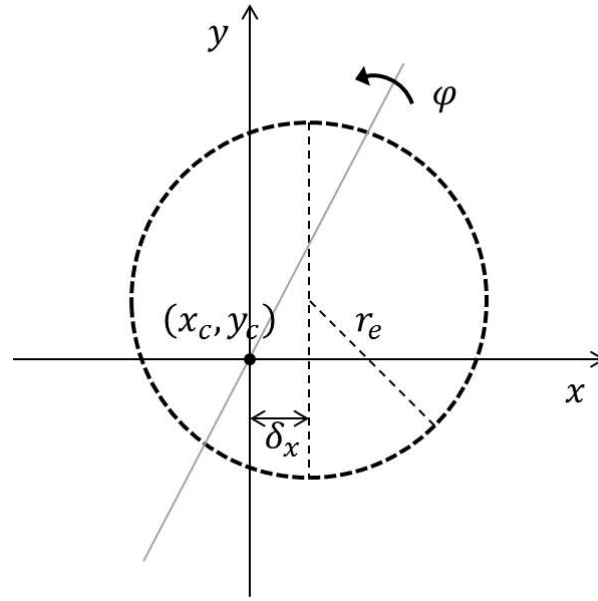


**Figure C.1:** Sketch of the reference system centered on the found  $x_c y_c$  couple at a distance  $\delta_x$  from the correct center. The circumference represent the considered fringe for the evaluation of its position in the decentered reference system.

This is the formula 2.10 reported in section 2.2.2.

## C.2 Frequency spectrum width's contribution

Another experimental deviation from the ideal case is given by the small polychromatic feature of the light beam: the LED's spectrum has a certain width, characterized by its FWHM. The beam is therefore made of a combination of several wavelengths, each one with its own interference pattern. They form a continuum spectrum with a shape that can be approximated with a Gaussian (figure 2.5). Since the spectrum is very narrow the interference pattern is very similar to the monochromatic one. However, for safety at the beginning of the work an evaluation has been made of the error introduced by this effect.

The passage from a single wavelength to the Gaussian spectrum implies the following transformations of the two electric fields reflected by the two surfaces:

Monochromatic	Gaussian spectrum
$E^{awi} = E_0^{awi}$	$\rightarrow \int_{-\infty}^{+\infty} \frac{1}{\sigma_k \sqrt{2\pi}} e^{-\frac{(k-k_0)^2}{2\sigma_k^2}} dk$
$E^{col} = E_0^{col} e^{-2ik_0 z(r)}$	$\rightarrow \int_{-\infty}^{+\infty} \frac{1}{\sigma_k \sqrt{2\pi}} e^{-\frac{(k-k_0)^2}{2\sigma_k^2}} e^{-2ikz_s} dk$

Where  $k_0$  is the peak value of the spectrum (635 nm and 505 nm for the two wavelengths),  $\sigma_k$  here is used to indicate the width of the spectrum and  $z_s$  is the vertical coordinate of a point of the particle's surface (it is a function of  $x$  and  $y$ ).

From the fields it is possible to get the total intensity on the camera's sensor:

$$I(x, y) = I_0 \left| \int_{-\infty}^{+\infty} e^{-\frac{(k-k_0)^2}{2\sigma_k^2}} (1 + e^{-2ikz_s}) dk \right|^2 \quad (\text{C.6})$$

The square complex modulus can be brought inside the integral symbol because the different wavelengths don't interfere with each other: the only interference is the one between the couples of reflected beams with the same wavelength. The physical reason is that different wavelengths are incoherent with each other because of the low coherence length, much shorter than the total optical path. The absence of temporal coherence therefore makes the double product vanish between different wave numbers but at the same time keeps the ones between the two reflected beams at a fixed wave number. The final intensity is therefore:

$$\begin{aligned} I(x, y) &= I_0 \int_{-\infty}^{+\infty} \left| e^{-\frac{(k-k_0)^2}{2\sigma_k^2}} (1 + e^{-2ikz_s}) \right|^2 dk \\ &= 2I_0 \int_{-\infty}^{+\infty} e^{-\frac{(k-k_0)^2}{\sigma_k^2}} (1 - \cos(2kz_s)) dk \end{aligned} \quad (\text{C.7})$$

The plot of  $I(x, y)$  has been made both for the red and the blue wavelength using their correspondent  $\sigma_\lambda$  of 10 and 16 nm respectively. It has been found that the deviation on the position of the maxima and minima with respect to the monochromatic formula is always lower than 3 nm (see figure C.2), corresponding to an error on  $d$  which is always subnanometric and therefore negligible.

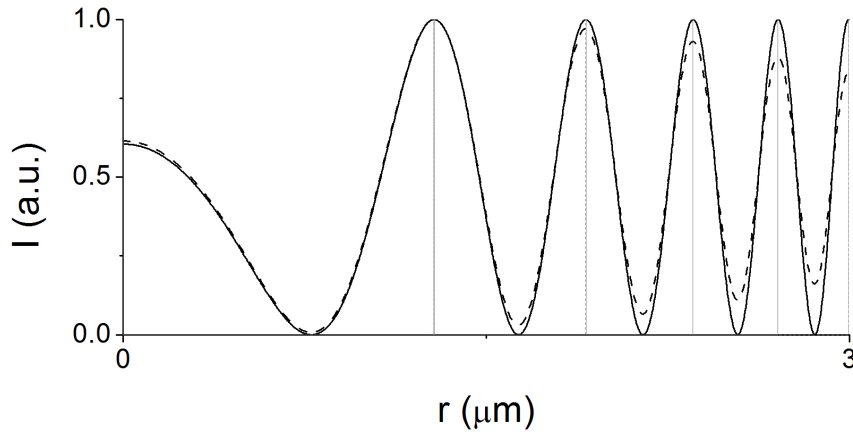


**Figure C.2:** Profile along  $r$  of the expected interference pattern for a sphere ( $a = 4.5 \mu\text{m}$ ) illuminated by a monochromatic source at 635 nm (black continuous line) superimposed to the profile along  $r$  of the expected interference pattern for the same sphere illuminated by a source with a peak intensity for  $\lambda = 635 \text{ nm}$  and a gaussian power spectrum with  $\sigma_\lambda = 10 \text{ nm}$  (black dashed line). The grey vertical lines highlight the maxima positions.



# Bibliography

- [1] Aristotele, "Metaphysics", book 1, section 983b.
- [2] P. Ball, "Water - an enduring mystery", *Nature*, **452**, 291-292 (2008).
- [3] Y. Xing, X. Gui, L. Pan, B. Pinchasik, Y. Cao, J. Liu, M. Kappl and H. Butt, "Recent experimental advances for understanding bubble-particle attachment in flotation", *Adv. Coll. Int. Sci.*, **246**, 105-132 (2017).
- [4] R. A. Pushkarova and R. G. Horn, "Bubble-Solid Interactions in Water and Electrolyte Solutions", *Langmuir*, **24**, 8726-8734 (2008).
- [5] L. A. Del Castillo, S. Ohnishi, S. L. Carnie and R. G. Horn, "Variation of Local Surface Properties of an Air Bubble in Water Caused by Its Interaction with Another Surface", *Langmuir*, **32**, 7671-7682 (2016). DOI: 10.1021/acs.langmuir.6b01949
- [6] E. Taran, M. A. Hampton, A. V. Nguyen and P. Attard, "Anomalous Time Effect on Particle-Bubble Interactions Studied by Atomic Force Microscopy", *Langmuir*, **25**, 2797-2803 (2009).
- [7] R. F. Tabor, F. Grieser, R. R. Dagastine and D. Y. C. Chan, "Measurement and Analysis of Forces in Bubble and Droplet Systems Using AFM", *J. Coll. Int. Sci.*, **371**, 1-14 (2012).
- [8] L. Helden, K. Dietrich and C. Bechinger, "Interactions of Colloidal Particles and Droplets with Water–Oil Interfaces Measured by Total Internal Reflection Microscopy", *Langmuir*, **32** (51), 13752-13758 (2016).
- [9] G. M. Wang, R. Prabhakar and E. M. Sevick, "Hydrodynamic Mobility of an Optically Trapped Colloidal Particle near Fluid-Fluid Interfaces", *Phys. Rev. Lett.*, **103**, 248303 (2009).
- [10] T. Watarai and T. Iwai, "Direct observation of submicron Brownian particles at a solid–liquid interface by extremely low coherence dynamic light scattering", *App. Phys. Express*, **7** 3, 032502 (2014).
- [11] J. C. Benavides-Parra, D. Jacinto-Méndez, G. Brotons, M. D. Carbajal-Tinoco, "Brownian motion near a liquid-gas interface", *J. Chem. Phys.*, **145**, 114902 (2016).
- [12] A. Maali, R. Boisgard, H. Chraïbi, Z. Zhang, H. Kellay and A. Würger, "Viscoelastic Drag Forces and Crossover from No-Slip to Slip Boundary Conditions for Flow near Air-Water Interfaces", *Phys. Rev. Lett.*, **118**, 1-5 (2017).
- [13] O. Bonhomme, B. Blanc, L. Joly, C. Ybert and A. Biance, "Electrokinetic transport in liquid foams", *Adv. Coll. Int. Sci.*, **247**, 477-490 (2017).

- [14] D. M. Kaz, R. McGorty, M. Mani, M. P. Brenner and V. N. Manoharan, "Physical ageing of the contact line on colloidal particles at liquid interfaces", *Nature Materials*, **11**, 138-142 (2012).
- [15] M. Chaplin, "Theory vs experiment: what is the surface charge of water", *Water*, **11**, 1-28 (2009).
- [16] J. N. Israelachvili, "Intermolecular and surface forces", 2<sup>nd</sup> edition, Academic Press, 1992.
- [17] R. J. Hunter, "Foundations of Colloid Science", Oxford University Press, Oxford (2001).
- [18] J. Perrin, "Mécanisme de l'électrisation de contact et solutions colloïdales", *J. Chim. Phys.*, **2**, 601-651 (1904).
- [19] M. Gouy, "Sur la constitution de la charge électrique à la surface d'un électrolyte" *J. Phys. Theor. Appl.*, **9** 1, 457-468 (1910).
- [20] D. L. Chapman, "LI. A contribution to the theory of electrocapillarity" *The London, Edinburgh, and Dublin philosophical magazine and journal of science*, **25** 148, 475-481 (1913).
- [21] G. Kar, S. Chander and T. S. Mika, "The Potential Energy of Interaction Between Dissimilar Electrical Double Layers", *J. Coll. Int. Sci.*, **44** 2, 347-355 (1973).
- [22] E. J. W. Verwey and J. T. G. Overbeek, "Theory of the Stability of Lyophobic Colloids", Elsevier, Amsterdam (1948).
- [23] R. Hogg, T. W. Healy and D. W. Fuerstenau, "Mutual coagulation of colloidal dispersions", *Trans. Faraday Soc.*, **62**, 1638-1651 (1966).
- [24] G. R. Wiese and T. W. Healy, "Effect of particle size on colloid stability", *Trans. Faraday Soc.*, **66**, 490-499 (1970).
- [25] A. Graciaa, P. Creux and J. Lachaise, "Electrokinetics of gas bubbles", *Surfactant science series*, Dekker (2002).
- [26] S. Usui, H. Sasaki and H. Matsukawa, "The dependence of zeta potential on bubble size as determined by the dorn effect", *J. Coll. Int. Sci.*, **81** 1, 80-84 (1981).
- [27] K. Okada, Y. Akagi, M. Kogure and N. Yoshioka, "Effect on surface charges of bubbles and fine particles on air flotation process", *Can. J. Chem. Eng.*, **68**, 393-399 (1990).
- [28] G. L. Collins, M. Motarjemi and G. J. J. Jameson, "A method for measuring the charge on small gas bubbles", *J. Coll. Int. Sci.*, **63** 1, 69-75 (1978).
- [29] M. Corti, M. Bonomo and A. Raudino, "New interferometric technique to evaluate the electric charge of gas bubbles in liquids", *Langmuir*, **28**, 6060-6066 (2012).
- [30] C. Stubenrauch and R. Von Klitzing, "Disjoining pressure in thin liquid foam and emulsion films—new concepts and perspectives", *J. Phys.: Condens. Matter*, **15** 27, R1197 (2003).
- [31] D. Exerowa, N. V. Churaev, T. Kolarov, N. E. Esipova, N. Panchev and Z. M. Zorin, "Foam and wetting films: electrostatic and steric stabilization", *Adv. Coll. Int. Sci.*, **104**, 1-24 (2003).

- 
- [32] W. A. Ducker, Z. Xu and J. N. Israelachvili, "Measurements of hydrophobic and DLVO forces in bubble-surface interactions in aqueous solutions", *Langmuir*, **10** 9, 3279-3289 (1994).
- [33] L. M. Levering, M. R. Sierra-Hernandez and H. C. Allen, "Observation of hydronium ions at the air-aqueous acid interface: Vibrational spectroscopic studies of aqueous HCl, HBr, and HI", *J. Phys. Chem. C*, **111** 25, 8814-8826 (2007).
- [34] M. Sovago, R. K. Campen, G. W. Wurpel, M. Müller, H. J. Bakker and M. Bonn, "Vibrational response of hydrogen-bonded interfacial water is dominated by intramolecular coupling", *Phys. Rev. Lett.*, **100** 17, 173901 (2008).
- [35] K. G. Marinova *et al.*, "Charging of oil-water interfaces due to spontaneous adsorption of hydroxyl ions", *Langmuir*, **12** 8, 2045-2051 (1996).
- [36] Beattie, James K. "The intrinsic charge at the hydrophobe/water interface." *Colloid Stability* (2010): 153-164.
- [37] M. Takahashi, " $\zeta$  potential of microbubbles in aqueous solutions: electrical properties of the gas-water interface", *J. Phys. Chem. B*, **109** 46, 21858-21864 (2005).
- [38] R. Zimmermann, S. Dukhin and C. Werner, "Electrokinetic measurements reveal interfacial charge at polymer films caused by simple electrolyte ions", *J. Phys. Chem. B*, **105** 36, 8544-8549 (2001).
- [39] L. R. Pratt and A. Pohorille, "Hydrophobic effects and modelling of biophysical aqueous solution interfaces", *Chem. Rev.*, **102**, 2671-2692 (2002).
- [40] M. G. Brown, D. S. Walker, E. A. Raymond and G. L. Richmond, "Vibrational sum-frequency spectroscopy of alkane/water interfaces: Experiment and theoretical simulation", *J. Phys. Chem. B*, **107** 1, 237-244 (2003).
- [41] S. I. Mamatkulov, P. K. Khabibullaev and R. R. Netz, "Water at hydrophobic substrates: curvature, pressure, and temperature effects", *Langmuir*, **20** 11, 4756-4763 (2004).
- [42] X. Yan *et al.*, "Central Role of Bicarbonate Anions in Charging Water/Hydrophobic Interfaces", *J. Phys. Chem. Lett.*, **9**, 96-103 (2018).
- [43] H. C. Hamaker, "The London-van der Waals attraction between spherical particles.", *Physica*, **4**, 1058-1072 (1937).
- [44] E. M. Lifshitz, "Theory of molecular attractive forces", *Soviet Phys. JETP*, **2**, 73-83 (1956).
- [45] D. Bonn, J. Eggers, J. Indekeu, J. Meunier and E. Rolley, "Wetting and spreading", *Rew. Modern Phys.*, **81**, 739-805 (2009).
- [46] D. B. Hough and L. R. White, "The calculation of Hamaker constants from Lifshitz theory with applications to wetting phenomena." *Adv. Coll. Int. Sci.*, **14**, 3-41 (1980).
- [47] H. D. Ackler, R. A. French and Y. Chiang, "Comparisons of Hamaker Constants for Ceramic Systems with Intervening Vacuum or Water: From Force Laws and Physical Properties", *J. Coll. Int. Sci.*, **179**, 460-469 (1996).

- [48] V. Médout-Marère, "A simple experimental way of measuring the Hamaker constant  $A_{11}$  of divided solids by immersion calorimetry in apolar liquids.", *J. Coll. Int. Sci.*, **228** 2, 434-437 (2000).
- [49] M. A. Bevan and D. C. Prieve, "Direct Measurement of Retarded van der Waals Attraction", *Langmuir*, **15**, 7925-7936 (1999).
- [50] K. A. Karraker and C. J. Radke, "Disjoining Pressures, Zeta Potentials and Surface Tensions of Aqueous Non-Ionic Surfactant/Electrolyte, Solutions: Theory and Comparison to Experiment", *Adv. Coll. Int. Sci.*, **96**, 231-64 (2002).
- [51] S. I. Karakashev, P. T. Nguyen, R. Tsekov, M. A. Hampton and A. V. Nguyen, "Anomalous Ion Effects on Rupture and Lifetime of Aqueous Foam Films Formed from Monovalent Salt Solutions up to Saturation Concentration", *Langmuir*, **24**, 11587-11591 (2008).
- [52] V. V. Yaminsky, S. Ohnishi, E. A. Vogler and R. G. Horn, "Stability of Aqueous Films Between Bubbles. Part 1. The Effect of Speed on Bubble Coalescence in Purified Water and Simple Electrolyte Solutions", *Langmuir*, **26**, 8061-8074 (2010).
- [53] R. M. Pashley and J. A. Kitchener, "Surface Forces in Adsorbed Multilayers of Water on Quartz", *J. Coll. Int. Sci.*, **71**, 491-500 (1979).
- [54] D. Beaglehole and H. K. Christenson, "Vapor Adsorption on Mica and Silicon: Entropy Effects, Layering, and Surface Forces", *J. Phys. Chem.*, **96**, 3395-3403 (1992).
- [55] L. R. Fisher, E. E. Mitchell, D. Hewitt, J. Ralston and J. Wolfe, "The Drainage of a Thin Aqueous Film Between a Solid Surface and an Approaching Gas Bubble", *Colloids Surf.*, **52**, 163-174 (1991).
- [56] L. D. Landau and E. M. Lifshitz, "Fluid Mechanics: Landau and Lifshitz: Course of Theoretical Physics", volume 6, Elsevier (2013).
- [57] H. Brenner, "The slow motion of a sphere through a viscous fluid towards a plane surface", *Chem. Eng. Sci.*, **16**, 242-251 (1961).
- [58] A. J. Goldman, R. G. Cox and H. Brenner, "Slow viscous motion of a sphere parallel to a plane wall — II Couette flow", *Chem. Eng. Sci.*, **22**, 653-660 (1967).
- [59] A. V. Nguyen and G. M. Evans, "Exact and global rational approximate expressions for resistance coefficients for a colloidal solid sphere moving in a quiescent liquid parallel to a slip gas-liquid interface", *J. Coll. Int. Sci.*, **273**, 262-270 (2004).
- [60] E. Lauga and T. M. Squires, "Brownian motion near a partial-slip boundary: A local probe of the no-slip condition", *Phys. Fluids*, **17** 10, 103102 (2005).
- [61] M. J. Boussinesq, "Sur l'existence d'une viscosité superficielle, dans la mince couche de transition separant un liquide d'une autre fluide contigue", *Ann. Chim. Phys.*, **29**, 349-357 (1913).
- [62] L. E. Scriven, "Dynamics of a Fluid Interface", *Chem. Engng Sci.*, **12**, 98-108 (1960).
- [63] A. M. J. Davis and M. E. O'Neill, "The slow rotation of a sphere submerged in a fluid with a surfactant surface layer", *Int. J. Mult. Flow*, **5** 6, 413-425 (1979).

- [64] K. D. Danov, T. D. Gurkov, H. Raszillier and F. Durs, "Stokes flow caused by the motion of a rigid sphere close to a viscous interface", *Chem. Eng. Sci.*, **53** 19, 3413-3434 (1998).
- [65] J. Bławzdziwicz, M. L. Ekiel-Jeżewska, and E. Wajnryb, "Motion of a spherical particle near a planar fluid-fluid interface: The effect of surface incompressibility", *J. Chem. Phys.*, **133** 11, 114702 (2010).
- [66] O. Manor, I.U. Vakarelski, X. Tang, S. J. O'Shea, G.W. Stevens, F. Grieser, R. R. Dagastine and D.Y. C. Chan, "Hydrodynamic boundary conditions and dynamic forces between bubbles and surfaces", *Phys. Rev. Lett.*, **101**, 024501 (2008).
- [67] O. Manor, I.U. Vakarelski, G.W. Stevens, F. Grieser, R. R. Dagastine and D.Y. C. Chan, "Dynamic forces between bubbles and surfaces and hydrodynamic boundary conditions", *Langmuir*, **24**, 11533-11543 (2008).
- [68] G. D. M MacKay and S. G Mason, "Approach of a solid sphere to a rigid plane interface", *J. Coll. Sci.*, **16** 6, 632-635 (1961).
- [69] M. D. Carbajal-Tinoco, R. Lopez-Fernandez and J. L. Arauz-Lara, "Asymmetry in Colloidal Diffusion near a Rigid Wall", *Phys. Rev. Lett.*, **99**, 138303 (2007).
- [70] K. Ishii, T. Iwai and H. Xia, "Hydrodynamic measurement of Brownian particles at a liquid-solid interface by low-coherence dynamic light scattering", *Opt. Express*, **18** 7, 7390-7396 (2010).
- [71] L. Liu, A. Woolf, A. W. Rodriguez and F. Capasso, "Absolute position total internal reflection microscopy with an optical tweezer", *PNAS*, **111** 52, E5609-E5615 (2014).
- [72] C. Ha, H. D. Ou-Yang and H. K. Pak, "Direct measurements of colloidal hydrodynamics near flat boundaries using oscillating optical tweezers", *Physica A*, **392** 17, 3497-3504 (2013).
- [73] G. M. Wang, E. M. Sevick, E. Mittag, D. J. Searles and D. J. Evans, "Experimental demonstration of violations of the second law of thermodynamics for small systems and short time scales", *Phys. Rev. Lett.*, **89**, 050601 (2002).
- [74] R. Brown, "XXVII. A brief account of microscopical observations made in the months of June, July and August 1827, on the particles contained in the pollen of plants; and on the general existence of active molecules in organic and inorganic bodies", *The Philosophical Magazine*, **4** 21, 161-173 (1828).
- [75] E. Frey and K. Kroy, "Brownian motion: a paradigm of soft matter and biological physics", *Ann. Phys.*, **14** 1-3, 20-50 (2005).
- [76] T. Li, S. Kheifets, D. Medellin and M. G. Raizen, "Measurement of the instantaneous velocity of a Brownian particle", *Science*, **328** 5986, 1673-1675 (2010).
- [77] R. Cox and S. Hsu, "The lateral migration of solid particles in a laminar flow near a plane", *Int. J. Multiphase Flow*, **3**, 201-222 (1977).
- [78] J. Zhang *et al.*, "Fundamentals and applications of inertial microfluidics: a review", *Lab Chip*, **16**, 10-34 (2016).
- [79] M. Yang and M. Ripoll, "Brownian motion in inhomogeneous suspensions", *Phys. Rev. E*, **87**, 062110 1-7 (2013).

- [80] M. von Smoluchowski, "Contribution à la théorie de l'endosmose électrique et de quelques phénomènes corrélatifs", *Bull. Akad. Sci. Cracovie.*, **8**, 182-200 (1903).
- [81] R. J. Hunter, "Zeta Potential in Colloid Science. Principle and Applications", Academic Press, London (1988).
- [82] P. Warszyński, "Coupling of hydrodynamic and electric interactions in adsorption of colloidal particles", *Adv. Coll. Int. Sci.*, **84** 1-3, 47-142 (2000).
- [83] H. Oshima, T. W. Healy and L. R. White, "Sedimentation velocity and potential in a dilute suspension of charged spherical colloidal particles", *J. Chem. Soc., Faraday Trans. 2*, **80**, 1299-1317 (1984). 1299
- [84] S. M. Tabatabaei and T. G. M. van de Ven, "Tangential electroviscous drag on a sphere surrounded by a thin double layer near a wall for arbitrary particle-wall separations", *J. Fluid. Mech.*, **656**, 360-406 (2010).
- [85] S. M. Tabatabaei, T. G. M. van de Ven and A. D. Rey, "Electroviscous sphere-wall interactions", *J. Coll. Int. Sci.*, **301**, 291-301 (2006).
- [86] D. C. Prieve and S. G. Bie, "Electrokinetic repulsion between two charged bodies undergoing sliding motion", *Chem. Eng. Comm.*, **55**, 149-164 (1987).
- [87] X. Wu, P. Warszyński and T.G.M. van de Ven, "Electrokinetic Lift: Observations and Comparisons with Theories", *J. Colloid Interface Sci.*, **180**, 61-69 (1996).
- [88] R. G. Cox, "Electroviscous forces on a charged particle suspended in a flowing liquid", *J. Fluid Mech.*, **338**, 1-34 (1997).
- [89] P. Warszyński, X. Wu, T. G. M. van de Ven, "Electrokinetic lift force for a charged particle moving near a charged wall — a modified theory and experiment", *Colloids Surf. A*, **140**, 183-198 (1998).
- [90] L. Léger and J. F. Joanny, "Liquid spreading", *Rep. Prog. Phys.*, **55**, 431-486 (1992).
- [91] G. Boniello, "Brownian motion of partially wetted colloidal particles", PhD thesis (2014).
- [92] T. Young, "An essay on the cohesion of fluids", *Philos. Trans. R. Soc. London*, **95**, 65-87 (1805).
- [93] D. M. Kaz, R. McGorty, M. Mani, M. P. Brenner and V. N. Manoharan, "Physical ageing of the contact line on colloidal particles at liquid interfaces. Supplementary Information", *Nature Materials* **11**, (2012).
- [94] A. Wang, W. B. Rogers and V. N. Manoharan, "Effects of Contact-Line Pinning on the Adsorption of Nonspherical Colloids at Liquid Interfaces", *Phys. Rev. Lett.*, **119**, 108004 (2017). DOI:<https://doi.org/10.1103/PhysRevLett.119.108004>
- [95] M. I. Mishchenko and L. D. Travis, "Capabilities and limitations of a current FORTRAN implementation of the T-matrix method for randomly oriented, rotationally symmetric scatterers", *J. Quant. Spectrosc. Radiat. Transfer*, **60**, 309-324 (1998). DOI:10.1016/S0022-4073(98)00008-9.
- [96] L. Helden *et al.*, "Single-particle evanescent light scattering simulations for total internal reflection microscopy", *Appl. Opt.*, **45** (28), 7299-7308 (2006).

- [97] C. Hertlein *et al.*, "Experimental verification of an exact evanescent light scattering model for TIRM", *Langmuir*, **24** (1), 1-4 (2008).
- [98] A. E. Cervantes-Martínez, A. Ramírez-Saito, R. Armenta-Calderón, M. A. Ojeda-López and J. L. Arauz-Lara, "Colloidal diffusion inside a spherical cell", *Phys. Rev. E*, **83**, 030402 (2011).
- [99] B. L. Arenas-Gómez and M. D. Carbajal-Tinoco, "Brownian motion of a colloidal particle immersed in a polymeric solution near a rigid wall", *Rev. Mex. Fis.*, **60**, 243-248 (2014).
- [100] J. C. Crocker and D. G. Grier, "Methods of Digital Video Microscopy for Colloidal Studies", *J. Coll. Int. Sci.*, **179** (1), 298-310 (1996). DOI: 10.1006/jcis.1996.0217
- [101] S. Coertjens, R. De Dier, P. Moldenaers, L. Isa and J. Vermant, "Adsorption of ellipsoidal particles at liquid-liquid interfaces", *Langmuir*, **33**(11), 2689-2697 (2017). <http://dx.doi.org/10.1021/acs.langmuir.6b03534>
- [102] D. Mukhija and M. J. Solomon, "Translational and rotational dynamics of colloidal rods by direct visualization with confocal microscopy", *J. Coll. Int. Sci.*, **314** (1), 98-106 (2007). <https://doi.org/10.1016/j.jcis.2007.05.055>
- [103] G. Rabut and J. Ellenberg, "Automatic real-time three-dimensional cell tracking by fluorescence microscopy", *J. Microsc.*, **216**, 131-137 (2004). <https://doi.org/10.1111/j.0022-2720.2004.01404.x>
- [104] L. Limozin and K. Sengupta, "Quantitative Reflection Interference Contrast Microscopy (RICM) in Soft Matter and Cell Adhesion", *Chem. Phys. Chem.*, **10**, 2752-2768 (2009).
- [105] C. Akcay, P. Parrein and J. P. Rolland, "Estimation of longitudinal resolution in optical coherence imaging", *Appl. Opt.*, **41** (25), 5256-5262 (2002).
- [106] G. Wiegand, K. R. Neumaier and E. Sackmann, "Microinterferometry: three-dimensional reconstruction of surface microtopography for thin-film and wetting studies by reflection interference contrast microscopy (RICM)", *App. Opt.*, **37**, 6892-6905 (1998).
- [107] C.C. Ho, A. Keller, J.A. Odell, and R.H. Ottewill, "Preparation of monodisperse ellipsoidal polystyrene particles", *Colloid Polym. Sci.*, **271**(5), 469-479 (1993).
- [108] Engineering ToolBox, (2003). Water-Density, Specific Weight and Thermal Expansion Coefficient. [online] Available at: [https://www.engineeringtoolbox.com/water-density-specific-weight-d\\_95.html](https://www.engineeringtoolbox.com/water-density-specific-weight-d_95.html) [Accessed Dec. 2017].
- [109] Engineering ToolBox, (2017). Density of aqueous solutions of inorganic sodium salts. [online] Available at: [https://www.engineeringtoolbox.com/density-aqueous-solution-inorganic-sodium-salt-concentration-d\\_1957.html](https://www.engineeringtoolbox.com/density-aqueous-solution-inorganic-sodium-salt-concentration-d_1957.html) [Accessed Dec. 2017].
- [110] J. Eastoe and J. S. Dalton, "Dynamic surface tension and adsorption mechanisms of surfactants at the air-water interface", *Adv. Coll. Int. Sci.*, **85**. 103-144 (2000).

- [111] N. Matubayasi, H. Matsuo, K. Yamamoto, S. Yamaguchi and A. Matuzawa, "Thermodynamic Quantities of Surface Formation of Aqueous Electrolyte Solutions - I. Aqueous Solutions of NaCl, MgCl<sub>2</sub>, and LaCl<sub>3</sub>", *J. Coll. Int. Sci.*, **209**, 398-402 (1999).
- [112] Brian Higgins and Housam Binous, "Configuration of a Sessile Drop", <http://demonstrations.wolfram.com/ConfigurationOfASessileDrop/> - Wolfram Demonstrations Project, Published: April 13, 2012.
- [113] E. C. Mbamala and H. H. von Grünberg, "Effective interaction of a charged colloidal particle with an air-water interface", *J. Phys.: Condens. Matter*, **14** (19), 4881 (2002). <http://doi.org/10.1088/0953-8984/14/19/313>
- [114] H. Wendt et al., "Ullmann's Encyclopedia of Industrial Chemistry. Electrochemistry", 7<sup>th</sup> edition, Wiley-VCH (2004).
- [115] B. M. Alexander and D. C. Prieve, "A Hydrodynamic Technique for Measurement of Colloidal Forces", *Langmuir*, **3**, 788-795 (1987).
- [116] D. Zwillinger and S. Kokoska, "Standard Probability and Statistics Tables and Formulae", 1<sup>st</sup> edition, Chapman & Hall/CRC (2000).
- [117] M. Paterno, "Calculating Efficiencies and Their Uncertainties", (FERMILAB-TM-2286-CD; Batavia: Fermilab), (2004). <http://home.fnal.gov/~paterno/images/effic.pdf>
- [118] A. Ibrahim, H. Ohshima, S. A. Allison and H. Cottet, "Determination of effective charge of small ions, polyelectrolytes and nanoparticles by capillary electrophoresis", *J. Chromatogr. A*, textbf1247, 154-164 (2012).
- [119] G. E. Yakubov, O. I. Vinogradova and H. Butt, "Contact angles on hydrophobic microparticles at water-air and water-hexadecane interfaces", *J. Adhes. Sci. Technol.*, **14**, 1783-1799 (2000).
- [120] G. Boniello *et al.*, "Brownian diffusion of a partially wetted colloid", *Nature Materials*, **14** 9, 908-911 (2015).
- [121] D. C. Prieve and W. B. Russel, "Simplified Predictions of Hamaker Constant from Lifshitz Theory", *J. Coll. Int. Sci.*, **125**, 1-13 (1988).
- [122] J. Marra, "Direct measurements of attractive van der Waals and adhesion forces between uncharged lipid bilayers in aqueous solutions", *J. Coll. Int. Sci.*, **109** (1), 11-20 (1986).
- [123] P. Warszyński and Z. Adamczyk, "Calculations of Double-Layer Electrostatic Interactions for the Sphere/Plane Geometry", *J. Coll. Int. Sci.*, **187**, 283-295 (1997).
- [124] V. Perel and B. Shklovskii, "Screening of a macroion by multivalent ions: a new boundary condition for the Poisson-Boltzmann equation and charge inversion", *Phys. A*, **274** 3-4, 446-453 (1999).
- [125] R. Messina, C. Holm and K. Kremer, "Strong Attraction between Charged Spheres due to Metastable Ionized States", *Phys. Rev. Lett.* **85** 4, 872-875 (2000).
- [126] S. A. Safran "Statistical Thermodynamics of Surfaces, Interfaces, and Membranes" (Chap.3, pag.80), 1<sup>st</sup> edition, CRC Press (2018).

- [127] R. Messina, C. Holm and K. Kremer, "Effect of colloidal charge discretization in the primitive model", *Eur. Phys. J. E*, **4**, 363-370 (2001).
- [128] D. Li and X. Zhao, "Micro and nano bubbles on polystyrene film/water interface", *Colloid Surface A*, **459**, 128-135 (2014).
- [129] J. N. Israelachvili and R. M. Pashley, "The hydrophobic interaction is long-range, decaying exponentially with distance", *Nature*, **300**, 341-342 (1982).
- [130] J. N. Israelachvili and R. M. Pashley, "Measurement of the hydrophobic interaction between two hydrophobic surfaces in aqueous electrolyte solutions", *J. Colloid. Interface Sci.*, **98** 2, 500-514 (1984).
- [131] T. D. Blake and J. A. Kitchener, "Stability of aqueous films on hydrophobic methylated silica", *J. Chem. Soc., Faraday Trans. 1*, **68**, 1435-1442 (1972).
- [132] E. E. Meyer, K. J. Rosenberg and J. N. Israelachvili, "Recent progress in understanding hydrophobic interactions", *PNAS*, **103** 43, 15739-15746 (2006).
- [133] M. U. Hammer, T. H. Anderson, A. Chaimovich, M. S. Shell and J. N. Israelachvili, "The search for the hydrophobic force law", *Faraday Discuss*, **146**, 299-308 (2010).
- [134] M. Mezger *et al.*, "High resolution in situ x-ray study of the hydrophobic gap at the water-octadecyl-trichlorosilane interface", *PNAS*, **103**, 18401-18404 (2006).
- [135] R. F. Tabor, F. Grieser, R. R. Dagastine and D. Y. C. Chan, "The hydrophobic force: measurements and methods", *Phys. Chem. Chem. Phys.*, **16**, 18065-18075 (2014).
- [136] E. E. Meyer, Q. Lin, T. Hassenkam, E. Oroudjev and J. N. Israelachvili JN, "Origin of the long-range attraction between surfactant-coated surfaces", *PNAS*, **102**, 6839-6842 (2005).
- [137] P. Attard, "Thermodynamic analysis of bridging bubbles and a quantitative comparison with the measured hydrophobic attraction", *Langmuir*, **16**, 4455-4466 (2000).
- [138] G. E. Yakubov, H. J. Butt and O. I. Vinogradova, "Interaction forces between hydrophobic surfaces. Attractive jump as an indication of formation of 'stable' submicrocavities", *J. Phys. Chem. B*, **104**, 3407-3410 (2000).
- [139] M. Azadi, A. V. Nguyen and G. E. Yakubov, "Attractive forces between hydrophobic solid surfaces measured by AFM on the first approach in salt solutions and in the presence of dissolved gases", *Langmuir*, **31**, 1941-1949 (2015).
- [140] Detlef Lohse Xuehua Zhang "Surface nanobubbles and nanodroplets", *Rev. Mod. Phys.*, **87**, 981-1035 (2015).
- [141] W. T. Coffey, Y. P. Kalmykov and J. T. Waldron, "The Langevin equation. With applications to stochastic problems in physics, chemistry and electrical engineering", 2<sup>nd</sup> Edition, World Scientific (2004).
- [142] M. C. Wang and G. E. Uhlenbeck, "On the Theory of the Brownian Motion II", *Rev. Mod. Phys.*, **17**, 323-342 (1945).
- [143] G. Volpe and G. Volpe, "Simulation of a Brownian particle in an optical trap", *Am. J. Phys.*, **81** 3, 224-230 (2013).

- [144] , "Stochastic Differential Equations. An Introduction with Applications", 5<sup>th</sup> edition, Springer-Verlag Heidelberg, New York.
- [145] Y. Han, A. M. Alsayed, M. Nobili, J. Zhang, T. C. Lubensky and A. G. Yodh, "Brownian Motion of an Ellipsoid", *Science*, **314** (5799), 626-630 (2006).
- [146] R. Di Leonardo, S. Keen, F. Ianni, J. Leach, M. J. Padgett and G. Ruocco, "Hydrodynamic interactions in two dimensions", *Phys. Rev. E*, **78**, 031406 (2008).
- [147] C. I. Bouzigues, P. Tabeling and L. Bocquet, "Nanofluidics in the Debye Layer at Hydrophilic and Hydrophobic Surfaces", *Phys. Rev. Lett.*, **101**, 114503 (2008).
- [148] D. M. Huang, C. Cottin-Bizonne, C. Ybert and Lydéric Bocquet, "Ion-Specific Anomalous Electrokinetic Effects in Hydrophobic Nanochannels", *Phys. Rev. Lett.*, **98**, 177801 (2007).
- [149] L. Joly, F. Detcheverry and A. Biance, "Anomalous  $\zeta$  Potential in Foam Films", *Phys. Rev. Lett.*, **113**, 088301 (2014).
- [150] B. Blanc, O. Bonhomme, P. Brevet, E. Benichou, C. Ybert and A. Biance, "Electroosmosis near surfactant laden liquid-air interfaces", *Soft Matter*, **14**, 2604-2609 (2018).
- [151] A. Delgado, F. Gonzalez-Caballero and J. M. Bruque, "On the Zeta Potential and Surface Charge Density of Montmorillonite in Aqueous Electrolyte Solutions", *J. Coll. Int. Sci.*, **113** 1, 203-211 (1986).
- [152] L. M. Vane and G. M. Zang, "Effect of aqueous phase properties on clay particle zeta potential and electro-osmotic permeability: Implications for electrokinetic soil remediation processes", *J. Haz. Mat.*, **55** 1-3, 1-22 (1997).
- [153] W. W. Wilson, M. M. Wade, S. C. Holman and F. R. Champlin, "Status of methods for assessing bacterial cell surface charge properties based on zeta potential measurements", *J. Microbiol. Methods*, **43** 3, 153-164 (2001).
- [154] A. Wiacek and E. Chibowski, "Zeta potential, effective diameter and multimodal size distribution in oil/water emulsion", *Coll. Surf. A*, **159** 2-3, 253-261 (1999).
- [155] A. Mertelj, J. L. Arauz-Lara, G. Maret, T. Gisler, and H. Stark, "Rotational diffusion in a bistable potential", *Europhys. Lett.*, **59**, 337-343 (2002).

# Acknowledgements

On the occasion of the submission of the final version of my PhD thesis, I would like to thank the people that more have been determinant for the development of the work and for my personal growth during these three years. It is not possible, and maybe this is not the best place, to detailed report all the richness I received from them here in Montpellier, but a preliminary summary must here be made.

First, I would like to thank prof. Maurizio Nobili for the opportunity given to me to participate in this interesting project and to enrich my experience and education with a PhD here in Montpellier, also through the possibility to participate to international conferences and the observation of his working method. Then there is Antonio Stocco, determinant for the help, the motivation and the support from both the working and the human sides. Furthermore, I am very grateful for the opportunity to learn from the experience of Christophe Blanc; I also thank him for his constant availability and patience in helping me.

I have then to say thank you to the referees and to all the members of the thesis jury, as well as to the members of all the *comité de thèse* for the availability and for the interesting and constructive discussions.

A very special thank you to all the members of the Soft Matter and Glasses group at the Charles Coulomb laboratory. They are too many, and they gave me too much, to list them here, but their company, as well as the one of the friends here in Montpellier, has been determinant for my thesis. Life is one and united: a work cannot be well done if the human side is forgotten.

Finally, special thanks go of course to my family and to Maria, for the sacrifice of the distance and the constant support without expecting any return.

Stefano Villa

Montpellier, 22th February 2019

